Pore Scale Modeling of Capillary Pressure Curves in 2D Rock Images

by

Yingfang Zhou

Thesis submitted in partial fulfillment of
the requirements for the degree of
Philosophiae Doctor (PhD)

Faculty of Science and Technology
Department of Petroleum Engineering
2013

Acknowledgements

I would like to express my sincere gratitude to my supervisor, Prof. Dr. Dimitrios G. Hatzignatiou, for his excellent guidance and supervision during the entire period of this research. His discussions and encouragement have been inspiring.

My sincere gratitude also goes to my co-supervisor, Dr. Johan Olav Helland for his supervision and the many fruitful discussions we have had along the way.

I would like to take this opportunity to express my great appreciation to Prof. Dr. Svein M. Skjæveland for advising me of the Ph.D courses I was taking and the fruitful discussions we have had.

Also, I would like to thank all my colleagues at IRIS; special thanks go to Dr. Sigmund Stokka for introducing me to this Ph.D position in IRIS; Dr. Kirsti Veggeland and Siv Marie Åsen for arranging all the EOR group meetings; Dr. Espen Jettestuen for performing the Lattice Boltzmann simulation in Paper 4 of this thesis; Mr. Erich Suter for helping me with C# code; Drs. Aruoture Voke Omekeh and Alexey Khrulenko and Mr. Ali Mehrabi for the pleasant coffee breaks and interesting discussions we have had; and others too numerous to mention, for the pleasant times we have spent during the research period.

I would like to express my gratitude to my family and friends in China and Norway for their encouragement and support. I want to especially thank my parents, Shengcheng Zhou and Xianglian Yi for their encouragement in all my pursuits. And most of all, my loving wife, Qing Luo, for her

love and understanding.

I am especially grateful to the Research Council of Norway, ConocoPhillips and the Ekofisk co-venturers, including TOTAL, ENI, Statoil and Petoro for supporting this study.

Abstract

Capillary pressure is relevant to most processes of multiphase flow in porous media, as it controls the pore scale fluids distribution. Reliable capillary pressure curves are required to model and predict larger-scale multiphase flow processes; normally these capillary pressures are obtained experimentally using representative core samples. Besides core scale measurements, pore scale modeling provides another alternative, physically-sound approach to compute capillary pressure curves and links the pore scale properties to laboratory measurements.

Pore scale modeling is a useful tool to enhance our understanding of capillary phenomena and their impact on microscopic fluid flow in porous media. In this thesis, an existing semi-analytical pore scale model is further developed to compute two- and three-phase fluid configurations and capillary pressure curves at arbitrary wetting conditions in 2D realistic pore spaces that are extracted directly from segmented rock images. The simulated capillary pressure curves and fluid configurations are used as input in an improved interacting tube bundle model to simulate viscosity-

and capillary-dominated flow in porous media. The dynamic effects of capillary pressure are further investigated by comparing the equilibrium static capillary pressure and the simulated dynamic capillary pressure curves.

Based on this research work, seven research papers have been presented in scientific journals and international conferences. The main findings are summarized below:

Two-phase capillary pressure curves computed at uniformly-wet conditions can be scaled by the traditional J-function. The imbibition capillary pressure curves and fluid configurations at mixed-wet conditions depend strongly on the initial water saturation and formation wettability. Based on simulated results, a novel dimensionless capillary pressure function for mixed-wet conditions has been developed to describe more accurately the variability of formation wettability and permeability in reservoir simulation models.

In water-wet three-phase systems, capillary entry pressure for the non-wetting phase (e.g., gas or CO_2) is strongly affected by the existing initial fluid configuration of oil and water in the pore space. Generally, the three-phase capillary entry pressure is lower for gas (or CO_2) displacing oil than for gas (or CO_2) displacing water in a uniform water-wet system, indicating that CO_2 is stored more safely below low-permeable formation layers in subsurface aquifers than in depleted oil reservoirs. The simulated three-phase fluid configurations exhibit a similar behavior as that

observed in micro-CT experiments; in spreading systems very thin oil-layers are present, while in non-spreading systems only a few relatively thick oil layers exist when gas-oil capillary pressure is low. In the major parts of the three-phase region (except for small oil saturations).

The gas-oil capillary pressure at water-wet conditions seems to be described well as a function of only the gas saturation in the major part of the three-phase region, despite three-phase displacements in which gas displaces both oil and water occur frequently in individual pore geometries for the non-spreading systems. At small oil saturations, the gas-oil capillary pressure depends strongly on two saturations, which is particularly visible in the results for the weakly water-wet spreading system because thin oil layers exist after gas has started to invade pores occupied by water only.

The simulated saturation profiles under viscous-capillary dominated flow can be explained by the capillary pressure and fluid configurations, which exhibit increasingly gradual behavior as the contact angle defined on the oil-wet solid surfaces increases or the initial water saturation decreases.

Drainage dynamic capillary pressure curves are located at a higher capillary level than the corresponding static curve, whereas for imbibition the dynamic curve is located at a lower capillary level than the corresponding static one, regardless the porous medium wettability. The simulated dynamic capillary coefficient is a function of saturation and independent of the incremental pressure step, which is consistent with the results re-

ported in previous studies. The dynamic coefficient increases with decreasing water saturation at water-wet conditions, whereas for mixed- to oil-wet conditions it increases with increasing water saturation. Imbibition simulations also show that the dynamic capillary coefficient at a constant saturation increases with decreasing initial water saturation at mixed-wet conditions.

List of papers

1. Zhou, Y., Helland, J. O., and Hatzignatiou, D. G. 2011: A model for imbibition in pore spaces from 2D rock images. Extended abstract presented at the Pore2Field International Conference held at IFP Energies nouvelles, Rueill-Malmaison, France, November 16-18, 2011.

2. Zhou, Y., Helland, J.O., and Hatzignatiou, D.G. 2013. A Dimensionless Capillary Pressure Function for Imbibition Derived From Pore-Scale Modeling in Mixed-Wet-Rock Images. *SPE Journal*. 18 (2): 296-308. SPE-154129-PA. http://dx.doi.org/10.2118/154129-PA.

3. Zhou, Y., Helland, J.O. and Hatzignatiou, D.G.: Pore-Scale Modelling of Water Flooding in Mixed-Wet Rock Images: Effects of Initial Saturation and Wettability, *SPE Journal*. SPE-154284-PA (in press; posted 05 July 2013). http://dx.doi.org/10.2118/154284-PA.

4. Zhou, Y., Helland, J.O., and Jettestuen, E. 2013. Dynamic Capillary Pressure Curves From Pore-Scale Modeling in Mixed-Wet-Rock Images. *SPE Journal*. 18 (4): 634-645. SPE-154474-PA. http://dx.doi.org/10.2118/154474-PA.

5. Zhou, Y., Helland, J. O. and Hatzignatiou, D.G. 2013: Computation of three-phase capillary entry pressures and arc menisci configurations in pore geometries from 2D rock images: a combinatorial approach, 2013. Submitted to *Advances in Water Resources*.

6. Zhou, Y., Helland, J. O., and Hatzignatiou, D. G. 2013: Simulation of three phase capillary pressure curves directly in 2D rock images, paper IPTC 16547 presented at the International Petroleum Technology Conference, Beijing, China, 26-28 March 2013.

7. Zhou, Y., Helland, J. O., and Hatzignatiou, D. G. 2013: Simulation of three phase capillary pressure curves directly in 2D uniformly-wet rock images, Manuscript under preparation.

Table of Contents

List of Figures

List of Tables

List of Symbols

Roman Symbols

C	Coefficient, N/m
CA	Capillary number, Dimensionless
F	Entry curvature, m^{-1}
g	Conductance, m^4
H	Pinning point, Dimensionless
J	J-function, Dimensionless
K	Permeability, m^2
L	Length of cross-sectional pore-boundary segments, interface or capillary tube, m
P	Pressure, Pa
q	Flow rate, m^3/s
r	Circle radius, m
T	Segment, Dimensionless
t	Time, s
V	Volume, m^3

v	Curve, Dimensionless

Greek Symbols

α	Orientation angle, $^\circ$
Γ	Pore boundary, Dimensionless
μ	Viscosity, Pa.s
ϕ	Porosity, Dimensionless
σ	Interfacial tension, N/m
τ	Dynamic coefficient, Pa.s
θ	Contact angle, $^\circ$
b	Pore boundary point, Dimensionless

Superscripts

c	Clockwise
cc	Counter clockwise
dyn	Dynamic
E	Form (with respect to AM lengths)
F	Vanish (with respect to AM lengths)
$stat$	Static

Subscripts

a	After
b	Before
c	Capillary or Cassie
g	Gas
o	Oil or Oil-wet
p	Pore space

pd	Primary drainage
S	Spreading
w	Water or Water-wet

Abbreviations

AM	Arc meniscus
BR	Bulk region
CFD	Computational fluid dynamics
CR	Corner region
CT	Computerized tomography
EOR	Enhanced Oil Recovery
LR	Layer region
MIS	Maximal inscribed sphere
MR	Mixed region
MS-P	Mayer and Stowe-Princen
MTM	Main terminal meniscus
SEM	Scanning-Electron-Microscope
WAG	Water-Alternating-Gas

Chapter 1

Introduction

Multiphase flow in porous media is encounted in several Enhanced Oil Recovery (EOR) methods in petroleum reservoirs, such as gas drainage, depressurization below bubble point pressure resulting in the flow of liberated gas phase, Water-Alternating-Gas (WAG) and CO_2 injection, as well as in environmentally focused processes, such as groundwater contamination and CO_2 sequestration. The performance of such processes requires a thorough understanding of two- and three-phase displacements in reservoir rock. For example, in the context of CO_2 storage, capillary pressure is directly related to two of the main trapping mechanisms – *structural* and *residual* trapping (Saadatpoor et al., 2010; MacMinn & Juanes, 2009; Juanes et al., 2010). Similarly, oil recovery can be increased in hydrocarbon reservoirs by injecting a third fluid after water flooding, e.g., CO_2, to displace remaining oil from pore space. The application of the governing equations for modeling experimentally-observed behavior in porous media by reservoir simulation also requires *a priori* knowledge of capillary pressure and phase saturation relationships. These relationships can be measured in the laboratory from core samples; however, because laboratory measurements are time-consuming and technically complicated, especially for three-phase capillary pressure curves, the common practice today is to determine these relationships using correlations that have

been formulated based on much more readily available two-phase data (Baker, 1998; Lenhard & Parker, 1988). Besides challenging laboratory measurements, pore scale modeling provides an alternative physically-based approach to predict capillary pressure curves (Kovscek et al., 1993; Øren et al., 1998; Blunt, 2001; Øren & Bakke, 2002).

1.1 Capillary pressure and wettability

Capillary pressure is defined as the pressure difference across an interface between two fluids. In a porous medium saturated with gas, oil and water this definition can be expressed as

$$P_{cij} = P_i - P_j, ij = ow, go, gw. \tag{1.1}$$

Combination of these equations gives the relationship between the three phase capillary pressures,

$$P_{cgw} = P_{cgo} + P_{cow}. \tag{1.2}$$

The phase saturations are defined as

$$S_i = \frac{V_i}{V_p}, i = g, o, w; \tag{1.3}$$

where V_p is the pore volume and V_i denotes the volume of phase i. Throughout this thesis, drainage is referred to the process where a lighter fluid displaces a denser fluid, e.g., oil displaces water. Likewise, imbibition is referred to the process where a denser fluid displaces a lighter fluid, e.g., water displaces oil. It is well-known that the relationships between capillary pressures and saturations (capillary pressure curves) depend on the formation wettability (Anderson, 1987; Tiab & Donaldson, 2004). Wettability, defined as the tendency of one fluid to spread on or adhere to a solid surface in the presence of other immiscible fluids, affects the distribution and transport behavior of fluids during displacement (Tiab &

Donaldson, 2004). For hydrocarbon reservoirs, the degree of wettability can be quantified by the contact angle between phases i and j, θ_{ij}, which is measured through the denser phase j.

The wettability of a reservoir rock could be either homogeneous or heterogeneous. If the entire rock surface has the same affinity for wetting/non-wetting phase, the wettability is classified as homogeneous or uniform wettability. Generally, for an oil/water homogeneous system, when θ_{ow} is between 0° and 60° - 75°, the system is defined as water wet. When θ_{ow} is between 180°and 120° - 105°, the system is defined as oil wet. In the middle range of θ_{ow}, the system is considered to be neutrally or intermediately wet (Anderson, 1986).

Alternatively, the internal surface of reservoir rock is composed of many minerals with different surface chemistry and absorption properties, which may lead to heterogeneous or nonuniform wettability. The term mixed wettability was introduced by Salathiel (1973) for a special case in which the oil-wet surface forms continuous paths through the larger pores.

The mixed-wet reservoirs are considered to be developed from the following process (Salathiel, 1973; Kovscek et al., 1993; Kaminsky & Radke, 1997). The reservoir is initially assumed to be completely water saturated and water wet. When oil invades the pore space, a water film is left between the surface and the invading hydrocarbon phase. Capillary forces retain water in small capillaries and grain contacts. However, when a critical capillary pressure is exceeded the water film destabilizes and ruptures to an adsorbed molecular film of up to several water monolayers. Surface active components (e.g., asphaltenes) from the oil phase are deposited on the rock surface, thus making it oil wet, and consequently mixed wet conditions are developed.

Traditional core scale measurements are normally used to obtain the capillary pressure curves. However these measurements are time consuming, might damage the samples and also cannot quantify spatial variation of the pore scale properties, such as wettability and pore geometry. Pore scale modeling provides another alternative physically-sound approach

which can be used to calculate capillary pressure curves by simulating the fluid distributions in the pore space under precisely described pore scale conditions; this offers the opportunity to obtain a more thorough understanding of the impact of underlying pore-scale physics on macro-scale flow properties.

1.2 Pore scale modeling

Pore scale modeling is attracting an increasing attention in the oil and gas industry during the last decades, and has potential applications in contaminant transport and carbon dioxide storage (Blunt, 2001; Frette & Helland, 2010; Bandara et al., 2011; Joekar-Niasar et al., 2012; Mostaghimi et al., 2012; Raeini et al., 2012; Raoof et al., 2012; Blunt et al., 2013). In addition to predicting fundamental flow parameters (e.g., capillary pressure and relative permeability) (Kovscek et al., 1993; Øren et al., 1998; van Dijke & Sorbie, 2002a; Piri & Blunt, 2005; Silin & Patzek, 2006; Helland & Skjæveland, 2006a; Mousavi et al., 2013), pore scale modeling is also capable of investigating the effects of micro-scale phenomena on the macro-scale behaviors, and thus it provides a physically-based approach to upscale multiphase flow in porous media from micro-scale to macro-scale (Middleton et al., 2012; Mehmani et al., 2012; Al-Dhahli et al., 2013; Porta et al., 2013).

Pore scale modeling methods require a proper representation of pore space and depend on pore-level physics of displacement mechanisms. There are two methods to model fluids flow in 3D pore space. The first is the direct application of computational fluid dynamics (CFD) to imaged pore space, such as the Lattice Boltzmann methods (Ahrenholz et al., 2006; Boek & Venturoli, 2010; Ramstad et al., 2010), level set methods (Prodanović & Bryant, 2006; Jettestuen et al., 2013), volume of fluid method (Raeini et al., 2012), smoothed particle hydrodynamics methods (Tartakovsky & Meakin, 2006) and the completely different method, morphology-based methods (Ahrenholz et al., 2008; Silin et al., 2011). The problem is that

for the key applications of interest, these techniques require numerical discretization within the irregular pore geometry, as well as mesh refinement around small pores, and consequently most of them are computationally demanding. An alternative methodology is the use of pore-network models (Øren et al., 1998; Blunt, 2001; Valvatne et al., 2005; Piri & Blunt, 2005; Joekar-Niasar & Hassanizadeh, 2012; Al-Dhahli et al., 2013), which first extract a topologically representative network with idealized geometries (e.g., circle, square, star, triangle) derived from the underlying image and then solve the flow and transport problem in the reconstructed simplified version of the pore space.

In addition to the advanced CFD and pore-network methods, straight capillary bundle models provide a simple, yet physically-sound approach to estimate capillary entry pressure, fluid configurations and capillary pressure curves. Two types of methods are adopted for representing the cross-sections of the straight tube model. The first representation method is cross-sections with analytical angular geometries and a pore size distribution function (Kovscek et al., 1993; Ma et al., 1996; van Dijke et al., 2004; Helland & Skjæveland, 2006b); the other method is extracted cross-section geometries directly from rock images (Lindquist, 2006; Virnovsky et al., 2009; Frette & Helland, 2010; Helland & Frette, 2010; Glantz & Hilpert, 2011; Kim & Lindquist, 2012). The straight tube model with angular tube cross-sections allow the development of mixed wettability and cross-sectional multiphase configurations and thus are well suited as a basis for developing simple, yet physically-based models accounting for some of the important capillary phenomena that occur in porous media; hence such models represent a natural starting point for developing and analyzing capillary pressure curves.

1.3 Motivation and scientific contributions

The primary motivation of this work is to extend an existing semi-analytical model, which has been utilized previously to compute two-fluid config-

urations, the associated capillary entry pressures and capillary pressure curves in individual straight tubes with cross-sections given by pore spaces extracted from rock images (Frette & Helland, 2010; Helland & Frette, 2010), into a model which will enable us to compute two- and three-phase capillary pressure curves and fluid configurations in large segmented Scanning-Electron-Microscope (SEM) images of Bentheim sandstone that contain many separate, and irregular-shaped pore spaces. In addition, the interacting tube bundle model (Dong et al., 2005; Wang & Dong, 2011) has been further developed to simulate the saturation profile evolution and subsequently analyze the dynamic effects of capillary pressure in mixed-wet porous media.

The proposed models provide insights into the pore-scale mechanisms of multiphase flow in porous media, which allows for improved understanding and thus enhanced interpretation of core-scale experiments, and guidance in developing reliable three-phase capillary pressure correlations.

1.4 Structure of thesis

Following this brief introduction, the remaining of the thesis is organized as follows: Chapter 2 presents the background theory and literature review. Chapter 3 contains a description of the developed models. The method used to compute two-phase capillary pressure curves and fluid configurations both at uniformly- and mixed-wet conditions directly in 2D segmented SEM images is described first. Then, the developed extension of this method for computing three-phase capillary pressure curves and fluid configurations at uniformly-wet rock images is presented. The interacting tube bundle model for simulating the saturation profile evolution and the algorithm to account for dynamic capillary pressure curves are also described. Finally, a short description of the models utilization and capabilities is included. Chapter 4 contains a brief summary of simulation results obtained during the course of this work along with relevant discussions. Chapter 5 includes the conclusions reached from these results

and closes with recommendations for future work.

Chapter 2

Literature Review

In this chapter several aspects related to pore scale modeling for computing capillary pressure curves, fluid configurations, dynamic effects and related areas are reviewed. These aspects include 3D reconstruction of pore spaces, pore scale based computation methods, wettability, pore scale displacement mechanisms, entry capillary pressure, static and dynamic capillary pressure. Based on the literature review, the methods employed in this work are presented and the new features implemented in the existing pore scale model are highlighted.

2.1 Pore space reconstruction

Realistic characterization of a porous medium structure is a prerequisite for pore scale modeling. Based on imaging techniques (e.g., micro-x-ray computerized tomography (micro-CT), SEM), there are three ways in which a three-dimensional (3D) representation of a pore space can be obtained. The first is through direct imaging, usually by x-ray micro-CT and the application of some advanced algorithms (e.g., maximal ball method) to extract the pore-network of the porous space (Silin et al., 2003; Silin & Patzek, 2006; Al-Kharusi & Blunt, 2007; Dong & Blunt, 2009). The second method is process-based method, which simulates the

packing of grains followed by geological processes such as sedimentation, compaction, and diagenesis by which sedimentary structures were formed (Øren & Bakke, 2002; Bryant et al., 1993b,a). The third approach is to use a statistical model to generate synthetic 3D structures that capture the properties of two dimensional (2D) thin sections (Wu et al., 2006; Okabe & Blunt, 2007). Besides the 3D representation of the pore spaces, the straight capillary tube bundle model represents the pore space in an alternative simple but physically-sound way (van Dijke & Sorbie, 2002a; Dong et al., 2005; Helland & Skjæveland, 2006b; Lindquist, 2006).

2.1.1 Extraction of pore-network from 3D rock images

Two major algorithms, the maximal ball (Silin et al., 2003) and medial axis based method (Lindquist & Venkatarangan, 1999), have been developed to extract pore networks from arbitrary 3D images. The maximal ball algorithm pioneered by Silin et al. (2003) and Silin & Patzek (2006), is based on generating balls in the center position of each voxel representing void in the image that just fit in the pore space; the largest maximal balls that are surrounded by smaller balls define the pores. Al-Kharusi & Blunt (2007) developed a more comprehensive set of criteria that include sphere clusters to handle equally sized balls. However, this extended algorithm is limited to relatively small systems containing fewer than a thousand pores, and it tends to form pores with lots of connected throats. Instead of growing a ball layer by layer, Dong & Blunt (2009) defined a void ball by developing a two-step searching algorithm to find the nearest solid; they also invented a clustering process to define pores and throats by affiliating the maximal balls into family trees according to their size and rank.

The medial axis based algorithms transform the pore space into a medial axis, which mathematically preserves the topology of the pore space and consequently the pore space is acting as a topological skeleton roughly running along the middle of pore channels (Lindquist & Venkatarangan,

1999). Pore-space partitioning can be validated along the skeleton to decide the pore throats by local minima along branches and pore bodies at the nodes.

Recently, statistical methods were adopted to generate pore networks from 3D rock images. Initially, the statistical information were obtained from a pore network that is extracted directly from a 3D digital image of the pore space (Jiang et al., 2012); later the multi-scale pore-network was proposed by considering the pore space with several statistical properties at various scales (Jiang et al., 2013).

2.1.2 Construction of 3D pore spaces from 2D rock images

For relatively large sample sizes, the resolution of x-ray CT scanning may not be high enough to resolve micro-porosity found in many carbonate reservoirs. In this case, 2D thin-section SEM images can be used to reconstruct the 3D pore space with a reasonable resolution by process-based modeling or stochastic reconstruction. The process-based method was developed by Bryant et al. (1993a,b), who simulated the process of quartz cementation by modeling close packing with equally-sized spheres, followed by processes such as swelling the spheres uniformly and allow them to overlap and compact by vertically moving the centers. The pore space can be tessellated into cells and pore networks can be generated by assigning cells as pores and cell faces as throats. Later this approach was extended to more complicated geometries by packing spheres of different size (Øren et al., 1998; Øren & Bakke, 2002, 2003). The simulated rock images produced a good agreement with micro-CT images of Fontainebleau and Berea sandstone in terms of morphological properties, such as two-point correlation functions, local porosity distributions and local percolation probabilities, and petrophysical properties, such as absolute permeability and formation factor (Valvatne et al., 2005).

Besides process-based methods, various statistical ones were developed to reconstruct 3D pore space from 2D rock images (Quiblier, 1984; Adler

et al., 1992; Yeong & Torquato, 1998). These methods recreate the 3D pore space by matching single- and two-point statistics derived from the input 2D images, but they fail to reproduce the long-range connectivity of the original pore space, for example in rocks with low porosity. To overcome this problem, Okabe & Blunt (2007) developed multi-point statistical methods. However these iterative multi-point methods are very computationally demanding. To reproduce the connectivity and shapes of the pore structures, several reconstruction approaches have been recently proposed; for instance, the multiple-point method or the five-point stencil method using a Markov chain Monte Carlo model (Wu et al., 2006), which reproduce typical patterns of the void space seen in 2D and consequently preserve the long-range connectivity. These statistical methods produce high resolution 3D images derived from their original 2D inputs with similar morphological statistics.

2.1.3 Straight capillary tubes bundle model

Although 3D representation of pore spaces gives more realistic characteristics of porous media, it is time demanding to conduct CFD in such pore structures, and thus the straight capillary bundle tube representation of pore space is still broadly used as it provides a simple, yet physically-sound approach for mathematical modeling of multiphase flow and displacement in porous media (Kovscek et al., 1993; van Dijke & Sorbie, 2002a; Dong et al., 2005).

The first type of capillary tube bundle model represents the pore spaces as analytical and simple cross-sections of straight tubes; in this type of model a distribution function is necessary for evaluating the pore size. Dong et al. (2005) developed an interacting tube bundle model, in which the pore spaces is formed by circular capillary tubes with a uniform size distribution. Angular geometries were also adopted to represent the tube cross sections, e.g., tubes having equilateral, triangular cross-sections. The geometry of an equilateral triangle is described by the half-angle

of the corner and the radius of the inscribed circles and the pore-size frequency can be given by a truncated two-parameter Weibull distribution (Diaz et al., 1987; Hui & Blunt, 2000; Helland & Skjæveland, 2006a; Wang & Dong, 2011).

As rock images become more available, realistic, highly irregular pore spaces can be extracted and used in the calculations. Lindquist (2006) considered capillary tubes with arbitrary, yet relatively convex, polygonal cross-sections. However, the assumed degree of convexity reduces direct utilization of tubes with irregular cross section that include converging/diverging geometry and high degree of surface roughness. Recently, Frette & Helland (2010) extracted the 2D realistic irregular-shaped pore geometries directly from 2D rock images and treated them as cross sections in straight tubes; the extracted pore spaces were represented by a smooth pore boundary applying the Euclidean path method (Braquelaire & Vialard, 1999).

2.2 Pore scale modeling computation methods

There are two main approaches to compute multiphase flow in the pore space. The first is to directly apply CFD in pore space; the second is to represent the pore space by a pore-throat network and then compute flow and transport through this network. Relatively simple, yet physically based, dynamic modeling could also be implemented with the capillary tube bundle models.

2.2.1 Direct application of CFD in rock images

CFD models can be classified as either particle- or grid-based. Examples of particle-based methods are the Lattice-Boltzmann (LB) which uses particle probability distribution function and the smoothed particle hydrodynamics (SPH) methods. The main grid-based methods include the level set (LS), volume of fluid (VoF), phase field method and the

morphology-based methods. As the name implies, particle-based models use particles to represent packets of fluid; the particles are tracked through the computational domain, and consequently allow to determine averaged fluid properties, such as pressure and density.

Particle-based methods

LB method is the most popular approach for computing single and multiphase flow directly on pore-space extracted from rock images (Ahrenholz et al., 2006; Boek & Venturoli, 2010; Ramstad et al., 2010). This method represents fluid dynamics at mesoscopic level by solving the discretized Boltzmann equation; LB is different from schemes that are based on a discretization of the Navier-Stokes equations, and thus represent balance equations at the continuum level.

An important advantage of LB method is that many properties related to fluid-solid and fluid-fluid interactions can be implemented in a straight forward manner without having to include complicated kernels (Martys & Chen, 1996). Moreover, LB method is relatively easy to code and is ideally suited for parallel computing platform; consequently it is relatively easier to compute single-phase flow properties and transport, such as permeability, dispersion coefficients and effective reaction rates (Manz et al., 1999; Manwart et al., 2002; Hiorth et al., 2013). However, the LB method is time demanding especially for two- or multi-phase flow, even with parallel implementation. Recent research indicates that with the best computer resources, it is possible to compute relative permeability curves based on pore-space images (Martys & Chen, 1996; Ramstad et al., 2010; Sheng et al., 2011; Ramstad et al., 2012).

Another group of simulation methods that has been applied successfully to study fluid transport is the SPH approach (Hu & Adams, 2006; Tartakovsky & Meakin, 2006; Kordilla et al., 2013), which can be seen as upscaled formulations of molecular dynamic in which particles represent fluid volumes. In the SPH method, it is relatively easy to add complex

physical, chemical and biological processes into particle codes. However, similarly with other particle based methods, the computational efficiency is low relative to grid methods. Multi-scale particle methods and hybrid (particle-particle and particle-grid) methods may be the future extension that could be applied to make an effective use of emerging computational capabilities (Kordilla et al., 2013).

Grid-based methods

The main advantage of grid-based methods, compared with particle based ones, is their computational effectiveness. Main grid-based methods are finite element method, finite volume method and finite difference method to solve Navier-Stokes equations. Multiphase problems require also interface tracking or interface capturing methods, such as the LS (Sethian, 1999), VoF (Raeini et al., 2012) and phase field methods (Jacqmin, 1999; Akhlaghi Amiri & Hamouda, 2013).

The LS method (Sethian, 1999; Osher & Fedkiw, 2003) is an interface tracking approach, which describes the interfaces implicitly as the zero level set function that is one dimension higher than the interface. This method has no constraints on the topology of the interface, and thus it well suited for modeling capillary dominated displacements in complex pore geometries. Prodanović & Bryant (2006) extended the application range of the level set method to model critical displacements events, such as Haines jump and snap-off, during drainage and imbibition as well as complete capillary pressure curves in 3D rock images. Fractured media have been also investigated via the LS method (Prodanović et al., 2010). In these applications, a second level set function was introduced to describe the pore structure and a "no-penetration" constraint (Sethian, 1999) was enforced at the end of each time step to prevent the fluid interfaces from invading the solid matrix. The limitation is that only strongly wetting conditions ($\theta = 0°$) can be simulated (Prodanović & Bryant, 2006); this shortage was addressed by (Jettestuen et al., 2013) who introduced a level set method for simulating capillary-controlled displacements

with *nonzero* contact angles in pore geometries of arbitrary shape from 3D rock images.

The VoF method is a simple and economical way to track free interfaces in 2D and 3D meshes (Hirt & Nichols, 1981; Ferrari & Lunati, 2013). This method treats the immiscible phases as a single fluid with variable properties and the distribution of the phase is described by a fluid function that carries information about the phase. The interfaces are identified as the region in which the gradient of the fluid function is nonzero. The contact angle can be accounted by imposing an appropriate boundary condition to the direction of the fluid-function gradient at the solid wall. Raeini et al. (2012) conducted pore scale modeling of two-phase flow by discretization of the governing differential equations with finite volume method and tracking the interface with VoF method. The relationship between capillary pressure and total surface energy was also investigated by this method (Ferrari & Lunati, 2013); the authors also demonstrated that the method is able to deal with large viscosity contrasts and model the transition from stable flow to viscous fingering.

The phase field method is also known as diffuse-interface method, the history of this approach goes back to a century ago when van der Waals (1979) used a density function that varies continuously at the interface to model a liquid-gas system. The best known example of phase field method is the convective Cahn-Hilliard equation that can conserve the volume and is relatively easy to implement in two and three dimensions (Cahn & Hilliard, 1958; Jacqmin, 1999; Akhlaghi Amiri & Hamouda, 2013).

Morphology-based method

A completely different, yet, discrete approach for modeling capillary dominated flow is the morphology-based method. Maximal inscribed ball (or sphere) (MIS) algorithm is one of the most popular morphology-based methods to model capillary equilibrium fluid configurations at the pore

scale (Silin et al., 2003; Silin & Patzek, 2006), and is also capable of extracting pore-networks from high resolution 3D rock images (Al-Kharusi & Blunt, 2007; Dong & Blunt, 2009). The MIS method has the capability to compute capillary pressure curves and fluid configurations in 3D rock images and the results show a reasonable agreement with results obtained from mercury injection experiments (Silin et al., 2003; Silin & Patzek, 2006; Silin et al., 2011). Silin & Patzek (2006) also formulated a new dimensionless capillary pressure function to improve the traditional J-function. Similarly to MIS algorithm, Virnovsky et al. (2009) computed capillary pressure curves using capillary tubes with arbitrary cross-sections obtained from 2D rock images. The MIS algorithm can only simulate strongly water-wet conditions for drainage processes, although efficient ways of including effects of wettability has been proposed (Silin et al., 2012).

Besides the MIS based method, Lindquist (2006) has shown the connection between arc-menisci configurations and the medial axis of a polygonal cross section and the entry conditions were determined under uniform strongly water-wet conditions. Lately, this medial axis based model has been extended to include simulating chord axes for arc-menisci configuration in an imbibition process for any wetting angle from 0° to 90° (Kim & Lindquist, 2012).

Even though the above two types of morphology-based methods have proven continuous contribution for capillary dominated displacement, they lack of a thermodynamical foundation. Recently, Frette & Helland (2010) developed a semi-analytical model which is based on combining all determined geological allowed arc menisci and applying the Mayer, Stowe and Princen (MS-P) equation (Mayer & Stowe, 1965; Princen, 1969a,b, 1970; Ma et al., 1996) to compute the entry pressure under arbitrary wetting conditions for a non-wetting phase invading a wetting phase filled capillary tube that contains highly irregular cross sections. This semi-analytical model was also extended to compute capillary pressure curves under mixed-wet conditions (Helland & Frette, 2010), which allows neg-

ative capillary pressure between oil and water.

2.2.2 Pore-Network Modeling

Since the pioneering work of Fatt (1956), pore-network models have become one of the main fields of research in the porous media discipline. Two primary types of pore-network modeling tools, the quasi-static and dynamic network, could be defined by the flow regime based on the value of capillary number. The capillary number, CA, denotes the ratio of viscous forces to capillary forces during the displacement in the porous medium, and it is defined as

$$CA = \frac{\mu q}{\sigma A}, \tag{2.1}$$

where μ is viscosity, q flow rate, A is cross-sectional area of the porous medium and σ denotes the interfacial tension.

Quasi-static pore-network modeling

If the capillary number is smaller than 10^{-5}, based on the fluid displacement mechanisms (see Section 2.4) a quasi-static pore network modeling could be applied to simulate the equilibrium positions of fluid-fluid interfaces, and thus determine the capillary pressure and relative permeability curves in the pore space (Blunt, 1997a; Øren et al., 1998; Valvatne et al., 2005; Piri & Blunt, 2005).

Dynamic pore-network modeling

Dynamic pore-network models are normally applied when the capillary number is larger than 10^{-5}, as the viscous forces cannot be neglected. In the dynamic pore scale models, at each time step the pressure distribution in the network is calculated first followed by the fluid-fluid interfaces based on pressure difference criteria. The dynamic pore scale models were used to investigate the effects of capillary number and viscosity ratios on the

relative permeability, residual oil saturation and pore scale displacement mechanisms (Blunt & King, 1991; Dahle & Celia, 1999). The balance between piston-like and snap-off displacement (see Section 2.4), and its effect on residual oil could be examined if the flow through thin wetting films is also included in the dynamic pore-network models (Blunt & Scher, 1995; Hughes & Blunt, 2000; Joekar-Niasar et al., 2010).

2.2.3 Interacting tube bundle model

Tube bundle models represent a simplified pore-scale modeling approach that could be utilized to study qualitatively multiphase flow in porous media (Ruth & Bartley, 2002; Dong et al., 2005; Wang & Dong, 2011). For example, Dong et al. (2005); Wang & Dong (2011) developed a so-called interacting tube bundle model where phase-pressure equilibration exists in both oil and water phases. This implies that the phase pressures vary with distance along the tube length, but remain constant at each cross-section. The assumption of phase pressure uniqueness at each cross-section causes the meniscus with the largest capillary pressure and velocity to advance in front. Ruth & Bartley (2002) developed a similar model which was referred to as a perfect cross-flow model. They considered adjacent tubes that are not separated completely by solid walls since phase pressure equilibration at each bundle cross-section was assumed to be maintained by resistant-free cross-flow between the tubes. In both models, the phase pressure constancy in each section implies that the flow rate of each phase in a given tube may be different in the length regions along the bundle, whereas the total flow rate in all length regions is constant. These models have been shown to be consistent with core-scale models that are based on the standard two-phase modification of Darcy's law (Ruth & Bartley, 2002). Unsal et al. (2007a,b) performed imbibition flow experiments in a tube constructed by the space between a rod and a glass plate and demonstrated that the saturation fronts computed with an interacting tube bundle model agreed very well with the experimental results. More recently, Wang & Dong (2011) developed an interacting

tube bundle model with triangular tube cross-sections in which both fluids can coexist at the same tube cross-section. They also investigated trapping of oil during water flooding by assuming that the size and distribution of the triangular tube cross-sections varied with positions along the tube bundle length.

2.3 Wettability

Wettability is one of the essential properties that control multiphase flow in porous media as it affects the distribution and transport behavior of fluids during displacement. Several methods have been applied to quantify the wettability of a porous rock, such as contact angle measurements and wetting indexes computed from capillary pressure curves (Cuiec, 1991). However, wettability classification of reservoir as water-wet or oil-wet is a gross oversimplification (Morrow, 1990; Cuiec, 1991). Recent advanced imaging techniques allow us to investigate the wettability distribution down to pore scale and thus provide physical fundamental knowledge to establish pore scale wettability models, which could increase the insight of multiphase flow in porous media (Kumar et al., 2009, 2012).

2.3.1 Wettability alteration

Hydrocarbon reservoirs are initially saturated with water and generally considered as uniformly water-wet (Tiab & Donaldson, 2004; Dandekar, 2006). This uniformly wetting state may change to either a homogeneous oil-wet state, or to a mixed-wet state, in which some parts of the rock surface become oil-wet while other parts remain water-wet (Donaldson & Alam, 2008). Hydrocarbon components (e.g., asphaltenes) that get adsorbed on the pore surface, when the hydrocarbon phase invades from the source rock, is the necessary condition of wettability alteration. In order to have an effective hydrocarbon-components adsorption, the pressure difference between the oil and water phases needs to be sufficiently

high, first to overcome the capillary entry pressure and second to overcome the critical pressure when thin water films collapse (Kovscek et al., 1993).

The first necessary condition of wettability alteration during primary drainage is that the pressure difference exceeds the capillary entry pressure. This is because only the part of the pore space exposed to crude oil could result in wettability changes on both core and pore scales (Masalmeh, 2003). The capillary entry pressure depends on several parameters, such as pore shape, pore size, interfacial tension and pore surface wettability. General speaking, the capillary entry pressure can be quantified by the so called MS-P equation (Mayer & Stowe, 1965; Princen, 1969a,b, 1970; Ma et al., 1996); please refer to Section 2.5 for a review of the capillary entry pressure for piston-like invasion.

After primary drainage, most of the original water has been displaced from the pores by oil, leaving water only in the pore corners/necks and as thin water films along the solid surfaces. The stability of the water films depend on the disjoining pressure and the geometry of the solid surface, and the critical pressure when the thin films start to collapse can be examined by the augmented Young-Laplace equation (Hirasaki, 1991b,a; Kovscek et al., 1993; Frette et al., 2009). The local curvature of a pore wall has a significant effect on the critical pressure.

Kaminsky & Radke (1997) discussed whether wettability alteration can occur in pores with intact the films due to asphaltene diffusion across the water film, which however is a much more time consuming process. The authors concluded that this process is not sufficient to initiate significant wettability alteration. While more recent studies performed using advanced imaging techniques generally support this conclusion, Kumar et al. (2009); Kumar & Fogden (2010); Kumar et al. (2012) also observed that the deposition of crude oil components slightly intruded the water/solid area in pore geometries saturated by both oil and water. Hence, after primary drainage and through the geological time, the reservoir rock might therefore end up with three distinctively different simultane-

ous wetting populations, namely strongly water-wet, where oil has not invaded, oil-wet, where the water films have collapsed, and weakly to strongly water-wet, where the films remain.

2.3.2 Mixed-wettability model

The pore scale model proposed by Kovscek et al. (1993) is currently the most acceptable theoretical model for mixed-wet conditions. In this model, the pore space is represented by capillary tubes with four-cornered curved star-shape cross-sections that are formed by four touching spheres; and thus the critical capillary pressure required for a thin water film collapse decreases with decreasing pore size. In their model, three types of wetting states could be formed after drainage. The smaller pores do not get invaded by oil and remain water-wet as the maximal drainage capillary pressure is smaller than the capillary entry pressure. The medium-sized pores become mixed-wet as the water filled corners remain water-wet and the middle portions of the pore walls, that are contacted by oil, become oil-wet. The larger pores invaded by oil remain water-wet as the critical capillary pressure has not been exceeded at the end of the drainage process and the protective water films are still stable. As explained by Kovscek et al. (1993), the wetting state after primary drainage depends strongly on maximal drainage capillary pressure and the pore wall curvature. For example, for curved convex pore shapes (e.g., eye-shaped), the larger pores become mixed-wet and the smaller pores remain water-wet.

Contact angle hysteresis could be incorporated in a mixed-wet model by introducing contact lines that get pinned while the corresponding arc meniscus hinges at an angle which changes according to capillary pressure (Ma et al., 1996). This conceptual hysteresis model has been used broadly in pore-network modeling to investigate the hysteresis effects on multiphase flow in mixed-wet porous media (Øren & Bakke, 2003; Piri & Blunt, 2004, 2005; Helland & Skjæveland, 2006b; Ryazanov et al., 2009; Helland & Frette, 2010; Kim & Lindquist, 2012).

Recently, advanced imaging techniques based on micro-CT have been utilized to investigate the microscopic wetting state directly in porous materials (Kumar et al., 2009; Kumar & Fogden, 2010; Kumar et al., 2012). Generally, it was demonstrated that deposition of crude oil components occurred in regions exterior to the bulk water phase and at locations where thin water films ruptured. These results support the pore scale mixed-wet model proposed by Kovscek et al. (1993) and are also in agreement with the study of Kaminsky & Radke (1997). However, Kumar et al. (2009); Kumar & Fogden (2010); Kumar et al. (2012) argue that the mixed-wettability model (Kovscek et al., 1993) could be potentially improved by including a transition zone near the contact line, as deposition of crude oil components is observed to occur non-uniformly at a finite distance outside of the remaining bulk water phase.

2.4 Pore scale displacement mechanisms

During drainage processes in strongly water-wet systems, the accessible pore throats and their neighboring pore bodies are invaded in order of increasing capillary entry pressure by piston-like displacement (see for example, Al-Futaisi & Patzek (2003)). Another particularly important pore scale displacement during drainage is the Haines jump which shows a sudden drop in capillary pressure when the non-wetting phase passes from a pore throat through a series of several wider pore bodies and throats until new stable interface positions are reached in narrower throats (Haines, 1930; Morrow, 1970; Berg et al., 2013). For imbibition processes the pore level displacements, snap-off and pore body filling, have been observed from water-wet micro-model experiments in addition to piston-like invasion (Lenormand et al., 1983). Oil layer formation and collapse is another type of displacement that can occur for mixed-wet conditions in two-phase systems and even for uniform-wet conditions in three-phase systems (Kovscek et al., 1993; Blunt, 2001). Finally, in three-phase flow double and multiple displacements are important mechanisms that have

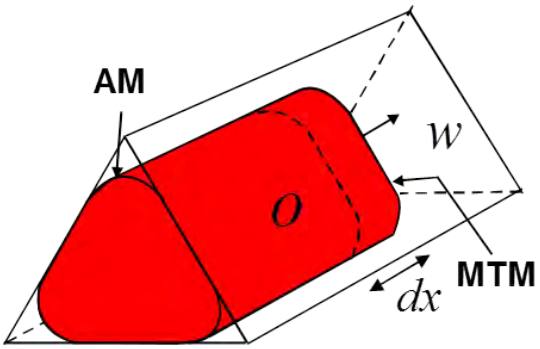

Figure 2.1: A sketch of arc meniscus (AM) and main terminal meniscus (MTM) in a triangle capillary tube.

shown to high impact on residual oil (van Dijke & Sorbie, 2003a; Al-Dhahli et al., 2013). In this section, these displacement mechanisms will be introduced and briefly discussed.

2.4.1 Piston-like invasion

The non-wetting phase enters a pore throat filled with wetting phase only if the capillary pressure is equal to or greater than a given capillary pressure, namely the capillary entry pressure (Lenormand et al., 1983). The invading interface moving in the direction along the tube, separating the bulk fluids, is referred to as the main terminal meniscus (MTM), and the interface located in the corners of the cross-section, separating the bulk fluid from corner fluid, is referred to as the arc meniscus (AM). A sketch illustrating the AMs and MTM in a triangle capillary tube is presented in Figure 2.1. Capillary entry pressure for this kind of piston-like invasion can be determined by balancing the work of displacement with the change in surface energy or, equivalently, by considering the forces required to maintain thermodynamical equilibrium (Mayer & Stowe, 1965; Ma et al., 1996).

For the imbibition process of mixed-wet conditions, contact angle hys-

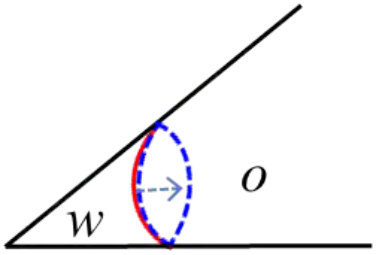

Figure 2.2: A sketch of hinging interface to account for hysteresis in imbibition.

teresis is modeled by introducing a hinging interface with pinned contact lines (see Figure 2.2) that separates the remaining corner water and center oil and thus allowing the contact angle to change at this position in order to maintain capillary equilibrium (Ma et al., 1996; Valvatne et al., 2005; Piri & Blunt, 2005; Helland & Skjæveland, 2006a; van Dijke & Sorbie, 2003b; van Dijke et al., 2007). The interface does not move until the hinging contact angle reaches the advancing contact angle. The capillary entry pressure for the piston-like displacement during imbibition is again found by calculating the force balance acting on the interface. For spontaneous imbibition, the capillary entry pressure is calculated similarly as in drainage if the hinging contact angle has reached the advancing contact angle. If this is not the case, such as in forced imbibition (negative capillary pressure), the entry pressure is affected by the initial configuration and the fraction of oil-wet and water-wet pore wall areas (Piri & Blunt, 2005; Helland & Skjæveland, 2006b; Helland & Frette, 2010).

A more detailed literature review of capillary entry pressure for piston-like invasion will be given in Section 2.5.

2.4.2 Layer formation and collapse

Two types of fluid layers can form in a multiphase displacement process in a pore throat. Depending on whether the fluids residing on the two

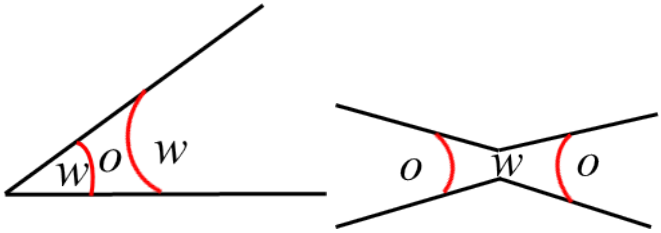

(a) $P_{c,ow} < 0$ (b) $P_{c,ow} > 0$

Figure 2.3: Layer types surrounded by identical fluids.

opposite sides of the layer are the same, layers may be categorized as layers surrounded by identical fluids or different fluids.

Layer type

Layers of oil surrounded by identical fluid (water) have a sandwiched shape and can exist at negative capillary pressure during forced imbibition in mixed-wet pore spaces (Kovscek et al., 1993; Blunt, 1997b; Piri & Blunt, 2004; Helland & Skjæveland, 2006a; Helland & Frette, 2010) as shown in Figure 2.3(a). However, this sandwiched shape layer type can also occur in pore necks during primary drainage process (Frette & Helland, 2010), in which water is the layer fluid surrounded by oil, see Figure 2.3(b).

Layers surrounded by different fluids are formed by intermediate-wet phases (e.g., oil) that are located between the wetting phase (e.g., water) in the pore corner and non-wetting phase (e.g., gas) in the pore center, see Figure 2.4(a) (Dong et al., 1995; Keller et al., 1997; Blunt, 1997a; Hui & Blunt, 2000). This type of layers is experimentally observed in micro-models (Keller et al., 1997) and has also been explained thermodynamically in non-circular capillary tubes both for uniformly- and mixed-wet conditions (van Dijke et al., 2004, 2007). Recently, Feali et al. (2012) conducted a high resolution X-ray micro-tomography to image the distribution of oil, water and gas after tertiary gas flooding in strongly

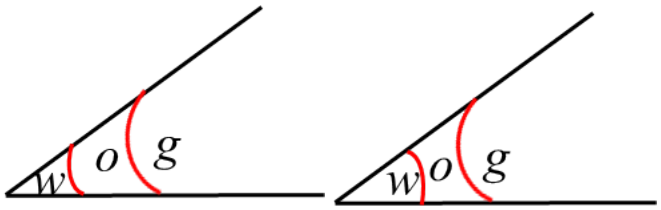

(a) $P_{c,ow} > 0$ (b) $P_{c,ow} < 0$

Figure 2.4: Layer types surrounded by different fluids.

water-wet Bentheimer sandstone and they found that spreading systems clearly display oil-layer behavior, while non-spreading ones display fewer oil layers. Figure 2.4(b) shows an example when the pore space becomes oil-wet, and thus oil layers may forme between gas and water at negative oil-water capillary pressure (Piri & Blunt, 2004; Helland & Skjæveland, 2006b; van Dijke et al., 2007).

Layer collapse criteria

The first criterion for layer collapse is purely geometrical and assumes the fluid layers would collapse when the surrounding oil-water interfaces meet (Blunt, 1997b). This criterion has been used for formation and collapse of oil layers in capillary bundles (Hui & Blunt, 2000) and network models (Øren et al., 1998; Piri & Blunt, 2004; Valvatne et al., 2005; Piri & Blunt, 2005).

In contrast to the geometrical criterion, a thermodynamical-based criterion was also developed for the existence of oil layers in two- and therephase systems (van Dijke et al., 2004, 2007). This criterion is consistent with the MS-P capillary entry pressures for other types of piston-like invasions. The thermodynamical-based criterion was implemented both into a capillary bundle model (Helland & Skjæveland, 2006a) and pore-network modeling (Ryazanov et al., 2009; Al-Dhahli et al., 2013) to model layer collapse. Ryazanov et al. (2009) compared the existence of oil layer

based on the geometrical and thermodynamical criteria and concluded that the geometrical criterion tends to maintain the existence of oil layers even when the thermodynamical-based criterion predicts that such layers should not exist. Recently, Al-Dhahli et al. (2013) implemented a thermodynamical criterion to allow for oil layers into network modeling.

2.4.3 Haines jump

Haines jump manifests itself as a sudden drop in capillary pressure when the non-wetting phase passes from a pore neck into a wider pore body displacing the wetting phase (Haines, 1930). This displacement mechanism results from unstable fluid configurations and thus forms apparatus pressure fluctuations (Morrow, 1970). In porous media, it usually occurs in the form of interfaces that move through a series of several wider pore areas, during which they may split or merge, before reaching equilibrium positions in narrow throats.

Måløy et al. (1992) measured the pressure fluctuations resulting from Haines jump in a two-dimensional porous medium and developed an invasion percolation algorithm to simulate the pressure jump which shows agreement with the experimental results. Recently, Haines jump events were also observed to occur in level-set simulations of capillary controlled displacement in porous medium (Prodanović & Bryant, 2006; Jettestuen et al., 2013).

Besides the pore scale modeling, Berg et al. (2013) conducted real time imaging of fluids displacement in porous media and observed several important displacement characteristics (e.g., snap-off, Haines jump). The authors found that most Haines jump events do not displace the wetting phase pore-by-pore, but typically invade 10-20 individual pores and that drainage events are co-operative. The authors also found that 64% of the externally applied work is actually dissipated during these jumps; the remaining 36% of the applied work is converted into interfacial energy.

2.4.4 Snap-off

Snap-off corresponds to an imbibition event where wetting phase films start swelling until the interface becomes unstable, at which point the pore throat or body becomes entirely filled with wetting phase (Roof, 1970; Lenormand et al., 1983; Keller et al., 1997). This unstable displacement causes the non-wetting phase (e.g., oil) to form isolated clusters at narrow pore throats resulting in trapped compartments, bubbles or drops of non-wetting phase (Mohanty et al., 1987; Kovscek et al., 1993; Berg et al., 2013).

An isolated non-wetting phase resulting from snap-off constitutes residual non-wetting phase saturation during imbibition and it is one of the main sources of hysteresis in flow functions of porous media. However, in straight tubes with constant cross-sections snap-off only occurs if piston-like invasion is topologically impossible since the capillary pressure for piston-like invasion is favorable compared to the capillary pressure for snap-off (Hui & Blunt, 2000; Lenormand et al., 1983; Helland & Skjæveland, 2006b).

2.4.5 Pore body filling

Pore body filling refers to the displacement of one phase in the center of a pore by movement from the center of adjoining throats (Lenormand et al., 1983). The capillary entry pressure for pore body filling is determined by the largest radius of the curvature in the pore body, and thus it depends on the number of adjacent oil-filled throats (Lenormand et al., 1983). Empirical models are normally used to estimate the entry pressure for pore body filling events (Blunt, 1997a; Øren et al., 1998; Valvatne et al., 2005). Most of these empirical models for capillary entry pressure of pore body filling depend on the inscribed radius of the pore body, the number of connecting pore throats filled by non-wetting phase, random weighting coefficients, and aspect ratio between pore bodies and pore throats.

The selection of weighting coefficients for pore body filling events or aspect

ratios will affect the kind of displacement that is more likely to occur (Valvatne et al., 2005). For example, larger aspect ratios between pore bodies and pore throats make pore body filling less favorable compared to snap-off.

2.4.6 Three-phase multiple-displacement events

Multiple-displacement events occur when the injection of one fluid at the inlet of a network model triggers a chain of displacements that involves disconnected clusters of oil, water or gas, which span a connected displacement path from the inlet to the outlet (van Dijke & Sorbie, 2003a). This type of displacement mechanisms were observed in micromodel experiments (Sohrabi et al., 2000, 2001), and it is an extension of the double-displacement process discussed by Øren & Pinczewski (1995); Fenwick & Blunt (1998). Al-Dhahli et al. (2013) have implemented these multiple-displacement mechanisms into network to allow disconnected phase clusters to be mobile, especially during WAG injection, which provided better prediction of residual oil saturations.

2.5 Capillary entry pressure

Capillary entry pressure is the smallest capillary pressure required for the non-wetting fluid (e.g., oil or gas) to invade a capillary tube that is filled with wetting phase (e.g., water). This property is related to several important applications in reservoir engineering (e.g., oil migration from source rock to reservoir) as well as environment issues (e.g., potential leakage of CO_2 through the caprock of a storage site). A proper value of capillary entry pressure is essential for capillary pressure curves representation by correlations (van Genuchten, 1980; Brooks & Corey, 1964); pore network models also require the knowledge of capillary entry pressure for a non-wetting phase to invade pore throats (Blunt, 1997b; Piri & Blunt, 2004; Valvatne et al., 2005; Wang & Dong, 2011). Reliable prediction of

CO_2 plume behavior in a storage site requires the knowledge of capillary entry pressures for CO_2 that dictates the invasion into low-permeable and internal formation layers or cap rock (Li et al., 2005; Class et al., 2009).

The MS-P method (Mayer & Stowe, 1965; Princen, 1969a,b, 1970) was used for calculating capillary entry pressures into individual pore throats that are modeled as constant cross-sections and which are obtained by balancing the required work with the corresponding change in interfacial free energy for a virtual displacement of the invading MTM in the direction along the tube length. The details of MS-P method are given in Section 3.1.

2.5.1 Uniform wettability

Two-phase case

The capillary entry pressures for the equilateral triangular and square cross-sections under perfect wetting condition were derived using the so-called MS-P method (Princen, 1970). After the pioneering work of Mayer & Stowe (1965); Princen (1969a,b, 1970), this method has been extended to allow the computation of capillary entry pressure for many types of idealized pore shapes and wetting conditions (e.g., rectangular geometry at any uniformly wetting conditions (Legait, 1983); regular n-polygons with any contact angle (Mason & Morrow, 1984); arbitrary triangular shape at perfect wetting condition (Mason & Morrow, 1991); curved triangle cross section at different wetting conditions (Princen, 1992)).

Lago & Araujo (2001) derived a generalized equation for entry pressure computation in capillaries with irregular polygonal cross sections for any wetting condition. Analytical expressions of capillary entry pressure for idealized pore shapes were obtained by simplifying their generalized equation. The authors also extended their method for regular hyperbolic polygons (three and four corners) and some other cross-sections with curved boundaries (Lago & Araujo, 2003).

The MS-P method has been combined with the medial axis concept for computing entry pressures in simply-connected pore throat geometries with high degree of convexity and a zero contact angle (Lindquist, 2006). Held (2010) extended this work and derived an analytical solution for the same pore geometries. However, the assumption of relatively strong convexity in the throat cross-sections reduces a direct utilization of the method on segmented 2D images of rock samples, where the pores normally exhibit irregular shapes with converging/diverging geometries and high degree of surface roughness. Frette & Helland (2010) presented a semi-analytical model to compute two-phase capillary entry pressures and corresponding fluid configurations for any uniform wetting conditions in realistic, irregularly-shaped pore spaces directly extracted from segmented rock images and represented the pore walls by a smooth pore boundaries computed with a Euclidean path method (Braquelaire & Vialard, 1999).

Three-phase case

Fenwick & Blunt (1998) studied three-phase piston-like displacements by assuming that three-phase displacements are combinations of two-phase displacements, and derived capillary entry pressures for three phase displacements using the two-phase MS-P equation.

Dong et al. (1995) examined the thermodynamical existence of an intermediate layer in convex corner capillary tube both at spreading and non-spreading conditions. van Dijke & Sorbie (2003b) and van Dijke et al. (2004) extended the MS-P method to compute the three-phase capillary entry pressure in uniformly-wet angular idealized pore throat geometries. In this case the energy balance equation generally relates two entry radii of curvature to the geometry of the cross-sectional fluid configurations before and after the displacement of the MTM. In such three-phase situations, the capillary entry pressure for gas invasion into a pore throat occupied by oil in the pore center and water in the corners for example, also depends on the oil-water capillary pressure if the invading gas phase

displaces both oil and water. The same authors have also applied the energy balance principle to derive entry pressures for piston-like invasion of intermediate wetting fluid layers (e.g., oil) in the corners of angular pores; they concluded that the computed entry pressures are favorable compared to the commonly assumed geometric conditions for fluid-layer existence (e.g., Hui & Blunt (2000)).

2.5.2 Mixed wettability

Kovscek et al. (1993) presented the classic mixed-wet, pore model, in which the pore surface has both water-wet and oil-wet parts. Based on this model, the two- and three-phase capillary entry pressure for piston-like invasion were determined by extending the MS-P method.

Two-phase case

Ma et al. (1996) extended the MS-P method to determine the capillary entry condition in regular n-sides polygonal tubes, both for drainage and imbibition processes, in which the effect of contact angle hysteresis was included by introducing interfaces hinging at pinned contact lines. These capillary entry pressures have been implemented in pore-network models for mixed-wet conditions using arbitrary triangular and square throat cross-sections (Øren et al., 1998; Valvatne et al., 2005).

Helland & Skjæveland (2006a) presented a bundle-of-triangular tubes model, in which the MS-P method was used to derive the entry pressures in mixed-wet equilateral triangular tube cross-sections for all displacements in primary drainage, imbibition, secondary drainage and subsequent scanning curve loops. The layer collapse event was determined using the thermodynamical criterion proposed by van Dijke et al. (2007). Frette & Helland (2010) developed a semi-analytical method to simulate the capillary entry pressure and fluid configurations in realistic uniformly-wet pore shapes which later was extended by Helland & Frette (2010) to allow for mixed-wet conditions. This semi-analytical model account for

oil layer configurations at negative capillary pressures, and the thermodynamical criterion (van Dijke et al., 2007) was used to determine the condition under which an oil layer will collapse.

Three-phase case

Hui & Blunt (2000) computed the capillary entry pressure in three-phase systems based on the two-phase MS-P method, and used the geometrical criterion to identify the existence of intermediate oil layers. The three-phase MS-P equation (van Dijke & Sorbie, 2003b) was used to derive the entry pressures in mixed-wet conditions by extending the mixed-wet approach for two-phase systems (Ma et al., 1996). Piri & Blunt (2004); Helland & Skjæveland (2006a) determined the capillary entry pressures by choosing the most favorable displacement among all possible geometrically displacement scenarios. However, they still used the geometric criterion to determine the layer existence. Based on the MS-P theory, van Dijke et al. (2007) derived the entry conditions for all possible three-phase displacements including bulk and layer displacement for mixed-wet angular pores.

2.6 Capillary pressure curves

Capillary pressure is one of the most important variables for simulating multiphase flow in porous media at the continuum scale. It is known to depend on porous material properties such as permeability and porosity, as well as parameters describing the interaction between the rock and the fluids, conventionally described in terms of wettability and interfacial tension (Tiab & Donaldson, 2004; Anderson, 1987; Brooks & Corey, 1964).

2.6.1 Leverett's J-function

Leverett (1941) proposed a dimensionless J-function with the intention to describe different capillary pressure curves, for different permeabilities, porosities and interfacial tensions, by a single unique curve; this function is given by

$$J(S_w) = \frac{P_c(S_w)}{\sigma cos\theta}\sqrt{\frac{K}{\phi}}. \tag{2.2}$$

In this expression, the contact angle was added later in an attempt to describe different wetting conditions. Noaman (1995) modified the J-function by incorporating the media tortuosity and irreducible water saturation to account for reservoir heterogeneities.

It has been demonstrated, using measured drainage data in relatively homogeneous rocks at strongly water-wet conditions, that Leverett's J-function yields an almost unique dimensionless capillary pressure curve because capillary pressure is observed to increase with decreasing permeability (Leverett, 1941; Hamon, 2000). However, for imbibition at mixed-wet conditions, a weaker dependency of permeability on the capillary pressure is observed (Hamon, 2000), and hence the traditional J-function does not work satisfactorily.

2.6.2 Correlations

In water-wet reservoirs, two main types of correlations, Brooks & Corey (1964) and van Genuchten (1980), are normally used to represent capillary pressure curves in reservoir simulation. The *Brooks-Corey* correlation uses a plateau that ends with a nonzero capillary entry pressure and thus yields a convex-shaped curve, while the *van Genuchten* correlation uses a steep slope that connects the end-point to the plateau region, thus yielding an S-shaped curve.

Based on the *van Genuchten* correlation, Bradford & Leij (1995) added a term that includes the lowest capillary pressure value into the capillary

pressure part of the correlation to account for the mixed-wet conditions.

Skjæveland et al. (1998) suggested another correlation for mixed-wet capillary pressure curves, which is formulated as a sum of two *Brooks-Corey* functions. Separately, these functions describe either strong water-wet or oil-wet conditions, but combined they included four fitting parameters and can reproduce mixed-wet capillary pressure curves. Capillary scanning loops can be generated through this correlation, which has also been used to formulate physically-based correlations for mixed-wet capillary pressure curves computed from a bundle of triangular tubes model (Helland & Skjæveland, 2006a).

2.6.3 Three-phase capillary pressure curves

Three-phase capillary pressure curves can be measured in the laboratory from core samples (Kalaydjian, 1992; Virnovsky et al., 2004). Bradford & Leij (1995, 1996) measured three-phase capillary pressure curves in sandpacks under several wetting conditions achieved by mixing different fractions of oil-wet and water-wet sands. However, because the three-phase capillary pressure measurements are time-consuming and technically complicated, the common practice is to determine these relationships using correlations that have been formulated based on much more readily available two-phase data (Baker, 1998; Lenhard & Parker, 1988; van Dijke et al., 2001).

As an alternative, Helland & Skjæveland (2006b) extended the MS-P method to three-phase systems and computed three-phase capillary pressures at mixed-wet conditions in a bundle-of-tubes model, and they formulated physically-sound correlations for mixed-wet, three-phase capillary pressure curves based on simulated capillary pressure data (Helland & Skjæveland, 2004).

2.7 Dynamic effects in capillary pressure

In several reservoir multiphase flow processes, especially in natural fractures and near wellbore, both viscous and capillary forces determine the pore-scale fluid configurations due to high flow rates (Hughes & Blunt, 2000). This could give rise to significant dynamic effects in the capillary pressure relation because the fluids are redistributed faster than the relaxation time required for them to reach a capillary equilibrium state.

Dynamic capillary pressure is defined as the intrinsic phase pressure difference at any time and fluid saturation; a detailed literature review of dynamic capillary pressure can be found in Diamantopoulos & Durner (2012).

Two main theories have been proposed in the literature for incorporating dynamic effects in constitutive relations (Barenblatt & Vinnichenko, 1980; Silin & Patzek, 2004; Hassanizadeh & Gray, 1993; Hassanizadeh et al., 2002). The first one is the Barenblatt model that accounts for dynamic effects in both capillary pressure and relative permeability by relating the dynamic quantities to the actual water saturation, and the static quantities to a so-called future water saturation (Barenblatt & Vinnichenko, 1980; Silin & Patzek, 2004). The difference between the actual and future saturations is related to the time rate of saturation change. The second is the Hassanizadeh and Gray model that accounts for dynamic effects in capillary pressure only through the relationship (Hassanizadeh & Gray, 1993),

$$P_c^{dyn} - P_c^{stat} = -\tau \frac{\partial S_w}{\partial t}, \tag{2.3}$$

where the dynamic and static capillary pressures are given by P_c^{dyn} and P_c^{stat}, respectively, and τ is the dynamic capillary coefficient which has been reported to depend on the porous material properties, such as porosity, permeability and domain size, as well as fluid properties and fluid saturation (Bottero et al., 2006; Dahle et al., 2005; Hassanizadeh et al., 2002; Camps-Roach et al., 2010; Goel & O'Carroll, 2011; Mirzaei & Das,

2007; Hanspal & Das, 2012).

2.7.1 Experimental investigation of dynamic effects

Several attempts of measuring dynamic capillary pressure in core samples have been reported, and the results have shown that during a drainage process the value of dynamic coefficient, τ, is a function of saturation and independent on desaturation rate (Bottero et al., 2006; Schembre & Kovscek, 2006; Camps-Roach et al., 2010; O'Carroll et al., 2010). The dependence of τ on water saturation was determined from laboratory experimental; Bottero et al. (2006) reported a non-monotonic behavior of τ with saturation, which shows a decreasing trend from small to larger wetting phase saturations until it reaches a value close to 0.7, and then it starts to increase. In contrast, a decreasing exponential relationship between τ and saturation has been reported both experimentally and numerically (Das & Mirzaei, 2012). Recently, Bottero et al. (2011) performed drainage experiments with high viscosity ratios and found that τ increases with a decrease of the wetting phase saturation; this behavior was also observed by pore scale modeling (Joekar-Niasar et al., 2010).

The dependency of τ on permeability was investigated by Camps-Roach et al. (2010); Das & Mirzaei (2012); they reported larger τ in lower permeability porous media which shows the same trend as the empirical relationship proposed by Staffer (1978). Camps-Roach et al. (2010) and Das & Mirzaei (2012) also argued that τ is scale independent; however Bottero et al. (2011) reported larger values of τ at a larger length scale, and thus they concluded that τ is strongly scale dependent.

O'Carroll et al. (2010) investigated the influence of rock wettability on dynamic effect in capillary pressure by conducting two phase multi-step outflow measurement in chemically treated sand packs that possess different wettability, namely contact angles. Their results showed that it might be reasonable to neglect dynamic effects in capillary pressure in systems that approach intermediate-wet conditions, but that these effects will be

increasingly important in more water-wet systems.

Recently, Mirzaei & Das (2013) investigated the hysteresis effects in dynamic capillary pressure. They found that at a particular water saturation, the magnitude of τ is generally higher for imbibition than that for drainage.

2.7.2 Numerical modeling of dynamic effects

Although there has been a growing number of experimental work aimed at investigating the dynamic effects in capillary pressure curves, a full study of their significance has been difficult since such measurements are challenging because of the difficulties associated with accessing the intrinsic phase pressures and saturations at different locations inside the samples. Some quantities, such as fluid distributions and local phase pressures, are hard to measure and the experiments are costly and time-consuming. Besides experimental investigations of dynamic effects in capillary pressure curves, numerical modeling allow us to quantify more realistic and complicated conditions, e.g., heterogeneity, fluid properties.

The first type of modeling approach is the continuum scale modeling (Mirzaei & Das, 2007). The authors investigated the effects of micro-heterogeneities on dynamic coefficient and found that, as the intensity of heterogeneity increases, the dynamic coefficient τ at a given saturation increases. The second type of modeling approach uses pore scale modeling. Dahle et al. (2005) used a non-interacting tube bundle model with tubes of circular cross-sections and reported that τ increases with a decrease of wetting fluid saturation. A similar trend for the variation of τ with saturation was also observed by a dynamic pore-network modeling approach (Joekar-Niasar et al., 2010; Joekar-Niasar & Hassanizadeh, 2011). Fluid properties, such as viscosity ratio and effective viscosity, were fully investigated by the dynamic pore-network modeling approach. Contrary to recent experimental observations (Mirzaei & Das, 2013), no significant difference was observed in τ-saturation relationship for drainage and

imbibition (Joekar-Niasar & Hassanizadeh, 2011).

Although some aspects of non-equilibrium capillarity effects have been studied, there is still much room for further studies. For example, the dynamic effects in mixed-wet porous media and their impact on the initial water saturation during imbibition have not been studied before.

2.8 Thesis Objectives

The goal of this work is to shed light on the capillary pressure modeling in realistic pore spaces which are represented as straight tubes with cross section extracted from rock images.

The research approach is based on a realistic two-dimensional description of pore space taken directly from rock images, i.e., by avoiding idealized representation of the pore space by pore network. A semi-analytic method (Frette & Helland, 2010; Helland & Frette, 2010) which models quasi-static displacements based on the principle of minimum free energy in arbitrary 2D pore shapes, is adopted as the basis for this work. This model is developed further to simulate, directly on segmented 2D rock images, two-phase capillary pressure curves and fluid configurations for imbibition at mixed-wet conditions, as well as capillary entry pressures, related fluid configurations and capillary pressure curves at uniformly-wet conditions for three-phase fluid systems. The transient behavior of interfaces will be modeled by extending the interacting tube bundle model proposed by (Dong et al., 2005; Wang & Dong, 2011) to allow arbitrary pore shapes, and combine it with the determined capillary pressures and fluid configurations from the semi-analytical approach.

The main thesis objectives are therefore to:

- Compute two-phase capillary pressure curves and fluid configurations for uniformly- and mixed-wet conditions directly on 2D segmented rock images.

- Develop a dimensionless capillary pressure function for mixed-wet conditions based on the simulation results from two-phase semi-analytic approach.
- Compute three-phase capillary entry pressure, capillary pressure curves and fluid configurations for uniformly-wet conditions directly on 2D segmented rock images.
- Model transient behaviour of waterflooding, that is water saturation profiles evolution, directly in uniform- and mixed-wet rock images.
- Compute dynamic capillary pressure curves for imbibition processes in mixed-wet rock images.

Chapter 3

Models Description

This chapter presents a brief description of the models developed as part of this work. First, the general three-phase MS-P equation which was utilized to compute entry pressure for all of piston like displacements in the semi-analytical model, is described.

The semi-analytical model (Frette & Helland, 2010; Helland & Frette, 2010), designed to compute two-phase capillary entry pressures and associated fluid configurations in 2D pore geometries of arbitrary shape, is extended to allow for water invasion into mixed-wet pore spaces and gas invasion into oil and water saturated pore spaces under uniformly-wet conditions. With the extended semi-analytical model, two-phase capillary pressure curves and fluid configurations are simulated directly on segmented 2D rock images both at uniformly- and mixed-wet conditions. Subsequently, three-phase capillary entry radii and associated configuration changes are simulated in single 2D pore geometries extracted from rock images, and finally, three- capillary pressure curves and fluid configurations are simulated directly on 2D rock images at uniform water-wet conditions.

The interacting tube bundle model (Dong et al., 2005; Wang & Dong, 2011) is improved to compute two-phase interface dynamics in mixed-wet realistic pore geometries; subsequently, dynamic capillary pressure curves

and the dynamic coefficient are investigated by defining a proper volume averaged phase pressure.

3.1 MS-P method

In a three-phase fluid system (e.g., gas, oil, water) the capillary pressure between phases satisfies Eq. (1.2). The contact angle between phases i and j, θ_{ij}, is measured through the denser phase j and obeys Young's equation

$$\sigma_{is} - \sigma_{js} = \sigma_{ij} \cos\theta_{ij}. \tag{3.1}$$

From Laplace formula for interfaces in two-dimensional pore spaces, the capillary pressure is expressed as,

$$P_{cij} = \frac{\sigma_{ij}}{r_{ij}}. \tag{3.2}$$

In a gas/oil/water system, elimination of the fluid-solid interfacial tension in Eq. (3.1) results in the Bartell-Osterhof equation (Zhou et al., 1997; van Dijke & Sorbie, 2002a),

$$\sigma_{gw} \cos\theta_{gw} = \sigma_{go} \cos\theta_{go} + \sigma_{ow} \cos\theta_{ow}. \tag{3.3}$$

van Dijke & Sorbie (2002b) proposed linear correlations to describe the relationships between interfacial tensions and wettability in a three-phase system, and estimated the gas-oil and gas-water contact angles, θ_{go} and θ_{gw}, based on the set of interfacial tensions and the oil/water contact angle,

$$\cos\theta_{go} = \frac{1}{2\sigma_{go}}\{C_{S,o} \cos\theta_{ow} + C_{S,o} + 2\sigma_{go}\}, \tag{3.4}$$

$$\cos\theta_{gw} = \frac{1}{2\sigma_{gw}}\{(C_{S,o} + 2\sigma_{ow}) \cos\theta_{ow} + C_{S,o} + 2\sigma_{go}\}. \tag{3.5}$$

In these equations, $C_{S,o}$ is the equilibrium oil spreading coefficient defined as $C_{S,o} = \min(0, \sigma_{gw} - \sigma_{go} - \sigma_{ow})$ (van Dijke et al., 2000). These cor-

relations, Eqs. (3.4) and (3.5), were recently validated using laboratory measurements (Grate et al., 2012).

When three phases are present in a closed system, the external work performed on the system is balanced by the increase of surface free energy of the system:

$$\sum_{i=g,o,w} p_i A_i dx = \sum_{i,j=g,o,w,s\&i\neq j} \sigma_{ij} L_{ij} dx. \tag{3.6}$$

Utilizing the free energy minimization principle, before (subscript b) and after (subscript a) a fluid configurations change (e.g., gas invasion), application of Eq. (3.6) yields:

$$\begin{aligned} &\left\{ -\sum_{i=g,o,w} p_i A_i + \sum_{i,j=g,o,w,s\&i\neq j} \sigma_{ij} L_{ij} \right\}_a dx \\ &= \left\{ -\sum_{i=g,o,w} p_i A_i + \sum_{i,j=g,o,w,s\&i\neq j} \sigma_{ij} L_{ij} \right\}_b dx, \end{aligned} \tag{3.7}$$

where $L_{i,j}$ defines the length of the interfaces (phase-solid and phase-phase). Assuming a rigid solid phase, the total volume of fluid phases and the total length of fluid-solid interfaces remain constant, i.e.,

$$\sum_{i=g,o,w} dV_i = 0 \text{ and } \sum_{i=g,o,w} dA_{is} = 0. \tag{3.8}$$

Combining the Laplace equation, Eq. (3.2), Young's equation, Eq. (3.1), Bartell-Osterhof equation, Eq. (3.3), and Eq. (3.8) into Eq. (3.7), the gas-oil interface curvatures, $1/r_{go}$, is related as follows (van Dijke et al., 2004):

$$\begin{aligned} \frac{\sigma_{go}}{r_{go}}(A_{g,a} - A_{g,b}) &= \sigma_{go}\cos\theta_{go}(L_{gs,a} - L_{gs,b}) + \sigma_{ow}\cos\theta_{ow}(L_{ws,b} - L_{ws,a}) \\ &\quad + \sigma_{go}(L_{go,a} - L_{go,b}) + \sigma_{ow}(L_{ow,a} - L_{ow,b}) \\ &\quad + \sigma_{gw}(L_{gw,a} - L_{gw,b}) - \frac{\sigma_{ow}}{r_{ow}}(A_{w,b} - A_{w,a}). \end{aligned} \tag{3.9}$$

The associated gas-water curvature, $1/r_{gw}$, can be determined from Eqs. (3.2) and (1.2) as:

$$\frac{1}{r_{gw}} = (\frac{\sigma_{go}}{r_{go}} + \frac{\sigma_{ow}}{r_{ow}})\frac{1}{\sigma_{gw}}. \tag{3.10}$$

Eqs. (3.9) and (3.10) are utilized to compute the entry pressure curvature for different types of piston like invasion which will be fully described in Sections 3.3 - 3.5.

3.2 Pore space representation

The semi-analytical model (Frette & Helland, 2010; Helland & Frette, 2010) requires a 2D binary image of the pore as input to calculate capillary pressure curves and fluid configurations in capillaries of arbitrary cross-sections. In this work, individual pores are extracted from high-resolution SEM images of Bentheim sandstone samples. Smooth pore/solid boundaries Γ are calculated by a Euclidean path method (Braquelaire & Vialard, 1999) based on the discrete boundaries that are identified in the binary image.

An example of discrete (black curve) and smoothed (red curve) pore boundary from a pore space extracted from a segmented SEM image of Bentheim sandstone is presented in Figure 3.1(a). Obviously, the pore boundary computed by the Euclidean path method is less angular than the discrete image representation. A closer comparison of the discrete and smooth pore boundary is given in Figure 3.1(b). Orientation angles α are then computed for all boundary points b. An orientation angle α is defined between the boundary tangent at b and a line parallel to the abscissa, see Figure 3.2. The detailed computation of smooth pore boundaries and the orientation angles can be found in Frette & Helland (2010).

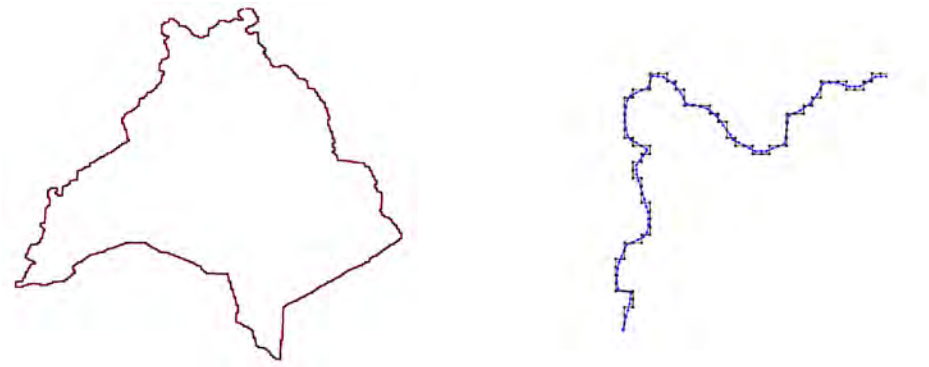

(a) (b)

Figure 3.1: (a) A pore space extracted from Bentheim sandstone as represented by a discrete boundary (black) and corresponding Euclidean path (red); (b) Discrete points (black square) and associated Euclidean points (blue circle) for a pore boundary segment (Frette & Helland, 2010).

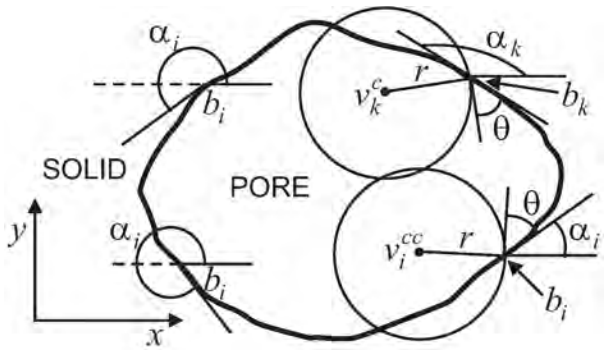

Figure 3.2: Definition of the orientation angle α_i at points b_i. The relation between the counter-clockwise and clockwise closed curves, v^{cc} and v^c, and the parameters r and b are illustrated for a nonzero contact angle θ.

3.3 Two-phase capillary pressure curves and fluid configurations at uniformly-wet conditions

Capillary-controlled fluid displacement for uniformly water-wet conditions is modeled by the process in which oil displaces water, i.e., a drainage process if oil is considered to be the non-wetting phase. For each capillary pressure, the model considers the pore space to be initially fully occupied by water, and the valid oil and water configurations are determined during the required steps in the computational procedure.

3.3.1 Geometrically allowed AMs and regions

For a given oil-water capillary pressure P_{cow}, a circle with radius $r_{ow} = \frac{\sigma_{ow}}{P_{cow}}$ is moved along the pore boundary in opposite (clockwise and counter-clockwise) directions, such that the front arcs form the given contact angle θ_{ow} at the boundary points. The loci of the circle centers constitute two closed curves which are given by (Frette & Helland, 2010):

$$\begin{aligned} v^{cc} &= (x - r_{ij}\sin(\alpha + \theta_{ij}), y + r_{ij}\cos(\alpha + \theta_{ij})), \\ v^{c} &= (x - r_{ij}\sin(\alpha - \theta_{ij}), y + r_{ij}\cos(\alpha - \theta_{ij})); \end{aligned} \tag{3.11}$$

here $ij = ow$, v^{cc} is the counter clockwise curve, v^c is the clockwise curve and (x, y) are the coordinates of the pore boundary point b. Geometrically allowed arc menisci occur at locations where the circles moving in opposite directions intersect, i.e., $v^{cc} = v^c$, and the coinciding arcs point toward pore-space constrictions or corners. Figure 3.3 shows an example calculation of these parameters for a given interface radius and contact angle in a pore extracted from an SEM image of Bentheim sandstone. The precise criteria an AM must satisfy to be geometrically valid were presented in detail by Frette & Helland (2010) and are not repeated here. AM M_i is associated with two contact lines P_i and Q_i that are located in pore/solid boundary points and determined from the v^{cc}- and v^c-curves, respectively. The length of an AM M_i is calculated analytically as cir-

cular arc length and is denoted by $L_{M,i}$. A procedure in which the pore boundary is tracked in counter-clockwise direction (Frette & Helland, 2010) is applied to determine pore/solid segments that are connected to the different AMs. These elements are grouped to form closed boundaries of different regions in the pore space that are classified as bulk regions (BR) or layer regions (LR) based on the orientation of the AMs that belong to the region boundaries (Frette & Helland, 2010). We make use of the following definitions (see also (Frette & Helland, 2010) and paper 6 in the second part of the thesis):

Definition 3.1. *A* pore/solid corner segment*, $S_i \subset \Gamma$, is defined for each AM M_i by a sequence of pore/solid boundary points ordered in counter-clockwise direction from P_i to Q_i, i.e., $S_i = \{P_i = b_k, b_{k+1}, \ldots, b_{l-1}, b_l = Q_i\}$. A corresponding segment which excludes the contact lines is given by $\widehat{S}_i = S_i \setminus \{P_i, Q_i\}$.*

Definition 3.2. *A* pore/solid boundary segment*, $S_{i,j} \subset \Gamma$, is defined by a sequence of pore/solid boundary points ordered in counter-clockwise direction, which connects two adjoining AMs, M_i and M_j, and includes their contact lines as segment endpoints. Its length, $L_{S,i,j}$, is the sum of the distances between all consecutive boundary points. A corresponding segment which excludes the contact lines is denoted by $\widehat{S}_{ij}$.*

Definition 3.3. *Two AMs, M_i and M_j, are* opposite *if $\widehat{S}_i \cup S_j = \Gamma$.*

Definition 3.4. *A* bulk region*, BR, is a region with a closed boundary composed of $n \geq 2$ alternate pore/solid boundary segments and AMs, in which none of the corner segments $\widehat{S}_1 \ldots, \widehat{S}_n$ of AMs $M_i, \ldots, M_n$ have coinciding pore/solid boundary points. The boundary is always a Jordan curve. In the special case $n = 1$, the bulk region has boundary $\{S_{1,1}, M_1\}$, and if $n = 0$ the bulk region is given by the entire pore.*

Definition 3.5. *A* layer region*, LR, is a region with a closed boundary composed of $n \geq 2$ alternate pore/solid boundary segments and AMs. At least two of the AMs are opposite. The boundary is a Jordan curve if and only if the opposite AMs do not intersect.*

Examples of corner and boundary segments, AMs, and the different regions based on Definitions 3.1-3.5 are shown in the example pore in Figure 3.3. In this case, ten geometrically allowed AMs, two BRs and one LR are identified.

Note that region $LR(1)$ with boundary $\{M_4, S_{4,7}, M_7, S_{7,4}\}$ is a layer region because AMs M_4 and M_7 are opposite according to Definition 3.3 and does not satisfy the bulk region conditions (Definition 3.4) because corner segments $\widehat{S}_4$ and $\widehat{S}_7$ (not indicated in the figure) have coinciding pore/solid boundary points. Similarly, $BR(1)$ and $BR(2)$ with boundaries $\{M_1, S_{1,2}, M_2, S_{2,3}, \ldots, M_6, S_{6,1}\}$ and $\{M_7, S_{7,8}, M_8, S_{8,9}, \ldots, M_{10}, S_{10,7}\}$, respectively, are bulk regions according to Definition 3.4 because the corner segments of the AMs, $\left\{\widehat{S}_1, \ldots, \widehat{S}_6\right\}$ and $\left\{\widehat{S}_7, \ldots, \widehat{S}_{10}\right\}$, that belong to the individual region boundaries, do not include coinciding pore/solid boundary points.

3.3.2 Possible fluid configurations change

A valid fluid configuration change is associated with the most favorable entry pressure among all possible oil displacement scenarios. Hence, for a given radius r_{ow}, all possible configurations must be determined. The oil area and total lengths of the pore/solid-fluid boundary segments and AMs must be determined for each configuration candidate, from which the entry radius curvature is calculated from Eq. (3.12).

The valid combinations of regions are (i) individual bulk regions, and (ii) combinations of layer regions that together with neighboring bulk regions form larger merged regions. For each radius r_{ow}, regions that are invaded by oil are organized in a set, which is initially empty. Oil-invaded bulk regions that neighbor a layer region are not included in the merged region combination subjected to oil invasion. This allows for oil invasion into pore-space constrictions that are surrounded by two regions already occupied by oil.

As shown in Figure 3.3, at a given interface radius, the three identified

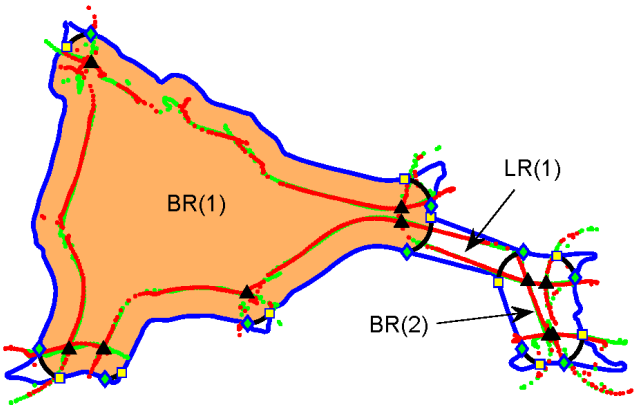

(a)

(b)

Figure 3.3: Numerical example of the procedure to determine oil/water configuration at a given interface radius r_{ow} with a contact angle equal to $\theta_{ow} = 20°$. The pore/solid boundary (blue solid curve), arc menisci (black solid curves), contact lines P (blue diamonds) and Q (yellow squares) that are associated with the counter-clockwise and clockwise circle-center curves, v_{ow}^{cc} (red dotted curve) and v_{ow}^{c} (green dotted curve), respectively, and circle-center intersections (black triangles) are shown. Panel (a) indicates the different layer and bulk regions and highlights the region invaded by oil (colored area). Panel (b) elucidates the different AMs M_i, pore/solid boundary segments $S_{i,j}$ and some of the corner segments S_i.

regions are $BR(1)$, $LR(1)$ and $BR(2)$. Initially, none of the identified regions are occupied by oil, therefore the allowed combinations of regions are given as two individual bulk regions $\{BR(1)\}$ and $\{BR(2)\}$, and the combination of the layer regions $\{BR(1), LR(1), BR(2)\}$.

3.3.3 Procedure for determining the fluid configurations

Entry pressure curvatures are computed for all valid BR and LR combinations not yet occupied by the invading fluid. The general MS-P equation, Eq. (3.9), for possible fluid configurations changes at uniformly-wet, two-phase condition yields:

$$F_i(r_{ow}) = \left(\frac{1}{r_{ow}}\right)_i = \frac{L_{os,i}\cos\theta_{ow} + L^E_{ow,i} - L^F_{ow,i}}{A_{o,i}}, i = 1, 2, 3...N_c, \tag{3.12}$$

where F denotes entry curvature, $L^E_{ow,i}$ and $L^F_{ow,i}$ are the lengths of the AMs that form and vanish during the displacement, respectively, and N_c represents the number of possible fluid configurations changes. The solid length contacted by the invading fluid is denoted by $L_{os,i}$, and $A_{o,i}$ is the invaded cross-sectional area. The fluid configuration at a given capillary pressure is determined by an iterative procedure where, in each iteration step, the most favorable entry pressure among all available displacement scenarios is computed from:

$$F^*(r_{ow}) = \min\{F_i(r_{ow}) : 1/r_{ow} > F_i(r_{ow}), i = 1, 2, 3..., N_c\}, \tag{3.13}$$

and the corresponding combination of regions is invaded by oil. The iterations are terminated when $F^*(r_{ow})$ cannot be determined. At this stage the fluid configuration as well as phase saturation at the given capillary pressure are obtained.

Figure 3.3 shows an example of the iterative procedure. As mentioned above, at the given interface radius, three regions $BR(1)$, $LR(1)$ and $BR(2)$ are identified. Initially, the pore space is water-filled, and therefore the allowed combinations of regions in the first iteration are $\{BR(1)\}$,

$\{BR(2)\}$ and $\{BR(1),\ LR(1),\ BR(2)\}$. According to Eqs. (3.12) and (3.13), it is demonstrated that the most favorable entry pressure $F^*(r_{ow})$ corresponds to the individual region {BR1}. Thus, this region is invaded by oil, and the fluid configuration is updated. In the second iteration step, the combinations of regions $\{BR(2)\}$ and $\{LR(1),\ BR(2)\}$ are generated. However, since it turns out that none of these combinations of regions satisfy Eq. (3.13), these regions remain occupied by water and the algorithm proceeds with the next capillary pressure.

The phase saturations for a given capillary pressure are obtained by summing up individual fluid occupation in each individual pore space for the whole rock image. The entire capillary pressure curve is obtained by increasing the capillary pressure stepwise value to a maximum capillary pressure, which in each step the procedure presented in Section 3.3.1 - 3.3.3.

3.4 Two-phase capillary pressure curves and fluid configurations at mixed-wet conditions

The procedure employed to compute capillary pressure curves and corresponding fluid configurations for mixed-wet conditions is described in this section. First, the wettability is characterized for mixed-wet realistic pore geometries; and then the procedure for computing fluid configuration at a determined capillary pressure in the represented mixed-wet pore space is briefly introduced.

3.4.1 Wettability Characterization

Establishment of mixed wettability

In this work, mixed-wet conditions are generated according to the hypothesis described in Kovscek et al. (1993); the model is run for uniform wetting conditions as described in Section 3.3 to an arbitrary interfacial

radius r_{pd}, which represents the end of primary drainage and establishes an initial water saturation for imbibition.

At the end of primary drainage, we assume that the thin water film between pore-wall areas and the bulk oil phase collapse simultaneously and thus the pore surface is exposed to oil, which consequently results in wettability alteration. The pore boundary is organized in segments $\{T_j\}_{j=1}^{N_s}$ that are associated with uniform contact angles $\{\theta_j\}_{j=1}^{N_s}$. The segments T_j are assumed to connect adjoining contact lines of the AMs occurring at the end of primary drainage. If a segment T_j is in contact with oil, $\theta_j = \theta_c$ where θ_c denotes Cassie contact angle as defined in Eq. (3.14) below, and if T_j is in contact with water, $\theta_j = \theta_w$, which θ_w is the contact angle used in primary drainage. The endpoint of each segment equals the starting point of the next segment, i.e., $T_j \cap T_{j+1} = H_j$, where H_j are pinning points on the pore boundary where AMs may hinge during imbibition. Note that, while the procedure is general enough to allow assigning a different contact angle θ_j to each segment T_j, we limit this study to cases in which only one contact angle θ_c is defined on all oil/solid segments, and another contact angle θ_w is defined on all water/solid segments.

An example of a mixed-wet pore space is given in Figure 3.4; there are three oil-wet segments (T_2, T_4, T_6) and three water-wet segments segments (T_1, T_3, T_5) which are separated by the AMs and six pinning points $(H_1, H_2, H_3, H_4, H_5, H_6)$.

Cassie contact angle

In order to account for mixed-wet conditions, where different pores have different wetting properties, we first assign a constant contact angle θ_o to all the segments in contact with oil. Subsequently, a new contact angle is calculated in each pore using the expression:

$$\cos\theta_c = \frac{L_w \cos\theta_w + L_o \cos\theta_o}{L}, \tag{3.14}$$

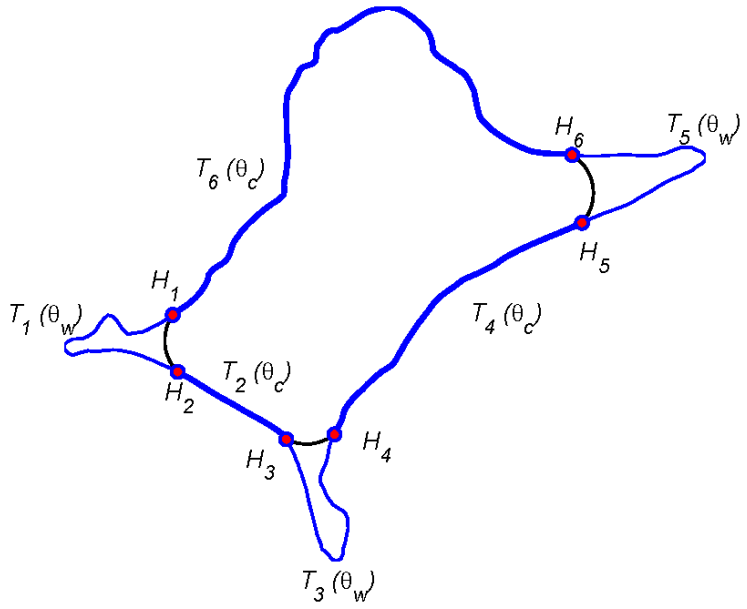

Figure 3.4: Mixed-wet pore space wettability characterization, oil-wet pore boundary segments $T_j(\theta_c)$ (bold blue lines), water-wet pore boundary segments $T_j(\theta_w)$ (thin blue lines), pinning points H_j, and relevant AMs (black solid curves).

where L_w and L_o are the sum of all segment lengths in an individual pore space that are contacted by water and oil, respectively, at the end of primary drainage, and $L = L_w + L_o$ is the pore perimeter. Hence, the pore-boundary segments in contact with oil are described by the contact angle θ_c, which varies from pore to pore, whereas the pore-boundary segments in the corners and constrictions are still occupied by water, thus remaining water-wet and described by the contact angle θ_w. Thus, arc menisci may become pinned at lines separating surfaces of different wettability during the subsequent imbibition process. The contact angle expressed by Eq. (3.14) is referred to in the literature as Cassie's contact angle (Cassie & Baxter, 1944), and has been employed previously to describe surfaces with heterogeneous wettability (Long et al., 2005).

The proposed method for determining contact angles θ_c that are specified on the oil-wet segments results in θ_c that varies from pore to pore. Eq. (3.14) also implies that the contact angles θ_c become larger as the initial water saturation is reduced because L_o increases at the expense of a decreasing L_w. Such a behavior is in agreement with the work of Frette et al. (2009) who calculated the pore-wall area with intact and collapsed water films during primary drainage based on disjoining pressure and pore-wall curvature. With the redefined Cassie contact angle, pore spaces could be oil-wet, intermediate-wet or water-wet. Porous rocks that remain water-wet after primary drainage are modeled by assigning a contact angle $\theta_o < 90°$, like $\theta_o = 70°$, on the segments in contact with oil.

3.4.2 Circle-center curves at mixed-wet conditions

For mixed-wet conditions, fluid invasion may occur at both $P_{c,ow} > 0$ and $P_{c,ow} < 0$, as opposed to the uniform water-wet case where always $P_{c,ow} > 0$. In the model, we consider the process where oil displaces water for $P_{c,ow} > 0$ and the process at which water displaces oil for $P_{c,ow} < 0$. To facilitate calculations for both cases, we introduce the parameters $\bar{r}_{ow}$

and $\bar{\theta}_\gamma, \gamma = c, w$, which are defined as

$$\bar{r}_{ow} = \begin{cases} r_{ow} & \text{if } r_{ow} > 0, \\ -r_{ow} & \text{if } r_{ow} < 0; \end{cases} \quad \bar{\theta}_\gamma = \begin{cases} \theta_\gamma & \text{if } r_{ow} > 0, \\ \pi - \theta_\gamma & \text{if } r_{ow} < 0. \end{cases} \tag{3.15}$$

The procedure described in Section 3.3.1 is followed and for a given capillary pressure, $P_{c,ow} = \frac{\sigma_{ow}}{r_{ow}}$, a circle with radius $\bar{r}_{ow}$ is moved in the two opposite (clockwise and counter-clockwise) directions along the pore boundary such that the angle $\bar{\theta}_\gamma$ is defined at the front arcs in all boundary points in both cases. The loci of circle centers constitute two closed curves which are given by an equation similar to Eq. (3.11):

$$\begin{aligned} v^{cc} &= (x - \bar{r}_{ow}\sin(\alpha + \bar{\theta}), y + \bar{r}_{ow}\cos(\alpha + \bar{\theta})), \\ v^{c} &= (x - \bar{r}_{ow}\sin(\alpha - \bar{\theta}), y + \bar{r}_{ow}\cos(\alpha - \bar{\theta})), \end{aligned} \tag{3.16}$$

where $\bar{\theta} = \bar{\theta}_c$ or $\bar{\theta} = \bar{\theta}_w$. However, if the circle is moving from a surface described by $\bar{\theta}_\alpha$ to a surface described by $\bar{\theta}_\beta$, the separating boundary point $b(x, y)$ is considered to be constant while a sequence of equally spaced values $\theta_i = \bar{\theta}_\alpha + \frac{(\bar{\theta}_\beta - \bar{\theta}_\alpha)}{m} i, i = 0, 1, \cdots, m$ (m is the number of contact angles in this sequence, and $m = 50$ is considered in this work) replace $\bar{\theta}_\alpha$. Thus, the circle is pinned in $b(x, y)$ while it rotates from angle $\bar{\theta}_\alpha$ until angle $\bar{\theta}_\beta$ is reached, at which instance it enters the obtained surface and continues the movement to the next boundary points at the constant contact angle $\bar{\theta}_\beta$. This feature accounts for situations where contact lines become pinned and the corresponding arc meniscus hinges at an angle which changes according to capillary pressure (Ma et al., 1996).

Figure 3.5 shows a numerical example of the v^{cc} and v^c curves computed in an extracted Bentheim sandstone pore space at mixed-wet conditions assuming $\theta_c = \theta_o$. Figure 3.5(a) shows that for positive capillary pressures and $\theta_c > 90°$, v^{cc} and v^c data corresponding to oil-wet pore-boundary segments are located on the pore exterior. This is reasonable because all

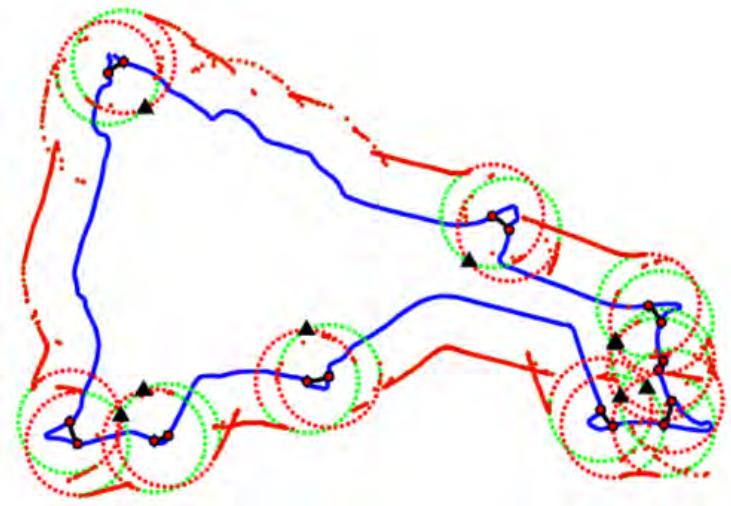

(a) $\theta_w = 0°, \theta_o = 180°$ and $P_c > 0$

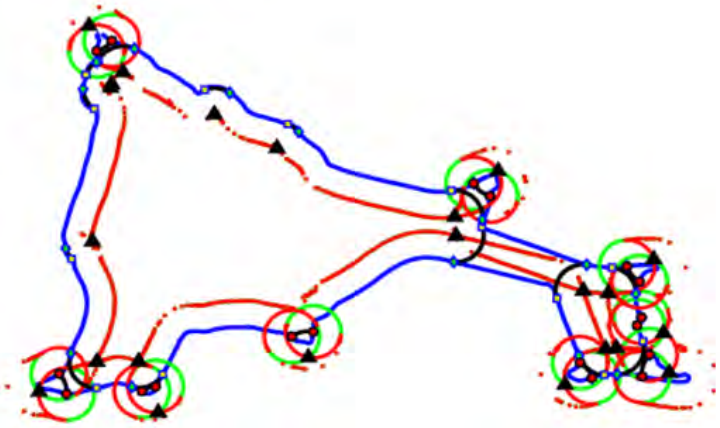

(b) $\theta_w = 0°, \theta_o = 180°$ and $P_c < 0$

Figure 3.5: Numerical examples of the semi-analytical algorithm employed in an extracted pore space from Bentheim sandstone at mixed-wet conditions. The relation between $b \in \Gamma$ (blue solid curve), v^{cc} (red dotted curve), v^c (green dotted curve), circle intersections (black triangles) and AMs (black solid curves) is illustrated. Pinned contact lines (red circles) that are located in points separating solid surfaces with different wettability are distinguished from contact lines that are located on uniform oil-wet surfaces (yellow squares, green diamonds).

AMs are expected to be pinned at this condition.

3.4.3 Geometrically allowed AMs and regions

The locations of the geometrically allowed arc menisci are determined from Eq. (3.16) as the intersections of the circle centers, i.e., v^{cc}=v^c. An example of geometrically allowed AMs in a pore space from Bentheim sandstone at mixed-wet conditions both for $P_{c,ow} < 0$ and $P_{c,ow} > 0$ is shown in Figure 3.5.

Figure 3.5(a) shows that for positive capillary pressures and $\theta_c > 90°$, all AMs are located on the same contact lines as in the end of primary drainage. Obviously, these pinned interfaces curves int the opposite direction for $P_{cow} < 0$, as shown in Figure 3.5(b).

Based on the identified set of interfaces at mixed-wet conditions, regions with boundaries composed of alternate AMs and pore boundary segments are determined and subsequently classified as corner phase regions (CR), bulk phase regions (BR), or layer phase regions (LR) from the following definitions (Helland & Frette, 2010):

Definition 3.6. *A* Corner Region*, CR, is a geometrical region defined for $P_c < 0$ with a boundary composed of segments $T_j(\theta_w)$ only and pinned AMs, of which none of these AMs are opposite.*

Definition 3.7. *A* Bulk region*, BR, is a geometrical region defined for both $P_c > 0$ and $P_c < 0$ with a boundary composed of segments $S_{i,j}$ and AMs. Opposite AMs can only exist for $P_c < 0$, which must hinge and also belong to a CR boundary.*

Definition 3.8. *A* layer region*, LR, is a geometrical region defined for both $P_c > 0$ and $P_c < 0$ composed of segments $S_{i,j}$ and at least two opposite AMs, of which at least one is not pinned and located on uniformly-wet segments.*

Examples of these three types of regions defined at mixed-wet conditions are given in Figure 3.6. As shown in this figure, CRs describe the

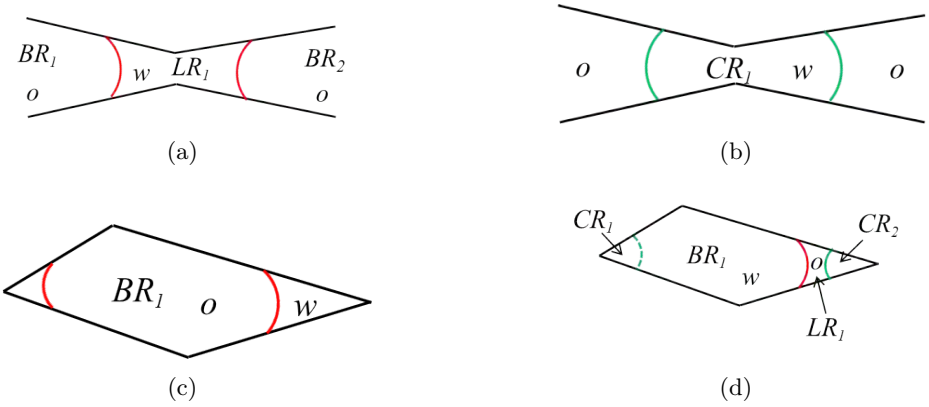

Figure 3.6: Illustration of region classification and possible phase occupancies in idealized pore geometries. Hinging AMs occurring at mixed-wet conditions (solid green curves) and AMs located on uniformly-wet surfaces (red solid curves) are shown. (a) Example of opposite AMs and the occurrence of an LR region at water-wet conditions; (b) example of hinging AMs pointing away from each other at negative capillary pressure and a CR region filled with residing water after drainage; (c) example of a BR region at water-wet conditions; and (d) example of BR, CR and LR regions during imbibition at negative capillary pressure for mixed-wet conditions. In panel (d) the boundaries of regions CR_1 and BR_1 include a common hinging AM (green dashed curve) which disappears when water invades region BR_1.

water-wet corners, Figure 3.6(d), and constrictions, Figures 3.6(b), that remain occupied with water after primary drainage. Examples of BRs are shown in Figure 3.6(c) and 3.6(d), and examples of LRs are shown in Figures 3.6(b) and 3.6(d).

3.4.4 Entry pressure

All allowed combinations of layer and bulk phase regions, BRs and LRs, that have not yet become occupied by the invading fluid are generated, and the associated entry pressure curvatures are calculated for each combination of regions i by generalizing the MS-P equation, Eq. (3.9), for

two-phase mixed-wet conditions as follows:

$$F_i(r_{ow}) = \begin{cases} \frac{L_{os,i}\cos\theta_c + L^E_{ow,i} - L^F_{ow,i}}{A_{o,i}}, & \text{if } r > 0 \\ \frac{L_{os,i}\cos\theta_c - L^E_{ow,i} + L^F_{ow,i}}{A_{o,i}}, & \text{if } r < 0. \end{cases} \tag{3.17}$$

Here, $L^E_{ow,i}$ and $L^F_{ow,i}$ are the lengths of the AMs that form and vanish, respectively, when oil displaces water for $P_c > 0$ or water displaces oil for $P_c < 0$. Furthermore, $L_{os,i}$ represents the length of all boundary segments the invading fluid contacts, and $A_{o,i}$ is the invaded cross-sectional area.

3.4.5 Procedure for determining fluid configurations

The fluid configurations at a given capillary pressure are determined by an iterative procedure. Initially, the pore space is occupied by water if $P_c > 0$, while for $P_c < 0$ the initial fluid configuration is given from the end of the primary drainage process, in which the invading water is always present in the corner regions CRs and the remaining pore areas are occupied by oil. At each iteration step, the most favorable entry pressure among all available displacement scenarios, N_c, is determined by

$$F^*(r_{ow}) = \begin{cases} \min\{F_i(r_{ow}) : 1/r_{ow} \geq F_i(r_{ow}), i = 1, 2, 3..., N_c\}, & \text{if } r_{ow} > 0 \\ \max\{F_i(r_{ow}) : 1/r_{ow} \leq F_i(r_{ow}), i = 1, 2, 3..., N_c\}, & \text{if } r_{ow} < 0 \end{cases} \tag{3.18}$$

and the corresponding regions become occupied by the invading fluid. At the next iteration step, new combinations of regions are generated based on the updated fluid configurations and the corresponding entry pressure curvatures are calculated from Eq. (3.17). The most favorable entry curvature is determined by Eq. (3.18) and the corresponding combination of regions is invaded. Thus, the valid fluid configuration is determined by filling favorable region combinations with the invading fluid consecutive in iteration steps. The iterations are terminated when $F^*(r_{ow})$ cannot be determined, that is when all regions have been invaded or when none of

the remaining combinations of regions satisfy Eq. (3.18). At this stage the algorithm proceeds with the next capillary pressure.

The phase saturations, for a determined capillary pressure, are obtained by summing up fluids occupation in each individual pore space for the whole rock image and the entire capillary pressure curve is obtained by decreasing the capillary pressure from its maximum value at the end of drainage to its minimum value at the end of the forced imbibition.

3.5 Three-phase capillary pressure curves and fluid configurations

For the three-phase case, gas is assumed to invade the porous space at uniform water-wet conditions, which implies that gas is the non-wetting phase, oil is the intermediate-wetting phase and water is the wetting phase (Hui & Blunt, 2000; van Dijke & Sorbie, 2002b). The procedure to compute three-phase capillary pressure curves and corresponding fluid configurations in the extracted pore spaces for each prescribed gas-oil capillary pressure can be summarized as follows: First, closed circle-center curves are generated for all three fluid pairs to compute all geometrically permissible gas-oil, gas-water and oil-water interfaces; second, all geometrically permissible combinations of the three sets of interfaces are determined based on the assumed wetting order, and the corresponding entry pressures for these interface combinations are calculated based on Eq. (3.9); and third, the valid fluid configurations at the prescribed gas-oil capillary pressure is determined iteratively by executing at each step the displacement with the smallest gas-oil capillary entry pressure being smaller than the gas-oil capillary pressure among the allowed interface combinations. When no further configuration changes satisfy the invasion criterion, the three-phase configuration is determined and the algorithm proceeds with the next prescribed gas-oil capillary pressure.

3.5.1 Geometrically allowed AMs

For a set of three-phase capillary pressures ($P_{cow}, P_{cgo}, P_{cgw}$) and contact angles ($\theta_{ow}, \theta_{go}, \theta_{gw}$), the fluid configurations for a specific oil-water capillary pressure, P_{cow}, is determined as described in the previous section. Prior to gas invasion, the pore space could be occupied by either a single phase (oil or water) or with oil located in the center of the pore spaces while the water is distributed in the corners and necks. The closed circle-center curves are generated for all three fluid pairs, by viewing the gas-oil, gas-water and oil-water systems separately and by applying Eq. (3.11) three times with $r_{ij} = \frac{\sigma_{ij}}{P_{cij}}, ij = go, ow, gw$. This results in three different sets of circle intersections which yield the centers of all possible gas-oil, oil-water and gas-water AMs. An example for geometrically allowed gas-oil and gas-water AMs in a single sandstone pore space is shown in Figure 3.7 with $r_{ow} = 8$ pixel lengths, $r_{go} = 12$ pixel lengths, $r_{gw} = 9$ pixel lengths, and $\theta_{ow} = \theta_{go} = \theta_{gw} = 0°$. Only gas-water AMs (green curves) and gas-oil AMs (red curves) are shown in Figure 3.7 to demonstrate the formation of possible gas invasion candidates; and the geometrically allowed oil-water AMs for this example are shown in Figure 3.8 as blue curves.

3.5.2 Possible fluid configurations changes

All possible fluid configurations for gas invasion are computed by combining the geometrically allowed three-phase AMs systematically in different ways. First, possible gas configurations are constructed by identifying individual gas regions, as well as combinations of them, based on the determined gas/oil and gas/water AMs without honoring the existing oil/water configuration in the pore. Second, for each bulk gas configuration, all possible combinations of bulk oil regions are determined. The third step is to identify all geometrically possible oil layers that can be located between bulk gas and corner water, and then add combinations of such oil layers to each of the determined bulk gas and oil configuration

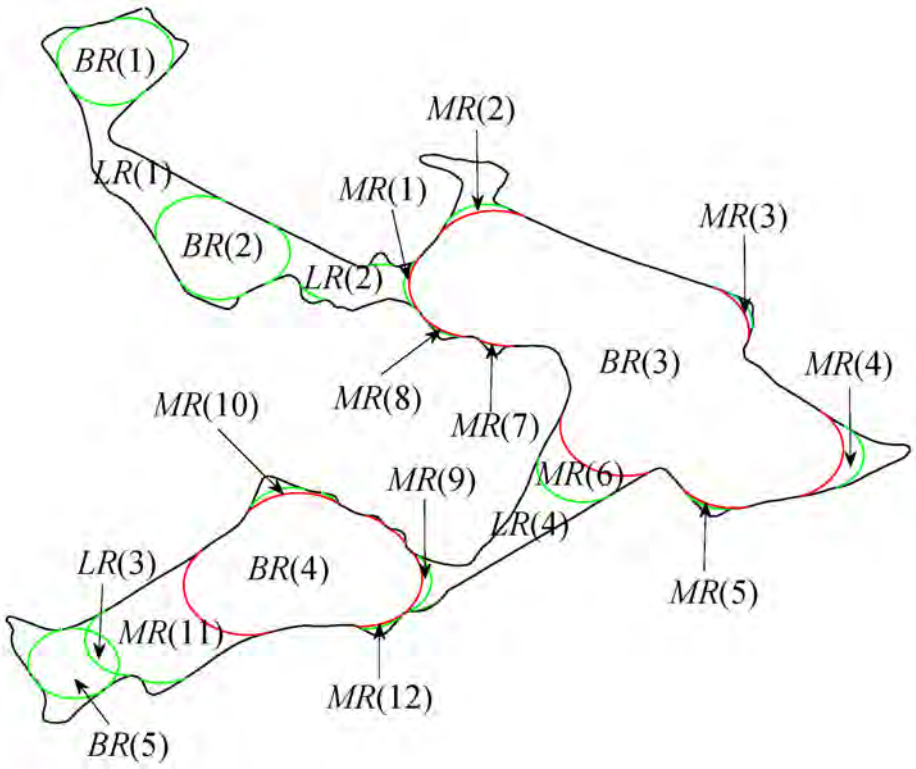

Figure 3.7: Numerical example illustrating the gas-oil and gas-water AMs (black: pore boundary; red: gas-oil; green: gas-water) and the extracted regions in a Bentheim sandstone pore ($r_{go} = 12$ pixel lengths, $r_{go} = 12$ pixel lengths, $r_{gw} = 9$ pixel lengths and $\theta_{ow} = \theta_{go} = \theta_{gw} = 0°$).

candidates. The sum of all these combinations constitutes the number of all possible three-phase configurations in the pore space at a prescribed set of three-phase capillary pressures.

Possible gas configurations

According to the wetting order of the three phases, the bulk gas configuration can only be formed by gas-oil and gas-water AMs, and the pore-boundary tracking procedure (Frette & Helland, 2010) is utilized to identify the various gas regions with boundaries composed of alternate AMs and pore-boundary segments. These determined regions are subsequently classified as bulk phase regions (BR; see Definition 3.4), layer phase regions (LR; see Definition 3.5) or mixed phase regions (MR) according to the following definition (see also Figure 3.7):

Definition 3.9. *A* mixed region*, MR, is a region with closed boundary composed of $n \geq 2$ alternate pore/solid boundary segments and AMs, of which none of the AMs are opposite. Further, the boundary consists of at least one gas/oil AM M_i and one gas/water AM M_j, for which the pore/solid corner segments either satisfy $S_i \subset S_j$ or $S_j \subset S_i$. The boundary of the region is a Jordan curve if and only if these AMs do not intersect.*

All possible gas configuration candidates are determined by combining the extracted regions in all possible ways, which are archived by first considering the individual BR regions and also generating the BR and LR region combinations as described previously in Section 3.3.2 for two-phase systems at uniformly-wet conditions; secondly, for each determined gas region candidate in the fist step, new gas invasion candidates can be formed by adding the combinations of all surrounding MRs to the determined gas candidate.

A numerical example of one gas configuration candidate is shown in Figure 3.8. The possible gas configuration (yellow area) is determined

from bulk region $BR(3)$ which is that is shown in Figure 3.7. There are eight MRs ($MR(1), MR(2), MR(3), MR(4), MR(5), MR(6), MR(7)$ and $MR(8)$) that are neighbors to $BR(3)$ (see Figure 3.7), and therefore $2^8 - 1 = 255$ different possible gas configurations could be formed for the determined gas candidate (yellow area in Figure 3.8) based on all combinations of the eight MRs.

Possible oil configurations

According to the wetting conditions, oil may exist as bulk regions which are surrounded by corner or/and sandwiched water, and as layers existing between center gas and corner/neck water. For a determined gas configuration candidate, the associated oil configurations are determined by adding the oil-water interfaces in all permissible ways. Independent bulk oil regions, and connected independent bulk oil regions are defined as BR and $LR - BR$ region combinations that are generated with the oil-water system and located completing outside of the considered gas configuration candidate. These regions are determined in the first step, and then the bulk oil configurations are obtained by combining them in all possible ways.

An example of one determined gas configuration candidate (yellow area) and all geometrically allowed oil-water interfaces (blue curves) are presented in Figure 3.8. This figure shows three BRs ($BR(1), BR(2), BR(4)$; $BR(3)$ is not considered because it is covered by the gas candidate (yellow area)) that are extracted from oil-water AMs. The possible bulk oil configurations can be determined by considering all combinations of these three BRs and LRs located in between.

The last step for a possible three-phase configuration is to quantify the oil layers between gas and water (both in the corner and neck) for each determined bulk gas and bulk oil configuration. For example, as shown in Figure 3.8, if the gas region (yellow area) and one bulk oil region ($BR(4)$) are considered as the bulk gas and bulk oil configurations, eight oil layers

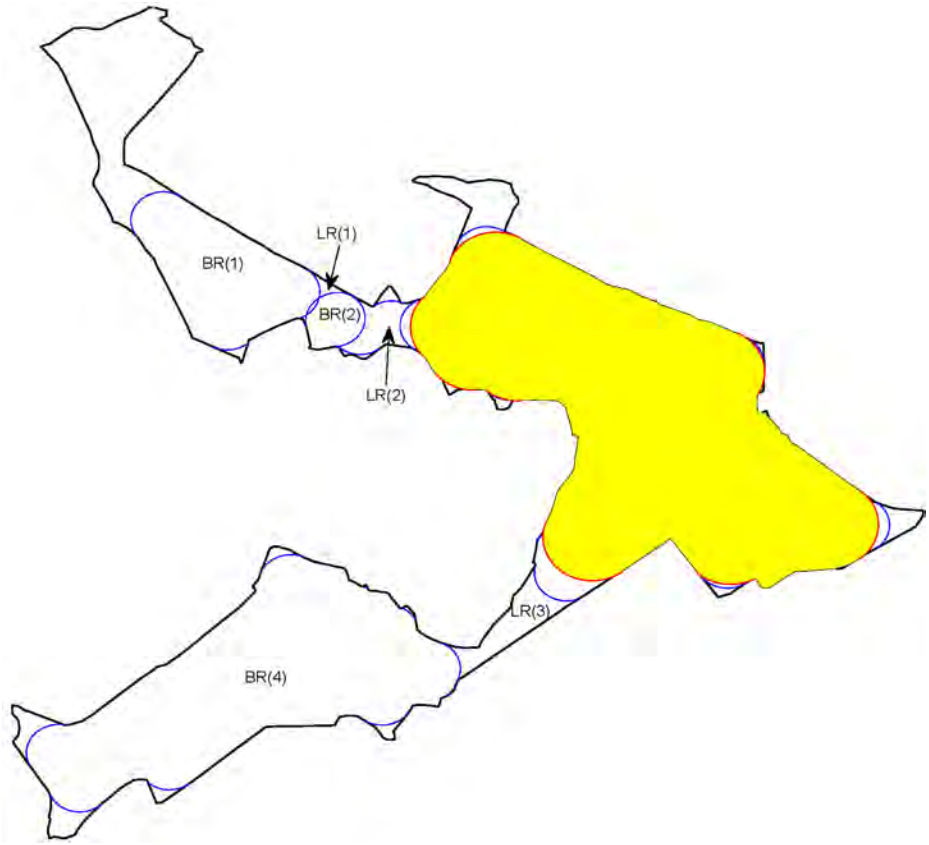

Figure 3.8: Numerical example illustrating one possible gas configuration and its possible oil-water AMs (black curve: pore boundary; blue curves: oil-water AMs; red curves: gas-oil AMs; yellow area: gas occupy) for gas invasion in a Bentheim sandstone pore, ($r_{ow} = 8$, pixel lengths $r_{go} = 12$ pixel lengths and $r_{gw} = 9$ pixel lengths and $\theta_{ow} = \theta_{go} = \theta_{gw} = 0^{\circ}$).

(formed by gas-oil and oil-water AMs) which exist between gas and water.

3.5.3 Capillary entry curvatures for all possible configuration changes

For each determined fluid configuration candidate resulting from gas invasion into the existing oil/water configuration in the pore space, the gas/oil capillary entry curvature is computed based on Eq. (3.9). The required parameters before and after displacement is calculated as follows in the configurations: AM lengths are calculated analytically as circular arc lengths; pore/solid boundary-segment lengths are calculated by adding the Euclidean distances between consecutive points included in the segment; and areas of oil, water and gas are computed based on the boundary points of the fluid regions formed by the alternate AM and pore/solid segments (Frette & Helland, 2010). For the gas/oil entry curvature computations, Eq. (3.9) is rearranged as follows:

$$\begin{aligned} F_{go,j} = \{ & \sigma_{go}\cos\theta_{go}(L_{gs,a} - L_{gs,b}) \\ & + \sigma_{ow}\cos\theta_{ow}(L_{ws,b} - L_{ws,a}) + \sigma_{ow}(L_{ow,a} - L_{ow,b}) \\ & + \sigma_{go}(L_{go,a} - L_{go,b}) + \sigma_{gw}(L_{gw,a} - L_{gw,b}) \\ & - \frac{\sigma_{ow}}{r_{ow}}(A_{w,b} - A_{w,a}) \Big\}_j / \{\sigma_{go}(A_{g,a} - A_{g,b})\}_j , \end{aligned} \tag{3.19}$$

where $F_{go,j}, j = 1, \ldots, N_c$, are gas/oil entry curvatures and N_c represents the number of possible configuration changes by which gas can enter the pore for the specific set of interface radii.

The gas-oil entry radius for gas invasion into an oil- and water-saturated pore is calculated iteratively:

$$\frac{1}{r_{go,m+1}} = \min\{F_{go,j}(r_{go,m}), j = 1, 2, 3..., N_c\}, \tag{3.20}$$

where m denotes the iteration level. For a given r_{ow}, the initial radii used

in the first iteration (m=1), $r_{go,1}$ and $r_{gw,1}$, are given by:

$$r_{gw,1} = \begin{cases} r_{ow,E}, \\ \frac{\sigma_{gw}}{\sigma_{go}/r_{go,1}+\sigma_{ow}/r_{ow}}; \end{cases} \quad r_{go,1} = \begin{cases} \frac{\sigma_{go}}{\sigma_{gw}/r_{gw,1}-\sigma_{ow}/r_{ow}} & \text{if } r_{ow} > r_{ow,E}, \\ r_{ow,E} & \text{if } r_{ow} \leq r_{ow,E}; \end{cases} \tag{3.21}$$

where $r_{ow,E}$ is the capillary entry radius for oil invasion into a water filled pore space.

3.5.4 Procedure for determining three-phase fluid configurations

The fluid configurations for a given set of three-phase capillary pressures are determined by an iterative procedure where, in each iteration step, the most favorable entry pressure among all available displacement scenarios N_c is determined by

$$F^*(r_{go}) = \min\{F_i(r_{go}) : \frac{1}{r_{go}} \geq F_i(r_{go}), i = 1, ...N_c\}, \tag{3.22}$$

and the corresponding regions in the combination are invaded by gas. All allowed combinations of regions, which are not yet occupied by the invading gas, are generated, and the associated entry pressure curvatures are calculated for each of these region combinations i by the three-phase MS-P equation (Eq. (3.19)). The iterations are terminated when $F^*(r_{go})$ cannot be determined, and the algorithm proceeds to the next gas-oil capillary pressure.

An example of this iterative procedure is described below to illustrate the computation of the three-phase fluid configuration for a given set of capillary pressure radii and contact angles in a strongly water-wet Bentheim sandstone pore space with spreading oil. The capillary radii are r_{go} = 12 pixel lengths, r_{ow} = 8 pixel lengths and r_{gw} = 9 pixel lengths, the interfacial tensions are equal to σ_{go} = 0.01 N/m, σ_{ow} = 0.02 N/m and σ_{gw} = 0.03 N/m, and the contact angles are $\theta_{ow} = \theta_{go} = \theta_{gw} = 0°$. The initial oil-water configuration before gas invasion is computed by an

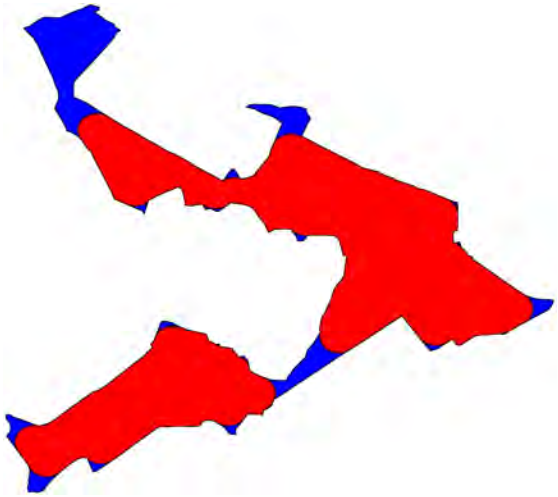

Figure 3.9: Initial fluid configuration before gas invasion in an individual Bentheim sandstone pore space; red: oil; blue: water ($r_{ow} = 8$ pixel lengths, $\theta_{ow} = 0°$).

iterative procedure as described in Section 3.3 and the resulting initial oil-water configuration before gas invasion is shown in Figure 3.9.

All geometrically allowed gas-oil and gas-water interfaces and extracted BR, LR, MR used to determine all possible gas invasion candidates are shown in Figure 3.7. One of the possible gas invasion candidates and its possible oil-water AMs are presented in Figure 3.8. Among all the possible interface combinations, the most favorable fluid configuration change is estimated by Eq. (3.22); in this case $F^*(r_{go}) = 0.0624$ (pixel lengths)$^{-1}$ and its associated three phase configuration is shown in Figure 3.10(a). For the determined fluid configuration shown in Figure 3.10(a), 28 possible BR gas invasion candidates could be determined by the four non-invaded BRs ($BR(1)$, $BR(2)$, $BR(4)$, $BR(5)$) and their associated MRs; eight different oil layer displacements examined based on the eight oil layers between the invaded gas region and remaining water; Two more $BR-LR$ combinations could be determined since both of the two LRs are connected by mixed regions with the invaded gas region. In the present

step, $F^*(r_{go}) = 0.0628$ (pixel lengths)$^{-1}$ and its associated three-phase fluid configuration is shown in Figure 3.10(b). In the third iteration step, no fluid configuration candidate satisfies Eq. (3.22), and the iterations are terminated with the algorithm proceeding to the next prescribed gas-oil capillary pressure.

3.6 Interacting tube bundle model

In this section, the interacting tube bundle model, which was introduced by Dong et al. (2005), is extended to simulate waterflooding in a pore space that is represented by a bundle of tubes whose cross-sections are extracted from a 2D thin-section rock image. The interacting tube bundle model for simulating the transient interface displacements enables the computation of water saturation as a function of time and the oil-water interface position along the tube length direction. The input parameters, namely capillary pressure and conductance, are computed with the semi-analytical model which has been presented in Sections 3.3 and 3.4. Based on the interface positions simulated with interacting tube bundle model, volume-averaged phase pressures are introduced to calculate the dynamic capillary pressure; the dynamic capillary coefficients, τ, are obtained by fitting the time derivative of water saturation and the difference between the dynamic and static capillary pressures by a linear correlation.

3.6.1 Interacting tube bundle model description

In the interacting tube bundle model the number of front menisci and capillary pressure curve data are equal. For $k = 1, 2, \ldots, N$ front menisci with capillary pressures $P_{c,k}$, the tube bundle is divided along its length into $N+1$ regions, with each region k having constant total cross-sectional fluid areas, $A_{o,k}$ and $A_{w,k}$, and fluid conductances, $g_{o,k}$ and $g_{w,k}$. Figure 3.11 shows a schematic diagram illustrating the front menisci positions measured from the inlet water reservoir. A realistic cross-sectional

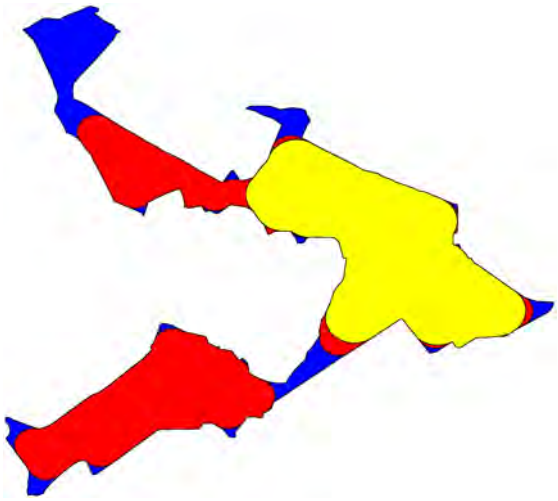

(a) First iteration step, $F^*(r_{go}) = 0.0624$ (pixel lengths)$^{-1}$

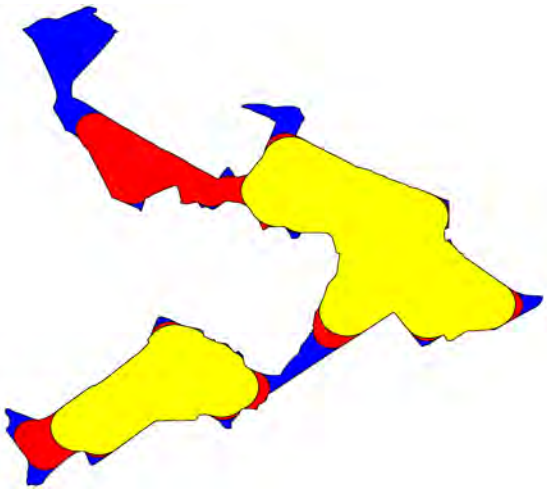

(b) Second iteration step, $F^*(r_{go}) = 0.0628$ (pixel lengths)$^{-1}$

Figure 3.10: Numerical example illustrating the three-phase fluid configuration for gas invasion (yellow area: gas, red area: oil and blue area: water) in a Bentheim sandstone pore.

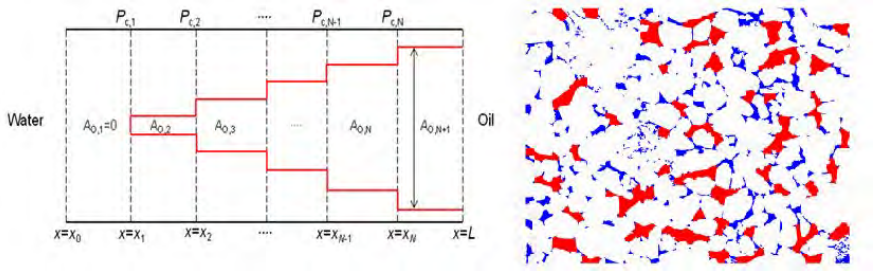

Figure 3.11: Schematic diagram of the interface positions along a tube bundle (left), and cross-sectional fluid configurations (blue colour represents the water phase and red the oil phase) in a length region as computed by the semi-analytical model (right).

fluid configuration in one of the regions is shown in the right panel of Figure 3.11, as computed by the semi-analytical model (Section 3.3). Note that the different front menisci separating the length regions could represent interfaces that are located in a single irregular pore geometry. It is also possible that the front menisci represent interfaces that are located in different pores or represent discrete approximations of the gradual change of interface positions in the pore corners behind the front.

A sketch of the phase pressure profiles along the tube bundle is illustrated in Figure 3.12. Hence, the pressure difference between the inlet water reservoir and outlet oil reservoir, $\Delta P = P_{w,res} - P_{o,res}$, can be expressed in terms of the capillary pressure across each front meniscus and the phase pressure differences in each region. This yields N pressure equations:

$$\sum_{i=1}^{k} \Delta P_{w,i} + \sum_{k+1}^{N+1} \Delta P_{o,i} = P_{c,k} + \Delta P, k = 1, 2, \cdots, N. \tag{3.23}$$

The flow rates of oil and water, $q_{o,k}$ and $q_{w,k}$, are expressed in the $N+1$ regions by a generalized Hagen-Poiseuille equation,

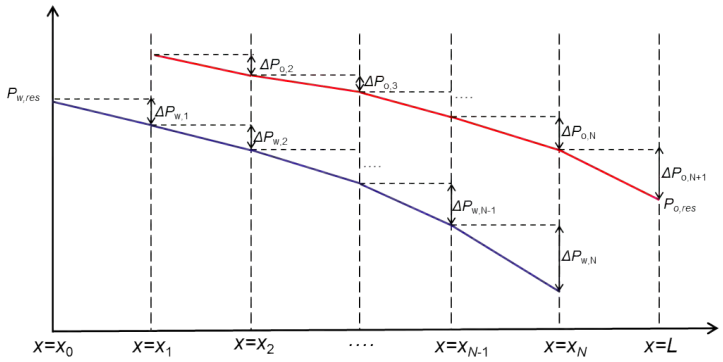

Figure 3.12: Schematic diagram of a possible profile of oil- and water-phase pressures in the interacting tube bundle model.

$$q_{o,k}(t) = \frac{g_{o,k}}{\mu_o} \frac{\Delta P_{o,k}(t)}{x_k(t) - x_{k-1}(t)}, \quad q_{w,k}(t) = \frac{g_{w,k}}{\mu_w} \frac{\Delta P_{w,k}(t)}{x_k(t) - x_{k-1}(t)}, \tag{3.24}$$

and by material balance as

$$q_{o,k}(t) = \sum_{i=1}^{k-1} \Delta A_{o,i} \frac{\Delta x_i(t)}{\Delta t}, \quad q_{w,k}(t) = \sum_{i=k}^{N} \Delta A_{w,i} \frac{\Delta x_i(t)}{\Delta t}. \tag{3.25}$$

In Eq. (3.25), $\Delta A_{o,i} = A_{o,i+1} - A_{o,i} = -\Delta A_{w,i}$ is the difference between cross-sectional areas invaded by oil in the length region between segments i and $i+1$, where $\Delta x_i(t)$ is the change in position of interface i during the time step Δt. Note that Eq. (3.25) is more general than the corresponding equation derived by Wang & Dong (2011) which is based on the areas of oil and water in each pore assuming all pores have the same triangular cross-sectional shape.

The water flow rate could also be expressed in terms of the injection rate q_{tot} as:

$$q_{w,1}(t) = q_{tot}, \cdots, q_{w,k} = q_{tot} - q_{o,k}, \cdots, q_{w,N+1} = 0. \tag{3.26}$$

Eqs. (3.24) and (3.25) are combined and inserted into Eq. (3.23), thus yielding N nonlinear equations that are solved for the N unknown interface positions, x_k, as a function of time when the pressure difference ΔP is constant. For constant rate displacements, the injection rate q_{tot} is given as an additional input parameter, whereas ΔP varies with time. In this case, the constant injection-rate condition,

$$q_{tot} = q_{w,1} = \sum_{i=1}^{N} \Delta A_{o,i} \frac{\Delta x_i(t)}{\Delta t}, \tag{3.27}$$

provides an additional equation, and a system of equations is solved by Newton-Raphson iterations for the $N+1$ unknown parameters $x_k, k = 1, \cdots, N$ and ΔP as a function of time. Further details regarding the solution procedure is provided by Dong et al. (2005); Wang & Dong (2011).

3.6.2 Computation of conductances

Pore space, oil and water conductances are obtained by computing the velocity profile directly in each cross-sectional fluid configuration determined by the semi-analytical model. We assume steady-state, laminar flow of incompressible fluids, with constant viscosity and no-slip conditions on all boundaries. The computations are performed by solving Poisson's equation on many different pore space geometries and fluid configurations.

Based on the data obtained, fluid conductance correlations are formulated as polynomial functions of areas and shape factors that seem to describe the data effectively. We distinguish between the conductance data for fluids occupying (i) the corners, (ii) the wider bulk portions of the pore space; and (iii) layers that are located between the bulk and corner occupancies. The fluid occupying the pore space as a layer could correspond to water residing in a narrow constriction for water-wet conditions, or oil that remains present in a mixed-wet pore space at negative capillary pressure after water has invaded its bulk portion.

The pore-space conductances g_P are approximated by the following correlation:

$$\frac{g_P}{A_P^2} = \sum_{i=1}^{2} a_i G_P^i, \tag{3.28}$$

where $a_1 = 3.17$ and $a_2 = 0.75$, and the pore shape factor $G_P = \frac{A_P}{{L_P}^2}$; note that A_P is the area of the pore space and L_P is the pore perimeter. The proposed functional form is motivated by previous works (Øren et al., 1998; Ryazanov et al., 2009) where it was demonstrated that conductances in tubes with idealized triangular and star-shaped cross-sections could be approximated by functions of areas and shape factors.

For the fluid occupying corner portions of the pore spaces, the following conductance correlation is proposed:

$$\frac{g_c}{A_c^2} = \sum_{i=1}^{2} b_i G_c^i, \tag{3.29}$$

where $b_1 = -4.0$, $b_2 = 0.8$ and G_c denotes the shape factor defined as $G_c = \frac{A_c}{L_c^2}$; here A_C and L_C are the area and the boundary length of the corner fluid configurations.

For irregular pore spaces, correlations expressed as functions of pore-space conductance and areas appear to describe the conductance data for the bulk and layer fluid occupancies more accurately than correlations based on shape factors (such as Eqs. (3.28) and (3.29)). The conductance of the fluid occupying the bulk portion of the pore space is approximated by:

$$\frac{g_B}{g_P} = \sum_{i=1}^{3} c_i \left(\frac{A_B}{A_P}\right)^i, \tag{3.30}$$

where $c_1 = -0.8$, $c_2 = 0.6$ and $c_3 = 1.2$. In Eq. (3.30), g_B and A_B denote the bulk-phase conductance and area, respectively.

The conductance of the fluid occupying the pore space as layers can be

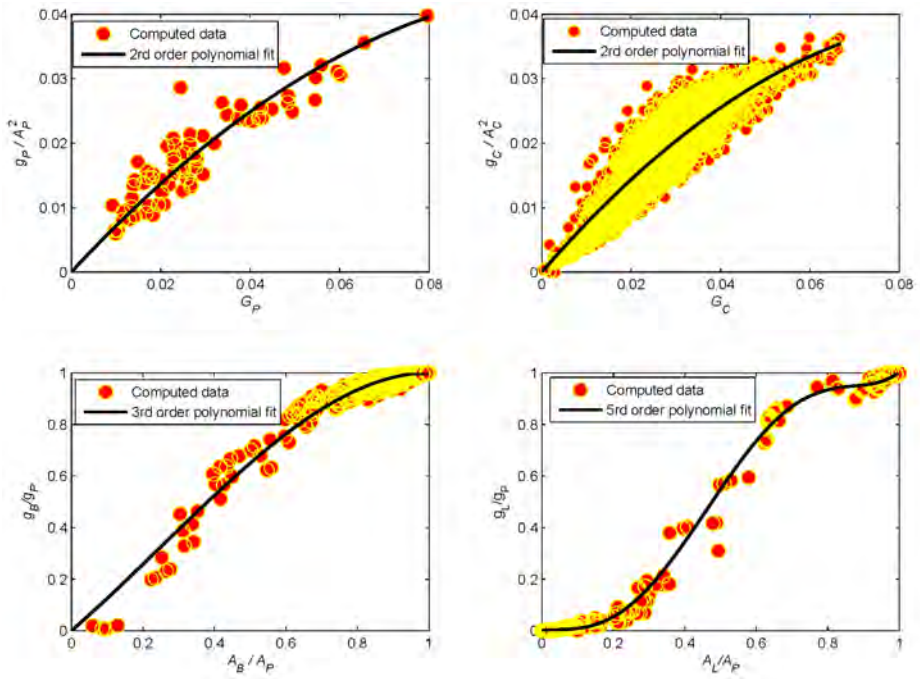

Figure 3.13: Dimensionless conductance correlations for the pore spaces (top, left), corner fluid configurations (top, right), bulk fluid configurations (bottom, left) and layer fluid configurations (bottom, right) plotted as functions of shape factors or area fraction. The correlations are compared with conductance data computed directly in the fluid configurations that occur during mixed-wet imbibition simulations performed with the semi-analytical model in a small subset of an SEM image of Bentheim sandstone.

computed from:

$$\frac{g_L}{g_P} = \sum_{i=1}^{5} d_i \left(\frac{A_L}{A_P}\right)^i, \tag{3.31}$$

where $d_1 = 13.34$, $d_2 = -30.74$, $d_3 = 20.67$, $d_4 = -2.45$ and $d_5 = 0.16$. In Eq. (3.31), g_L and A_L denote the layer conductance and area, respectively.

The computed data (red circles) and correlations presented in Figure 3.13 show that the correlations proposed by Eqs. (3.28) to (3.31) agree reasonably well with the computed data by solving Poisson's equation. We also compared the relative permeability (defined as the ratio of the phase conductance to pore space conductance) and saturation profile evolutions (computed using the interacting tube bundle model) based on conductance values obtained both from proposed physically-sound correlations and computed data for a small subset of the rock image (see Paper 4); the results show that the conductance correlations work satisfactorily to generate reliable conductance data.

3.6.3 Dynamic capillary pressure

Dynamic capillary pressure is defined as the difference of the average phase pressures (Hassanizadeh et al., 2002):

$$P_c^{dyn} = \langle P_o \rangle - \langle P_w \rangle, \tag{3.32}$$

where $\langle x \rangle$ denotes an average of quantity x.

Average phase pressure algorithm

Several averaging methods have been proposed in the literature to obtain average phase pressures (Korteland et al., 2010); we choose the volume averaging approach adopted by Dahle et al. (2005), who evaluated dynamic capillary pressure effects in a non-interacting tube bundle model. The volume-averaged phase pressures employed in our interacting tube

bundle model with $k = 1, \ldots, N+1$ length regions and N advancing front menisci, are given by

$$\langle P_\gamma \rangle = \frac{1}{V_\gamma(t)} \sum_{k=1}^{N+1} P_{\gamma,k} V_{\gamma,k}(t), \gamma = o, w, \tag{3.33}$$

where $V_{\gamma,k}(t)$ is volume of phase γ at time t in the length region k, and $P_{\gamma,k}$ is the mean phase pressure of phase γ evaluated in that region. If an interface reaches one of the reservoirs, the phase behind that interface is assumed to become trapped with a zero pressure gradient. In that case, this interface is eliminated from the interacting tube bundle calculations and the number of moving interfaces, N, is reduced by one. The phase pressure on the tube side of the interface is now given by the reservoir pressure of the present fluid, i.e., $P_{w,res}$ for water and $P_{o,res}$ for oil. We account for this behavior by modifying Eq. (3.33) to include the trapped phase compartments:

$$\langle P_\gamma \rangle = \frac{1}{V_\gamma(t) + V_{\gamma,trapped}} \{ \sum_{k=1}^{N+1} P_{\gamma,k} V_{\gamma,k}(t) + P_{\gamma,trapped} V_{\gamma,trapped} \}, \gamma = o, w, \tag{3.34}$$

where $P_{o,trapped} = P_{o,res}$ if the interface is trapped at $x = x_0$, or $P_{w,trapped} = P_{w,res}$ if the interface is trapped at $x = L$.

Simulation procedure

Drainage is simulated by increasing $-\Delta P = P_{o,res} - P_{w,res}$ stepwise by a pressure P_{step}, while $P_{w,res}$ is fixed. Initially, the tube bundle is occupied with water. For each pressure step, the set of interfaces satisfying the static capillary pressure data $-\Delta P \geq P_{c,k}^{stat}$ is placed inside the tube bundle at $x = L$. Interacting tube bundle simulations are performed to advance this set of interfaces in time. The phase pressures and volumes on each side of these interfaces belong to the first term in the right hand side of Eq. (3.34), whereas the phase pressures and volumes for the remaining

interfaces that are still trapped at $x = L$ belong to the second term in the right hand side of Eq. (3.34).

At each time step, the dynamic capillary pressure is calculated from Eqs. (3.32) and (3.34). When an interface reaches one of the reservoirs, this interface becomes trapped, and the amount of fluid volume behind the interface is transferred from $V_{\gamma,k}$ to $V_{\gamma,trapped}$, and the phase pressure in this fluid compartment is changed from $P_{\gamma,k}$ to $P_{\gamma,trapped}$. The interacting tube bundle model then continues to advance the interfaces still present in the remaining tubes that satisfy the condition $-\Delta P \geq P_{c,k}^{stat}$. When all interfaces have reached the tube ends, the pressure difference $-\Delta P$ is increased again, and a new set of interfaces satisfying $-\Delta P \geq P_{c,k}^{stat}$ is advanced by the interacting tube bundle model.

Imbibition is performed by increasing $\Delta P = P_{w,res} - P_{o,res}$ stepwise by the pressure P_{step}, while $P_{o,res}$ is fixed. Initially, the tube bundle is occupied with oil and remaining water after drainage, representing the initial water saturation $S_{w,i}$. For each pressure step, the set of interfaces satisfying the static capillary pressure data $-\Delta P \leq P_{c,k}^{stat}$ is placed inside the tube bundle at $x = x_0$. The interacting tube bundle model is utilized to advance this set of interfaces in time. Again, the phase pressures and volumes on each side of these moving interfaces belong to the first term on the right hand side of Eq. (3.34), whereas the phase pressures and volumes for the remaining interfaces that are still trapped at $x = x_0$ belong to the second term in Eq. (3.34).

For each time step, dynamic capillary pressure is calculated from Eqs. (3.32) and (3.34). When an interface reaches one of the reservoirs, this interface becomes trapped, and the amount of fluid volume behind the interface is transferred $V_{\gamma,k}$ to $V_{\gamma,trapped}$, and the phase pressure in this fluid part is changed from $P_{\gamma,k}$ to $P_{\gamma,trapped}$. The interacting tube bundle model then continues to advance the interfaces still present in the tubes. When all interfaces have reached the tube ends, the pressure difference is increased by P_{step} again, and the new set of interfaces satisfying $-\Delta P \leq P_{c,k}^{stat}$ is advanced by the interacting tube bundle model.

Series of dynamic capillary pressure curves both for drainage and imbibition are computed with various P_{step}, which will be used to evaluate the dynamic coefficient τ.

Dynamic coefficient of capillary pressure

As mentioned in the literature review, the dynamic coefficient, τ, is a function of saturation and independent of desaturation rate (Bottero et al., 2006; Schembre & Kovscek, 2006; Camps-Roach et al., 2010; O'Carroll et al., 2010).

The dynamic coefficient, τ, is computed by plotting the difference between dynamic and static capillary pressure, $P_c^{dyn} - P_c^{stat}$, against the time derivative of water saturation, $\frac{\partial S_w}{\partial t}$, for constant water saturation with various pressure steps. The dynamic coefficient does not depend on the time derivative of the water saturation if $(P_c^{dyn} - P_c^{stat})$ vs $-\frac{\partial S_w}{\partial t}$ is given by a straight line. However, in the literature it has been suggested that such straight line could have a nonzero intercept with the ordinate (Hassanizadeh et al., 2002; Dahle et al., 2005; Mirzaei & Das, 2007), indicating that Eq. (2.3) should be replaced by an equation of the form

$$P_c^{dyn} - P_c^{stat} = -\tau \frac{\partial S_w}{\partial t} + C. \tag{3.35}$$

If $C = 0$, the difference between dynamic and static capillary pressure vanishes at equilibrium, i.e., $\frac{\partial S_w}{\partial t} = 0$ and the equilibrium fluid configuration is equal to the configuration obtained by slow capillary-controlled displacement. If $C \neq 0$, a difference between dynamic and static capillary pressures exists for $\frac{\partial S_w}{\partial t} = 0$. This corresponds to an equilibrium configuration that differs from the configuration that would be obtained by a capillary-controlled displacement.

3.7 Application

The developed semi-analytical pore scale model serves as a useful tool to efficiently compute capillary pressure curves and fluid configurations in realistic, highly-irregular pore spaces directly extracted from rock images, which allows us to investigate the effect of wettability, initial water saturation and pore space geometry on the capillary pressures and associated fluid configurations.

The model offers the possibility of linking pore scale displacement mechanisms and wettability state to capillary pressure curves, and thus it allows us to formulate a dimensionless capillary pressure function at arbitrary mixed-wet conditions; this makes it possible to describe the variability of wettability and permeability more accurately in reservoir simulation models. This also allows for improved evaluation of core-sample laboratory experiments and reservoir performance. The dimensionless J-function can also be applied together with data or existing capillary pressure correlations for use in reservoir simulation. Reliable capillary pressure correlations could also be suggested based on the computed data, in particular with respect to the pore-scale displacement mechanisms, fluid configurations, the capillary levels and saturation dependencies.

The relative permeability (defined as the ratio of phase conductance to pore conductance) curves could also be obtained by computing the phase conductances for the computed fluid configurations. This can be done either by solving Poisson's equation for determined geometries with proper boundary conditions or by developing physically-sound correlations from numerical data. This procedure could also be used to formulate reliable relative permeability correlations for various wettability and initial saturations.

Transient behavior of viscous- and capillary-dominated water invasion in rock images at mixed-wet conditions could also be performed using the computed capillary pressure and relative permeability with a physically-sound model, such as the interacting tube bundle model, which conse-

quently provides insights into the pore-scale mechanisms of waterflooding and relates their effects to the computed macro-scale properties, which allows for improved interpretation of core-scale experiments.

Dynamic effects in capillary pressure curves at mixed-wet conditions could be quantified using the so-called interacting tube bundle model with a proper phase averaging algorithm. The results provide insights into the extent of dynamic effects in capillary pressure curves for realistic mixed-wet pore spaces, which could contribute to improved interpretation of core-scale experiments. The simulated capillary pressure curves obtained with the pore-scale model could also be applied in reservoir simulation models to assess dynamic pore-scale effects on the Darcy scale.

In the proposed model, pore space is represented by a bundle of straight tubes with irregular cross-sections from 2D rock images. Thus, pore interconnectivity and phase entrapment is absent in our model. This would at least affect the endpoint saturations and the level of the capillary pressure curves. To overcome this, a 3D pore surface correction and pore connectivity factor (Virnovsky et al., 2009) could be introduced to compare the capillary pressure curves measured from laboratory. For the dynamic modeling, the phase trapping could be implemented by taking 2D rock images of different core sections and run the developed interacting tube bundle model on each image while introducing physically-based rules that account for the connectivity and trapping between the different sections, potentially by following the work of Wang & Dong (2011) who considered idealized tubes with equilateral, triangular cross-sections of different size in each cross section.

Chapter 4

Results and Discussion

Simulations to obtain two- and three-phase capillary pressure curves and associated fluid configurations and saturation profile evolutions are performed with our proposed models in a Bentheim sandstone SEM image; subsequently, dynamic capillary pressure curves are computed within a subset of the main image. The image resolution is 0.204 μm/pixel, it contains 1134x761 pixels and 293 separate pore spaces; the computed porosity and permeability are 0.17 and 0.76×10^{-12} m^2, respectively. The image permeability is computed by solving Poisson's equation directly in the identified pore spaces.

4.1 Two-phase capillary pressure curves

Capillary pressure curves are computed in the main rock image described above for both primary drainage at uniform water-wet condition and imbibition at mixed-wet conditions. The oil/water interfacial tension is set equal to $\sigma_{ow} = 0.050$ N/m for all simulations.

4.1.1 Drainage capillary pressure and fluid configurations at uniformly-wet conditions

The drainage capillary pressure curves computed from the semi-analytical model at uniformly-wet conditions are shown in Figure 4.1(a). Obviously, wettability affects the level of the capillary pressure curves, and this also confirmed by the fluid configurations occurring in the rock image, as shown in Figure 4.2. Figure 4.2(a) shows the oil-water distribution in a strongly water-wet system, $\theta = 0°$, and Figure 4.2(b) depicts the oil-water distribution at the same capillary pressure in a less water-wet system with $\theta = 30°$. These results illustrate that for the same capillary pressure, in the less water-wet system oil has invaded pores, or pore areas that have not yet invaded in the strongly water-wet system. Therefore, at a given capillary pressure, the water saturation in the strongly water-wet system ($\theta = 0°$) will be higher than the one for a less water-wet system (e.g., $\theta = 30°$).

The traditional J-function, that accounts for wettability effects in the rock image, can be used to scale the capillary pressure curves at uniformly-wet conditions. As shown in Figure 4.1(b), a unique curve $\frac{P_c}{\cos\theta}$ is obtained regardless the contact angle (wettability) of the rock.

4.1.2 Capillary pressure and fluid configurations at mixed-wet conditions

Imbibition capillary pressure curves at mixed-wet conditions are computed in the main rock image for different contact angles and maximum capillary pressure values at the end of primary drainage. First, the primary drainage processes are simulated until a selected maximum capillary pressure $P^{pd}_{c,max}$ (or reversal capillary pressure, $P_{c,rev}$) is reached. This establishes different initial conditions for the subsequent imbibition runs. The pore-boundary segments contacted by oil after primary drainage are assumed to undergo a wettability alteration, and therefore these segments are described by a different contact angle in the following imbibition pro-

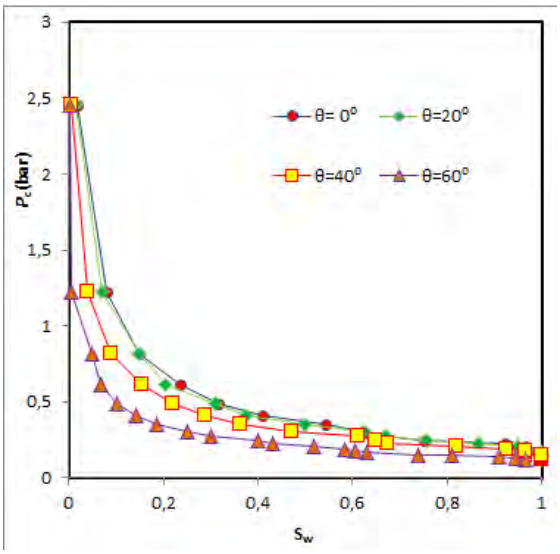

(a) Capillary pressure

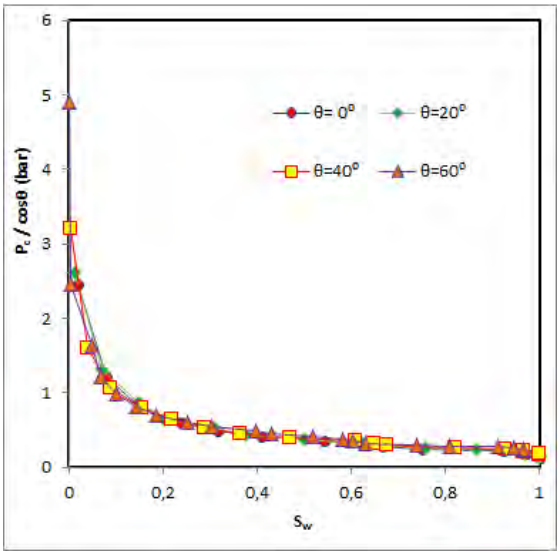

(b) Capillary pressure divided by $\cos\theta$

Figure 4.1: Capillary pressure curves at uniformly-wet conditions for different contact angles: (a) capillary pressure, (b) capillary pressure scaled by the contact angle.

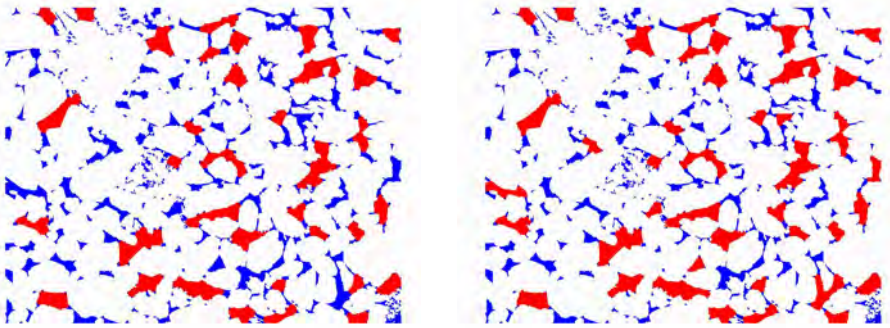

(a) $\theta = 0°$ (b) $\theta = 30°$

Figure 4.2: Fluid configurations at uniformly-wet conditions at a given capillary pressure, $r_{ow} = 6$ pixel lengths.

cess than that used in the primary drainage. The wetting condition for imbibition is described by θ_c which is determined from Eq. (3.14).

Examples of capillary pressure curves for imbibition processes simulated with three different contact angles determined from Eq. (3.14) are presented in Figure 4.3(a) together with the capillary pressure curve for primary drainage. The spontaneous imbibition sections of the capillary pressure curves are shown to increase significantly when θ_o changes from 180° to 120°. Imbibition capillary pressure curves for $\theta_o = 180°$ that are simulated starting from four different initial water saturation conditions ($S_{wi} = 0.018, 0.081, 0.150$ and 0.237) are presented in Figure 4.3(b). A comparison of these four imbibition capillary curves indicates that the level of capillary pressure during imbibition also increases with the increased value of the initial water saturation S_{wi} due to an increased water-wet area in the pore-space corners at higher S_{wi} values. This clearly suggests that the formation wettability is a function of the initial water saturation at the onset of the imbibition process. Such behavior is well-known and has been observed in core-scale measurements (Jadhunandan & Morrow, 1995) and explained by pore-scale modeling (Helland & Skjæveland, 2006a).

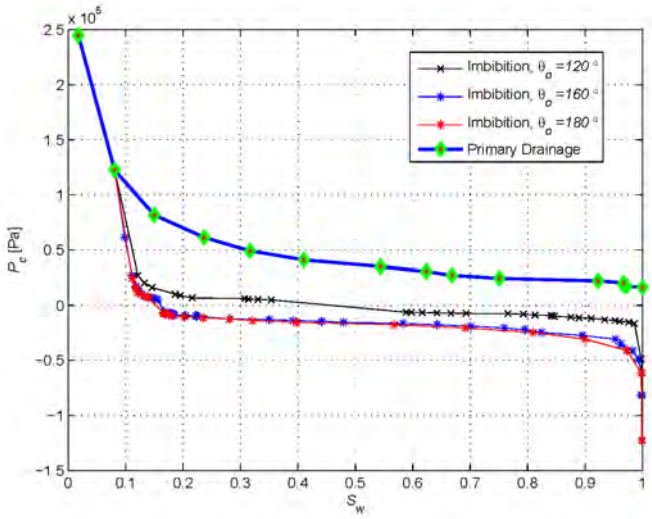

(a) $\theta_w = 0^\circ$ and $S_{wi} = 0.081$

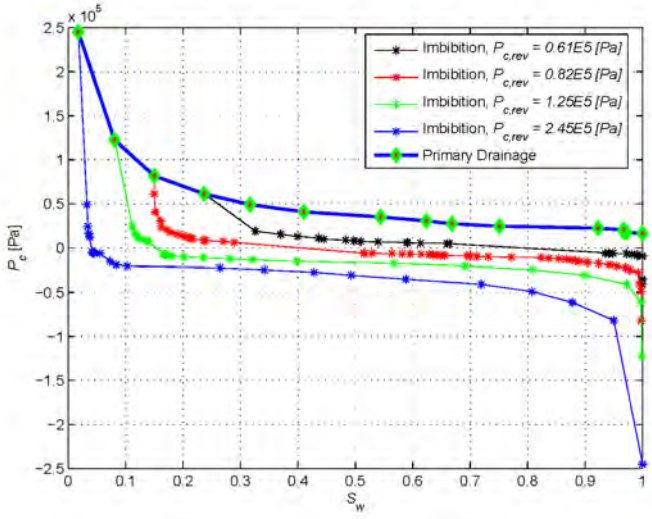

(b) $\theta_w = 0^\circ$ and $\theta_o = 180^\circ$

Figure 4.3: Capillary pressure curves for the primary drainage at strongly water-wet conditions followed by imbibition processes at several mixed-wet conditions.

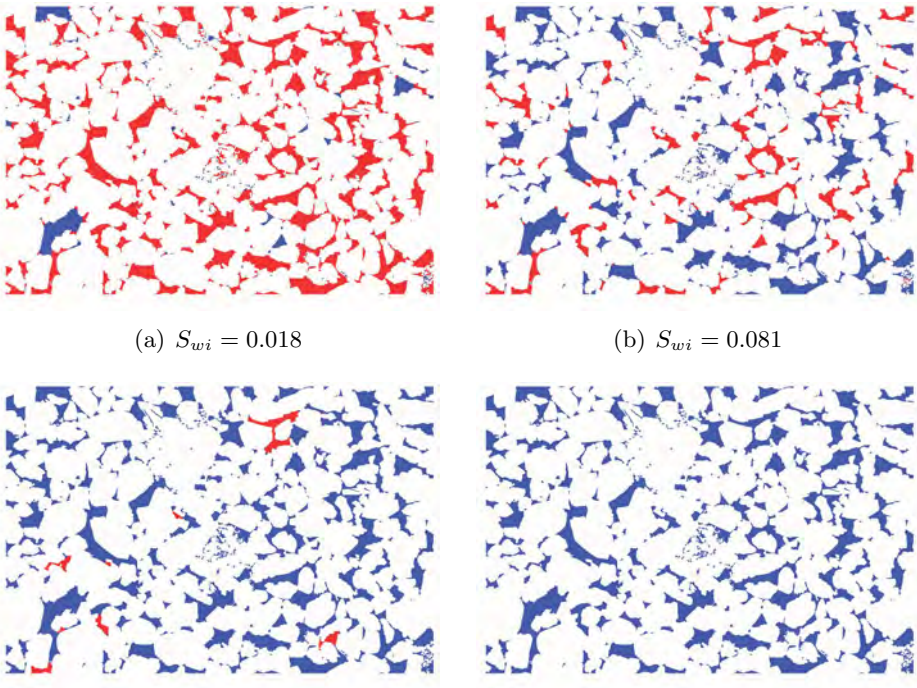

(a) $S_{wi} = 0.018$ (b) $S_{wi} = 0.081$

(c) $S_{wi} = 0.150$ (d) $S_{wi} = 0.237$

Figure 4.4: Fluid configurations during imbibition processes at mixed-wet conditions in an SEM image of Bentheim sandstone as simulated with the semi-analytical model. All images are taken at capillary pressure $P_c = -2.04 \times 10^4$ Pa during the imbibition simulations for $\theta_w = 0°$ and $\theta_o = 180°$ that are initiated from four different initial water saturations which are shown at the bottom of each panel.

Figure 4.4 presents fluid configurations at a constant negative capillary pressure value of $P_c = -2.04 \times 10^4$ Pa for imbibition processes originating from different initial water saturation ($S_{wi} = 0.018, 0.081, 0.150$ and 0.237). The contact angles $\theta_o = 180°$, $\theta_w = 0°$ were applied in all cases. Figure 4.4(a) shows that water in general invades first the larger pore spaces for the smallest initial water saturation ($S_{wi} = 0.018$). For intermediate values of S_{wi}, water invades some of the largest and several of the smallest pore spaces at a given capillary pressure, leaving the intermediate-sized pore spaces still occupied by oil in the bulk areas while water remains present in the pore corners that were not invaded by oil at the end of primary drainage, see Figure 4.4(b) and Figure 4.4(c). This non-monotonic invasion order of the pore sizes occurs because the fractional area of oil-wet surfaces are likely to be higher in large pore spaces, which therefore exhibit a more oil-wet behavior than the smaller pore spaces under these conditions. Figure 4.4(b) also shows that several oil layers of varying size and shape were formed in the highly irregular pore geometries. Finally for the largest S_{wi} case, all pore spaces are invaded by water at the selected capillary pressure ($P_c = -2.04 \times 10^4$ Pa), as shown in Figure 4.4(d).

4.1.3 Dimensionless capillary pressure function for mixed-wet conditions

Based on the simulated capillary pressure curves at various mixed-wet conditions, an improved J-function is proposed based on the following relationship,

$$J(S_w) = \frac{P_c}{\sigma[|\cos\theta^w_{eff}|H(P_c) + |\cos\theta^o_{eff}|H(-P_c)]}\sqrt{\frac{K}{\phi}}. \qquad (4.1)$$

In this equation, H is the Heaviside step function, and $\cos\theta^w_{eff}$ and $\cos\theta^o_{eff}$ denote the effective contact angles both for the water-wet and oil-wet parts of the pore space, respectively. These effective contact an-

gles can be related to wetting indices defined on the core scale, in order to apply the proposed dimensionless capillary pressure J-function on core samples. Based on pore-scale simulation, the following correlations were determined:

$$\begin{aligned} cos\theta^{w}_{eff} &= 0.068 \times WI + 0.38; \\ cos\theta^{o}_{eff} &= 0.2041 \ln(WI) + 0.1536. \end{aligned} \tag{4.2}$$

The wetting index is defined as

$$WI = \frac{S_{w0} - S_{wi}}{1 - S_{wi} - S_{or}}, \tag{4.3}$$

where S_{w0} is the water saturation at zero capillary pressure, and S_{or} is the residual oil saturation at the end of imbibition. In the simulations performed with the semi-analytical model, S_{or} is zero, or close to zero, because the assumed pore space is formed by a bundle of straight tubes cross-sections of arbitrary shapes.

The proposed J-function (Eq. (4.1)) is utilized to reproduce simulated data in order to test its accuracy. The original and reproduced imbibition capillary pressure curves for $\theta_o = 160^\circ$ and $\theta_o = 180^\circ$ are shown in Figure 4.5 for all four assumed initial water saturations at the start of imbibition. The figure shows that the reproduced capillary pressure curves for the smaller initial water saturations are located slightly below the original capillary pressure values at large water saturations, whereas the reproduced and original capillary pressure curves from the larger initial water saturations exhibit excellent agreement. This is because the capillary entry pressures for large initial water saturations depend strongly on the initial fluid configurations, which is a feature we have aimed at incorporating in the dimensionless capillary pressure function.

It is therefore demonstrated that the proposed J-function works satisfactorily for mixed-wet conditions. A particularly accurate description seems to be obtained when the entry pressures depend strongly on the

Table 4.1: Fundamental parameters of cores samples used to measure mixed-wet capillary pressure curves (Lomeland & Ebeltoft, 2008).

Sample number	Rock type	Permeability [mD]	Porosity [-]
1	Sandstone	29.1	0.192
2	Sandstone	3.04	0.111
3	Sandstone	4345	0.311
4	Sandstone	0.05	0.0504

initial water saturations. More details can be found in Paper 2.

Validation against core-scale laboratory measurements

Lomeland & Ebeltoft (2008) presented laboratory measurements of oil/ water capillary pressure data in four core samples from a Norwegian Continental Shelf oil field. The authors used both the porous plate and centrifuge techniques to obtain the reported capillary pressure data. The basic petrophysical parameters of the core samples used in these measurements are given in Table 4.1. The oil used in the first three measurements was crude oil, while in the last measurement it was a synthetic oil. The oil-water interfacial tension was not reported by the authors, and in this work its value was assumed to be equal to 0.05 N/m.

The measured capillary pressure data for the four different rock samples, shown in Figure 4.6(a), exhibit significant variations in initial water saturation, residual oil saturation and water wetting indices. For rock samples 1 and 2, the imbibition capillary pressure data, both spontaneous and forced imbibition, were measured by the porous plate technique following the primary drainage measurements. The imbibition capillary pressure data for samples 3 and 4 were measured using the centrifuge technique and the secondary drainage was adopted as the positive part of the imbibition capillary pressure curves. The dimensionless capillary pressure data scaled by Eqs. (4.1)-(4.2) are shown in Figure 4.6(b); a unique curve is obtained for the four capillary pressure curves despite the significant difference in the cores' properties such as permeability, porosity, initial

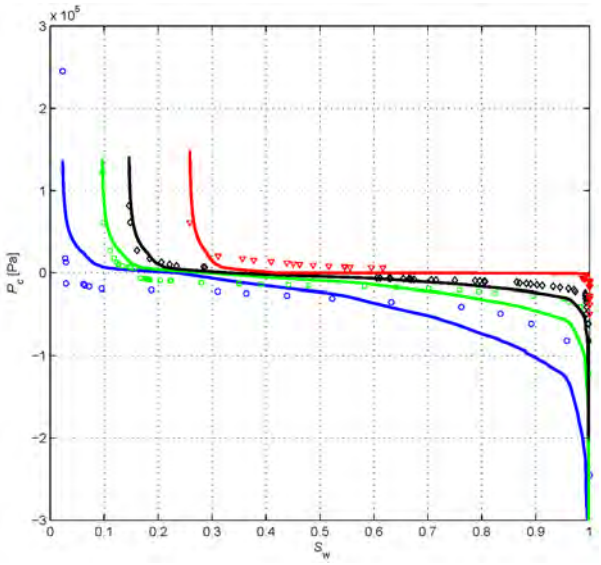

(a) $\theta_w = 0^\circ$ and $\theta_o = 160^\circ$

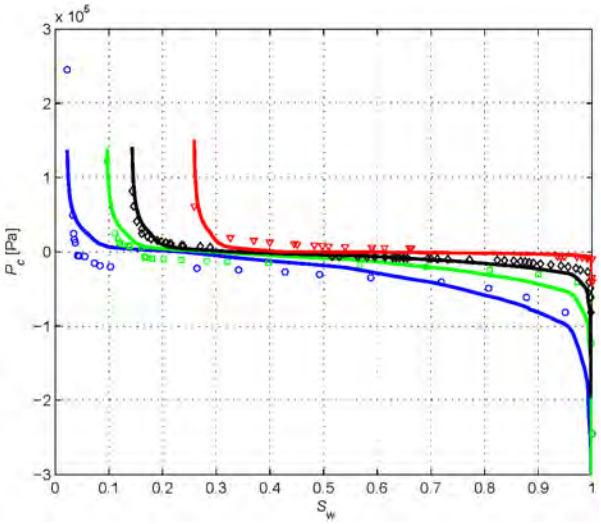

(b) $\theta_w = 0^\circ$ and $\theta_o = 180^\circ$

Figure 4.5: Imbibition capillary pressure curves at mixed-wet conditions as simulated with the semi-analytical model (symbols) and reproduced (curves) by the dimensionless capillary pressure function given in Eq. (4.1) (blue: $S_{wi} = 0.018$, green: $S_{wi} = 0.081$, black: $S_{wi} = 0.150$ and red: $S_{wi} = 0.237$).

water saturation, residual oil saturation and wettability.

The derived average J-function was then used to reproduce the four capillary pressure curves which are shown along with the original laboratory measurements in Figure 4.7. The comparison between the experimental and reproduced capillary pressure curves is excellent for all four core samples. This demonstrates that the proposed novel J-function introduced in this work can be used to scale measured capillary pressure curves with different permeability, porosity, initial water saturation, residual oil saturation and wettability at mixed-wet conditions.

4.2 Saturation profile evolution at mixed-wet conditions

Water saturation profile evolution during oil displacement by water under mixed-wet conditions are simulated using the so-called interacting tube bundle model. The effects of wettability θ_o and initial water saturation on the water saturation profile evolution are investigated. The results shown in these runs are for two flow rates, a moderate injection rate of $q_{tot} = 3.14 \times 10^{-4}$ m^3/s and a high injection rate of $q_{tot} = 3.14 \times 10^{-3}$ m^3/s, which corresponds to capillary numbers of (see Eq. (2.1)) $CA = 6.24 \times 10^{-6}$ and $CA = 6.24 \times 10^{-5}$, respectively.

4.2.1 Effects of wettability

Saturation profiles simulated with the interacting tube bundle model for the moderate flow rate water floods initiated from $S_{wi} = 0.081$ and three different contact angle conditions ($\theta_o = 120°, 160°$ and $180°$) are presented in Figure 4.8. The high and positive oil-water capillary pressure at small water saturations promote water invasion and advancement of the associated front menisci. The simulated water saturation profiles exhibit a gradual trend and become almost horizontal with time in small water saturations irrespective of the contact angle θ_o. Capillary pressure is less

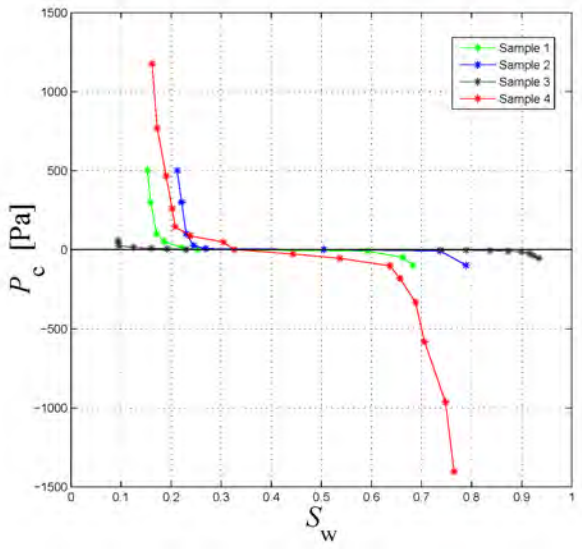

(a) Capillary pressure curves

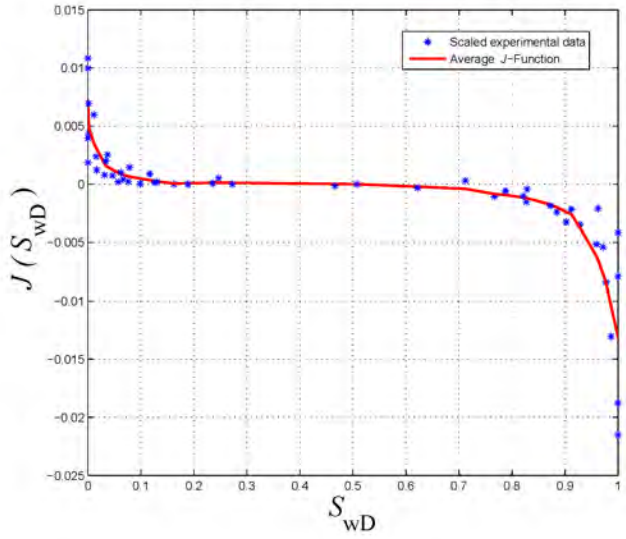

(b) Improved J-function

Figure 4.6: (a) Mixed-wet capillary pressure curves, and (b) improved J-function curve. Laboratory measurements are from Lomeland & Ebeltoft (2008).

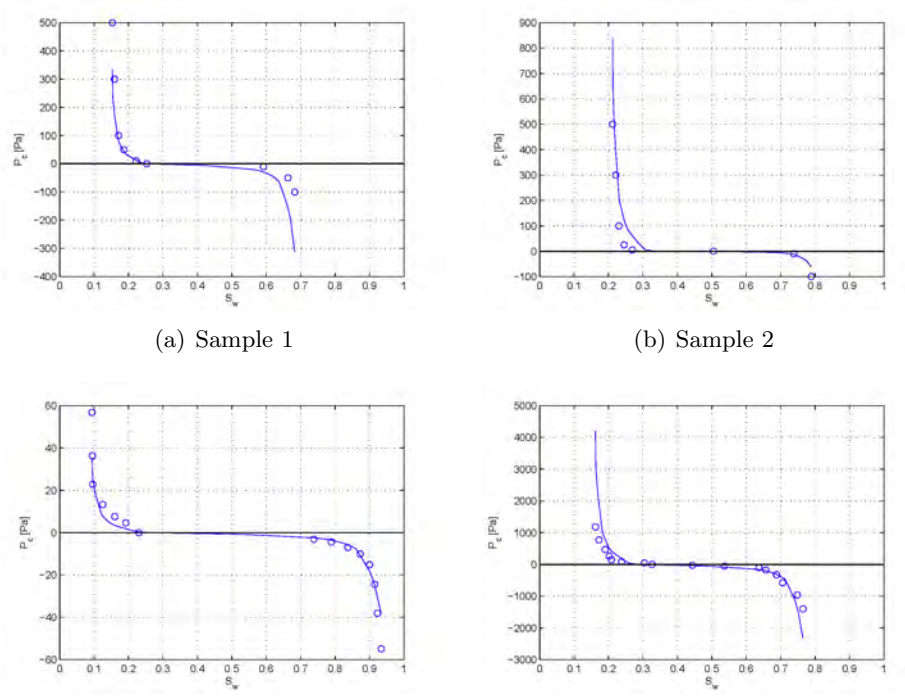

(a) Sample 1

(b) Sample 2

(c) Sample 3

(d) Sample 4

Figure 4.7: Reproduced imbibition capillary pressure curves (solid curves) computed from the average J-function and experimental core measurements reported by Lomeland & Ebeltoft (2008) (open circles) at mixed wet conditions.

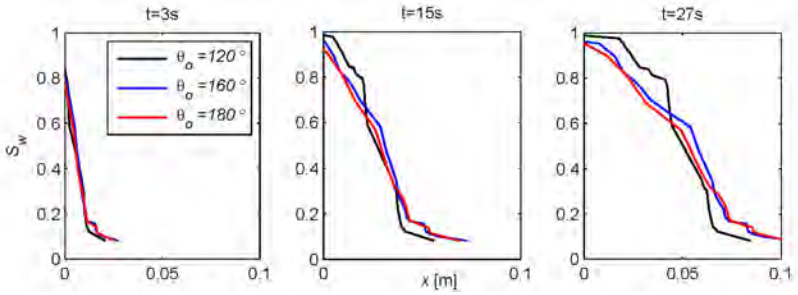

Figure 4.8: Evolution of water saturation profile at different wetting conditions during water flood conducted at a moderate flow rate $q_{tot} = 3.14 \times 10^{-4}$ m^3/s and from an initial water saturation of $S_{wi} = 0.081$.

important for the water saturation front at intermediate water saturations. In this saturation range, the capillary pressures (see Figure 4.3(a)) are small and negative when $\theta_o = 160°$ and $\theta_o = 180°$, and small and positive when $\theta_o = 120°$, which results in the formation of steeper but still gradual saturation fronts. For high water saturations, the oil-water capillary pressures are large and negative; in this region the saturation fronts become more gradual again, particularly for the water flood performed with $\theta_o = 180°$, where the displacement involved occur by water invasion into the smaller pore spaces as well as displacement of oil layers that have formed at smaller water saturations. Note that negative capillary pressures work to prevent water invasion into the pore spaces. In the interacting tube bundle model, the front menisci associated with the largest negative capillary pressures retract, which leads to the displacement of water by oil, and the water saturation fronts develop pronounced gradual shapes in time for zero flow rates (see more details in Paper 3).

4.2.2 Effects of initial water saturation

Figure 4.9 presents water saturation profiles at different times for moderate ($q_{tot} = 3.14 \times 10^{-4}$ m^3/s) and high ($q_{tot} = 3.14 \times 10^{-3}$ m^3/s) flow rate water floods that are initiated from four different initial saturations

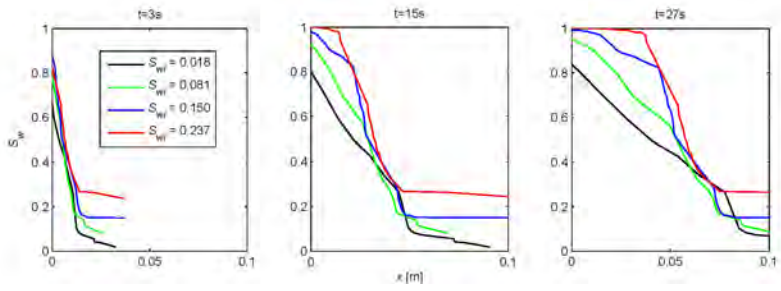

(a) Moderate flow rate, $CA = 6.24 \times 10^{-6}$

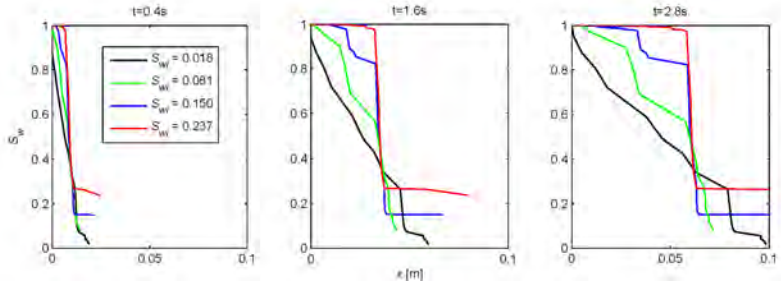

(b) High flow rate, $CA = 6.24 \times 10^{-5}$

Figure 4.9: Evolution of water saturation profiles for water floods conducted at moderate and high flow rates ($q_{tot} = 3.14 \times 10^{-4}$ m^3/s, $q_{tot} = 3.14 \times 10^{-3}$ m^3/s) and different initial water saturations ($S_{wi} = 0.0018, 0.081, 0.450$ and 0.237). The mixed-wet states are described by the contact angle of $\theta_o = 180°$ and the four initial water saturations.

($S_{wi} = 0.0018, 0.081, 0.150$ and 0.237) and for $\theta_o = 180°$. The results show that gradual saturation fronts are developed in this case. For low water saturations close to S_{wi}, the capillary pressure (see Figure 4.3(b)) is positive and large which results in gradual and almost horizontal saturation fronts.

For the intermediate water saturation, the cases of small initial water saturations, $S_{wi} = 0.0018$ and 0.081, resulted in pronounced gradual water saturation fronts because the oil-water capillary pressures (see Figure 4.3(b)) are negative and relatively large. For the larger initial water

saturations, $S_{wi} = 0.150$ and 0.237, the fronts become steeper in the intermediate water saturation range because the corresponding capillary pressures are less significant and closer to zero (see Figure 4.3(b)). This is explained by the capillary entry pressures which are negative for small S_{wi} but they become closer to zero, or even positive, as the water content present in the pore-space corners increases with S_{wi}. At intermediate saturations, steep Buckley-Leverett fronts form and prevail at all times in the water floods simulated with high flow rates.

At large water saturations, the capillary pressure is negative and large for all water floods, and the saturation profiles become again more gradual in this saturation range. For the moderate flow rate, the front menisci associated with the largest and negative capillary pressures (see Figure 4.3(b)) move in the negative x-direction and water is displaced by oil. This results in a pronounced gradual trend as the saturation fronts develop with time. Figure 4.9(b) also shows that the simulated high flow rate water floods at different wettability conditions exhibit pronounced differences even though the capillary pressure contribution is less important.

4.3 Dynamic capillary pressure curves

A subset of an SEM image of Bentheim sandstone rock containing 20 pore spaces with irregular and complex shapes is taken as input to the modeling procedures. Static capillary pressure and conductance data are computed by the semi-analytical model for primary drainage at strongly water-wet conditions and for the subsequent imbibition processes at mixed-wet conditions initiated from four different initial saturations ($S_{wi} = 0.0066, 0.036, 0.10$ and 0.18). The contact angle for the drainage is $\theta_w = 0^\circ$, and the contact angles employed in the imbibition simulations are $\theta_w = 0^\circ$ and $\theta_c = 180^\circ$. The simulated data (capillary pressure, conductances) from these processes are taken as input to the interacting tube bundle model for simulating dynamic capillary pressures for an oil viscosity 0.01 Pa-s, water viscosity 0.001 Pa-s and a tube bundle length of 0.1

m.

4.3.1 Dynamic capillary pressure curves

Dynamic capillary pressure curves for primary drainage at water-wet conditions, and for imbibition at mixed-wet conditions, are computed following the procedure described in the model description part (Section 3.6.3). The simulated results are shown in Figure 4.10. As shown in this figure, the difference between dynamic and static capillary pressures at a determined water saturation depends on P_{step} that has been deployed on each dynamic curve; this is because a larger pressure difference ΔP is applied when a relatively bigger P_{step} is used in the simulation.

The dynamic capillary pressure curves for drainage are located at a higher level than the static capillary pressure curve, whereas the dynamic imbibition curves are located at levels lower than the static one. As expected, the main trend is an increasing difference between dynamic and static capillary pressure for an increasing P_{step} (Hassanizadeh et al., 2002; Dahle et al., 2005; Mirzaei & Das, 2007). However, for low water saturations, the dynamic capillary pressure plateaus associated with the different constant pressure differences are not always monotonically increasing with P_{step} during drainage. This is an effect of the finite resolution of the static capillary pressure curve and the fact that the flow processes are carried out by changing ΔP in a stepwise fashion.

Generally, the dynamic capillary pressure curves do not coincide with the static curve when all interfaces are located at the tube end-points. This is due to the interacting tube bundle model which attempts to arrange the moving interfaces associated with increasing entry pressures and velocities in the order of increasing positions x_k (see Figure 3.11). Therefore, interfaces with the largest entry pressures satisfying $-\Delta P \geq P_{o,res} - P_{w,res}$ during drainage may become trapped at the oil reservoir, whereas during imbibition the interfaces with the smallest capillary entry pressures satisfying $-\Delta P \leq P_{o,res} - P_{w,res}$ may become trapped at the water reservoir.

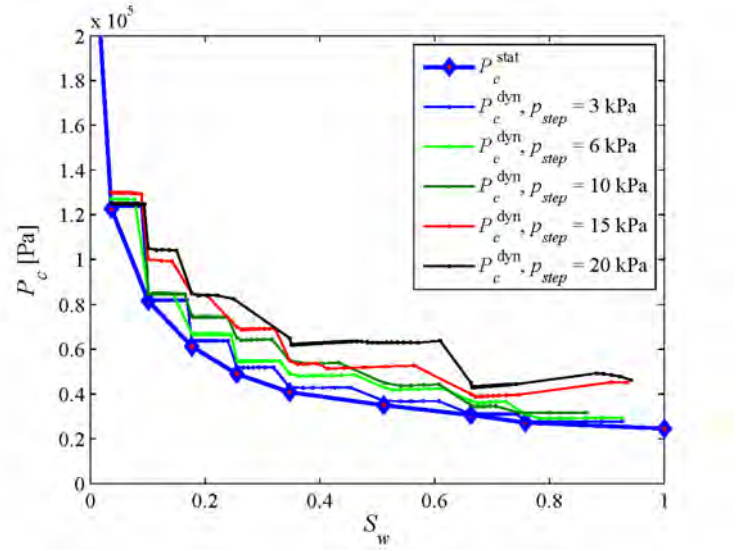

(a) Drainage processes at water-wet conditions.

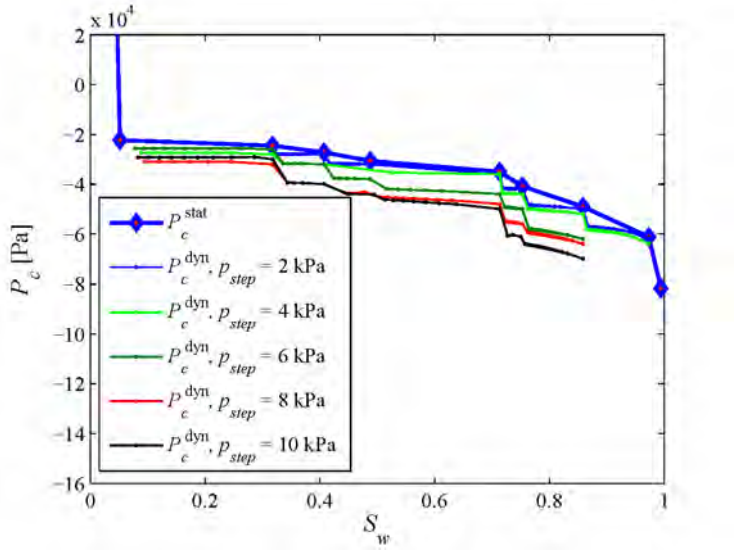

(b) Imbibition processes at mixed-wet conditions.

Figure 4.10: Dynamic and static capillary pressure curves computed in the subset of an SEM image of Bentheim sandstone.

The drainage dynamic capillary pressure curves also exhibit non-monotonic behavior as a function of water saturation in the various plateaus associated with different constant pressure differences ΔP (see Figure 4.10(a)). The dynamic capillary pressure plateaus at constant ΔP are decreasing slightly with time at high water saturations, whereas for smaller water saturations the dynamic plateaus at constant ΔP are increasing with time. At high water saturations, $P_{o,k}$ decreases in time as the interfaces move toward the water reservoir, implying that $\langle P_o \rangle$ decreases with time. At this stage, the average water pressure is approximately constant because its main contribution is due to the interfaces trapped at the oil reservoir, and hence P_c^{dyn} may decrease with time for large saturations. However, when interfaces arrive at the water reservoir, the oil pressures increase to $P_{o,res}$ and $\langle P_o \rangle$ starts to increase with time, whereas the main contribution to $\langle P_w \rangle$ at this stage is due to moving interfaces, implying that P_c^{dyn} may increase with time at small saturations. This effect is also observed in the imbibition simulations where P_c^{dyn} increases with time when ΔP is constant at small water saturations and decreases with time for constant ΔP at larger saturations. These results are in agreement with simulation results performed with a non-interacting tube bundle model (Dahle et al., 2005).

The resulting dynamic imbibition capillary pressure curves are presented in Figure 4.10(b). The dynamic capillary pressure, in segments of constant pressure difference ΔP, exhibits a more pronounced decline with increasing water saturations. A similar trend was observed in the dynamic drainage simulations conducted at uniform water-wet conditions where the dynamic capillary pressure in segments of constant ΔP increases more at low water saturations.

4.3.2 Dynamic coefficients

The dynamic coefficient is estimated by plotting $(P_c^{dyn} - P_c^{stat})$ against $-\frac{\partial S_w}{\partial t}$ based on Eq. (3.35) for a given water saturation and at various

pressure steps (P_{step}).

Figure 4.11 shows that the computed ($P_c^{dyn} - P_c^{stat}$) vs $-\frac{\partial S_w}{\partial t}$ data for the four water saturation values considered ($S_w = 0.29, 0.38, 0.60$ and 0.70 for drainage and $S_w = 0.15, 0.35, 0.55$ and 0.80 for imbibition), display a linear relationship; straight lines are fitted to the data sets for each water saturation. The good fit indicates that the dynamic coefficient is independent of the pressure step, P_{step}, used for both drainage and imbibition.

During drainage, the overall trend is that the fitted straight lines have an increasing slope, and consequently an increasing dynamic coefficient, as the water saturation decreases. This is also in agreement with the results presented by Dahle et al. (2005) and Mirzaei & Das (2007).

As opposed to the simulated ($P_c^{dyn} - P_c^{stat}$) vs $-\frac{\partial S_w}{\partial t}$ data at uniformly water-wet conditions, the general trend for imbibition at mixed-wet conditions shows that the dynamic coefficient increases with water saturation. This in turn would suggest that the dynamic coefficient is larger for saturation intervals where the slopes of the static capillary pressure curves are steeper.

The effects of the initial water saturation on the dynamic coefficient is also investigated as shown in Figure 4.12. In this figure, the computed ($P_c^{dyn} - P_c^{stat}$) vs $-\frac{\partial S_w}{\partial t}$ data for two different initial water saturations at four constant water saturations ($S_w = 0.15, 0.40, 0.68$ and 0.87) are shown along with the linear correlations fitted to these data sets. Generally, the straight lines fitted through the simulated data indicate that the dynamic capillary coefficient increases with decreasing initial water saturation, particularly for medium to high water saturations. This could be related to the shape of the static capillary pressure curves which exhibit steeper slopes, particularly at high water saturations, as S_{wi} decreases.

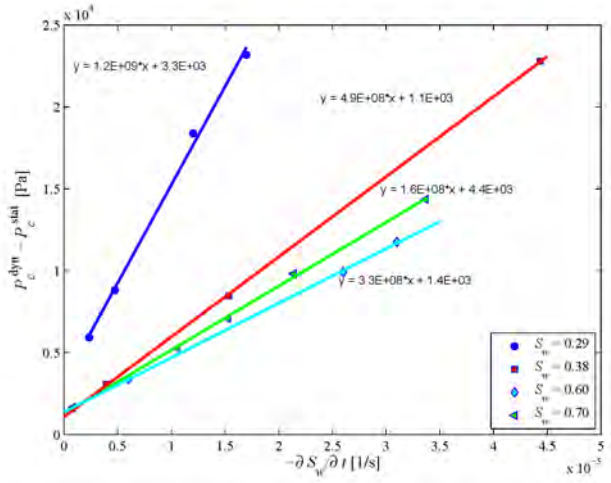

(a) Drainage processes at water-wet conditions.

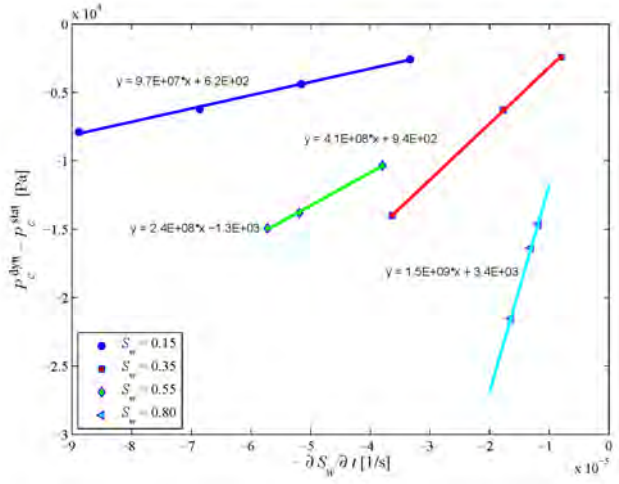

(b) Imbibition processes at mixed-wet conditions.

Figure 4.11: Difference between dynamic and static capillary pressure plotted as a function of the negative time derivative of water saturation at different pressure steps for several constant water saturations. The data are obtained from the dynamic simulations during (a) drainage at water-wet conditions and (b) imbibition at mixed-wet conditions. Straight lines are fitted to the simulated data based on Eq. (3.35) and the resulting expressions are shown next to the corresponding data set.

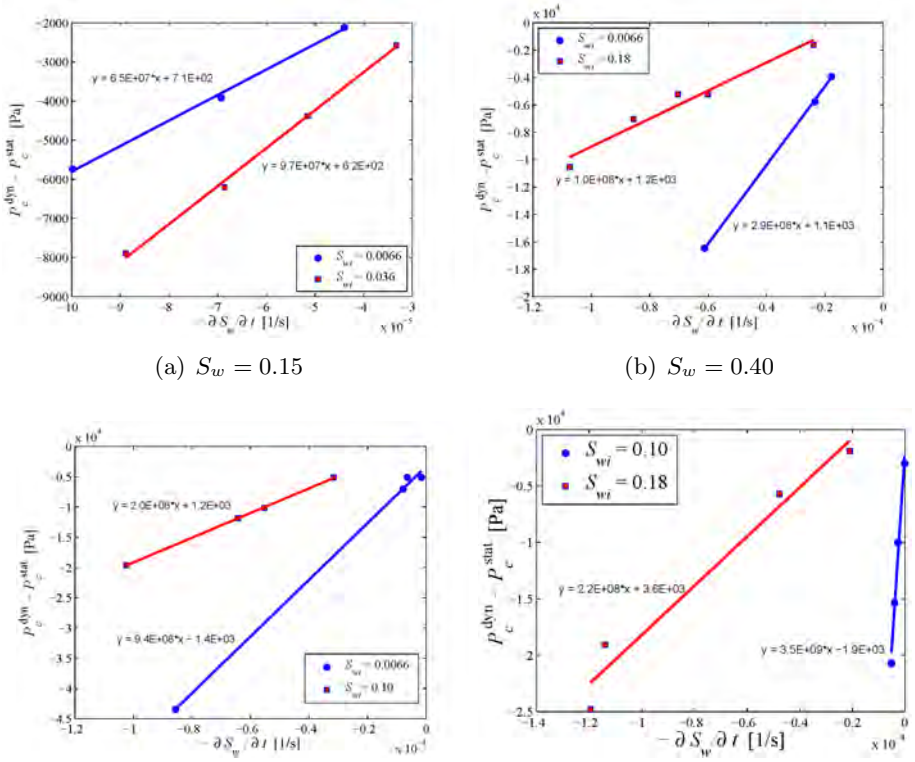

(a) $S_w = 0.15$ (b) $S_w = 0.40$

(c) $S_w = 0.68$ (d) $S_w = 0.87$

Figure 4.12: Difference between dynamic and static capillary pressure plotted as a function of the negative time derivative of water saturation at different pressure steps for constant water saturations S_w and S_{wi}. The data are obtained from the dynamic imbibition simulations at mixed-wet conditions established at four different initial water saturations. Straight line are fitted to the simulated data based on Eq. (3.35) and the resulting expressions are shown next to the corresponding data set.

4.4 Three-phase fluid configurations and capillary pressure curves

For the numerical results presented in this section, the fluid/fluid interfacial tensions in the spreading system ($C_{S,o}$ = 0 N/m) are given as σ_{go} = 0.01 N/m, σ_{ow} = 0.02 N/m and σ_{gw} = 0.03 N/m. In the non-spreading system ($C_{S,o}$ = -0.05 N/m), the corresponding values are σ_{go} = 0.01 N/m, σ_{ow} = 0.02 N/m and σ_{gw} = 0.025 N/m. The oil-water contact angles considered are $\theta_{ow} = 0^\circ$ and $\theta_{ow} = 40^\circ$, which represent a strongly water-wet and a weaker water-wet system, respectively, and the corresponding gas-oil and gas-water contact angles are computed from Eqs. (3.4) and (3.5).

4.4.1 Three-phase capillary entry pressure radii

The three-phase gas-oil capillary entry radii in more than 50 Betheim sandstone pore geometries at uniformly-wet conditions are computed from Eqs. (3.20) and (3.21) for both spreading and non-spreading systems, and the simulated results are shown in Figure 4.13. In this figure, the dimensionless gas-oil capillary entry radii (defined as the ratio of gas-oil capillary entry radius $r_{go,E}$ to oil-water capillary entry radius $r_{ow,E}$) are plotted as a function of dimensionless oil-water radii (defined as the ratio of oil-water radius r_{ow} to oil-water capillary entry radius $r_{ow,E}$).

The results presented in Figure 4.13(a) for the spreading system show that for a given wetting condition, the dimensionless gas-oil capillary entry radius, $\frac{r_{go,E}}{r_{ow,E}}$ increases as r_{ow} decreases down to $r_{ow,E}$. In this oil-water radius range, gas invades water-filled pore geometries. For $\frac{r_{ow}}{r_{ow,E}} < 1$, gas invades pore geometries occupied by both oil and water, and $\frac{r_{go,E}}{r_{ow,E}}$ reaches an approximately constant value that depends on the contact angles, indicating that the major part of the data in this radius range represents two-phase gas-oil displacements with oil layer formation.

In the non-spreading system, the behavior of gas-oil capillary entry radii

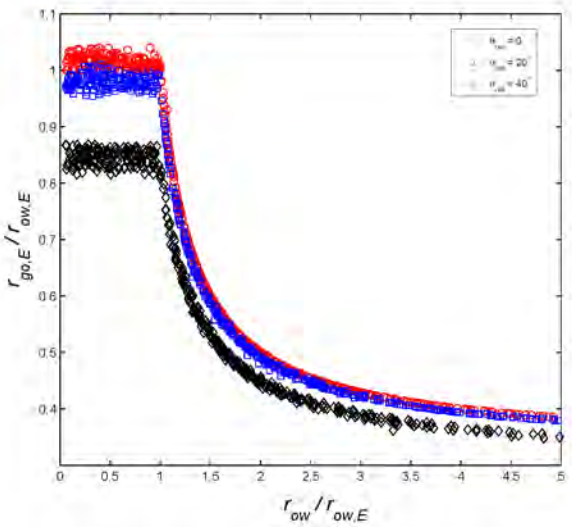

(a) Spreading system.

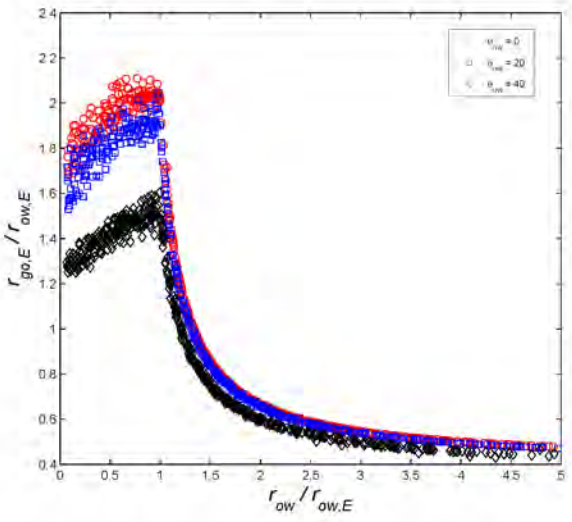

(b) Non-spreading system.

Figure 4.13: Numerically determined gas-oil dimensionless capillary entry radii for (a) spreading and (b) non-spreading systems; red circles: $\theta_{ow} = 0°$, blue squares: $\theta_{ow} = 20°$, black diamonds: $\theta_{ow} = 40°$.

is similar to that of a spreading system when $\frac{r_{ow}}{r_{ow,E}} > 1$ (refer to Figure 4.13(b)). The difference in the behavior of the normalized $\frac{r_{go,E}}{r_{ow,E}}$ in the two systems occurs for $\frac{r_{ow}}{r_{ow,E}} < 1$. For the non-spreading system, $\frac{r_{go,E}}{r_{ow,E}}$ is larger due to the larger gas-oil contact angles. In addition, the value of $\frac{r_{go,E}}{r_{ow,E}}$ decreases continuously for decreasing $\frac{r_{ow}}{r_{ow,E}} < 1$, which indicates that in this region three-phase displacement occur, in which gas displaces both oil and water while few oil layers form.

Figure 4.13 demonstrates that the gas-oil capillary entry pressure depends strongly on the existing oil/water configurations in the pore space. Generally, the presence of an oil phase lowers the gas entry pressure, indicating that for the CO_2 geological storage, CO_2 is stored more safely below low-permeable formation layers in subsurface aquifers than in depleted oil reservoirs. The same results were also observed recently in the lab with the use of micro-model experiments (Gauteplass et al., 2013).

4.4.2 Three-phase fluid configurations

Gas invasion processes at constant oil-water capillary pressures are simulated in the main image of Bentheim sandstone. Figure 4.14 shows for one of these gas invasion processes the three-phase (gas, oil and water) fluid distributions at chosen gas-oil capillary pressures in the strongly water-wet spreading system. The initial oil-water configuration is shown in Figure 4.14(a). The three-phase configurations show that a larger number of oil layers exist during the low gas-oil capillary pressure stage; this is in agreement with the micro-CT imaging results of three-phase distributions of gas, oil and water in Bentheim sandstone presented by Feali et al. (2012). Contrary to the non-spreading system, spreading oil layers exist even at higher gas-oil capillary pressures if the oil-water capillary pressure is sufficiently large.

Figure 4.15 shows the three-phase (gas, oil and water) fluid distributions at selected gas-oil capillary pressures for a gas invasion process carried out in the strongly water-wet non-spreading system. Fewer oil layers are

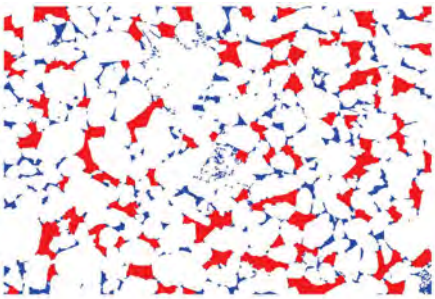

(a) Initial oil-water configurations

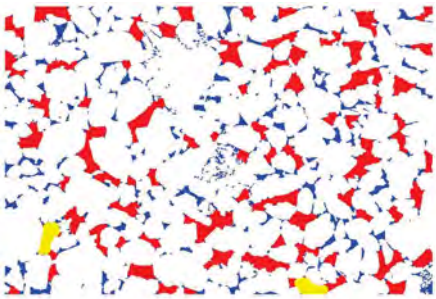

(b) $P_{cgo} = 4.26 \times 10^3$ Pa ($r_{go} = 11.5$ pixel lengths)

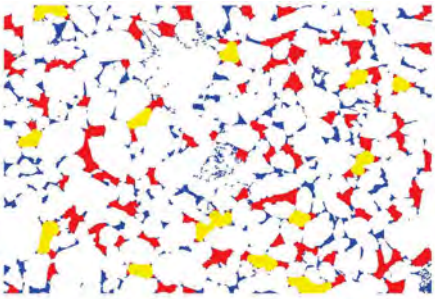

(c) $P_{cgo} = 4.90 \times 10^3$ Pa ($r_{go} = 10$ pixel lengths)

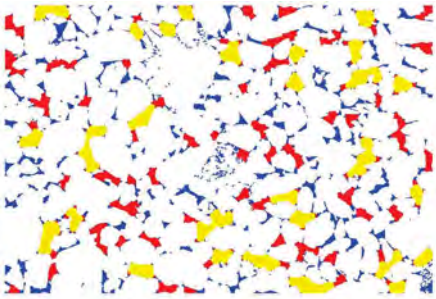

(d) $P_{cgo} = 6.13 \times 10^3$ Pa ($r_{go} = 8$ pixel lengths)

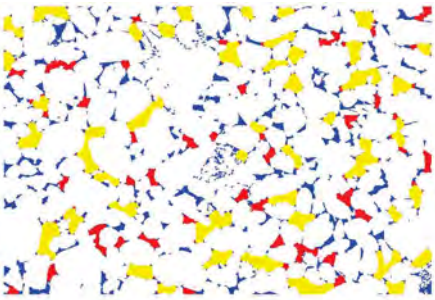

(e) $P_{cgo} = 7.54 \times 10^3$ Pa ($r_{go} = 6.5$ pixel lengths)

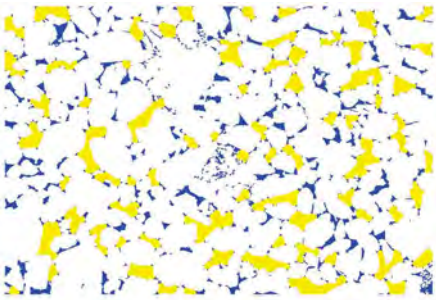

(f) $P_{cgo} = 9.80 \times 10^3$ Pa ($r_{go} = 5$ pixel lengths)

Figure 4.14: Three phase fluid configurations at selected gas-oil capillary pressures during gas invasion simulated with a constant oil-water capillary pressure, $P_{cow} = 1.9608 \times 10^4$ Pa ($r_{ow} = 5$ pixel lengths), in a strongly water-wet, spreading system (yellow: gas; red: oil; blue: water).

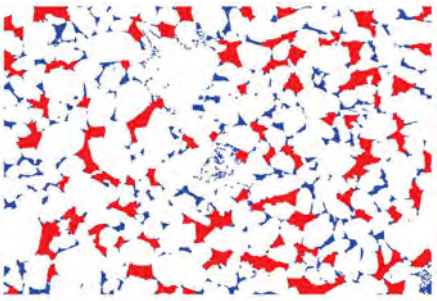

(a) Initial oil-water configurations

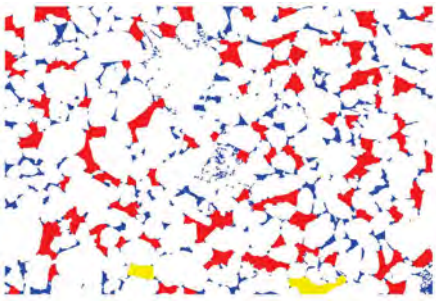

(b) $P_{cgo} = 2.39 \times 10^3$ Pa ($r_{go} = 20.5$ pixel lengths)

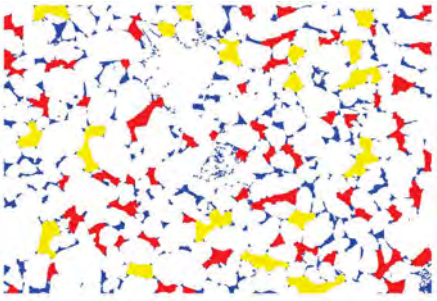

(c) $P_{cgo} = 2.72 \times 10^3$ Pa ($r_{go} = 18$ pixel lengths)

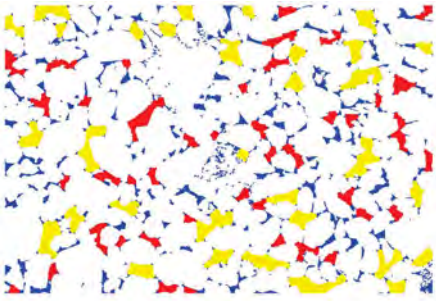

(d) $P_{cgo} = 3.50 \times 10^3$ Pa ($r_{go} = 14$ pixel lengths)

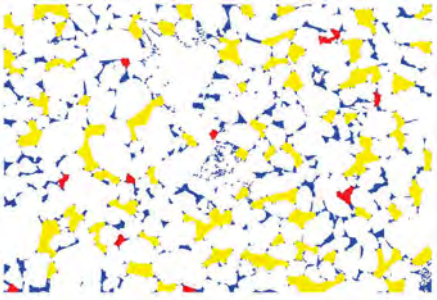

(e) $P_{cgo} = 4.46 \times 10^3$ Pa ($r_{go} = 11$ pixel lengths)

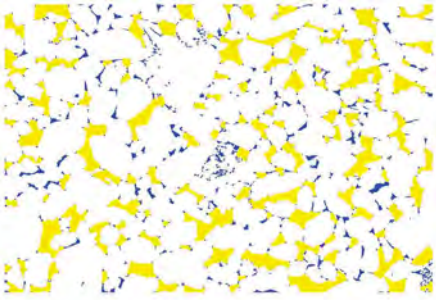

(f) $P_{cgo} = 1.96 \times 10^4$ Pa ($r_{go} = 2.5$ pixel lengths)

Figure 4.15: Three phase fluid configurations at selected gas-oil capillary pressures during gas invasion simulated with a constant oil-water capillary pressure, $P_{cow} = 1.9608 \times 10^4$ Pa ($r_{ow} = 5$ pixel lengths), in a strongly water-wet, non-spreading system (yellow: gas; red: oil; blue: water).

observed in this case as compared to the spreading system. However, Figures 4.15(c)- 4.15(d) show that some oil layers do exist between bulk gas and corner water and that the gas-oil interfaces are relatively flat; these findings are in agreement with the fluid distributions observed by (Feali et al., 2012) in Bentheim sandstone using micro-CT imaging techniques. In the non-spreading system, gas invades preferentially first the larger pores that are occupied by oil in the pore centers and water in the pore corners. Gas displaces all the oil, while gas-water AMs form in the pore corners and constrictions. Oil layer formation is, in most cases, prohibited due to the larger gas-oil contact angle in the strongly water-wet, non-spreading system.

4.4.3 Three-phase capillary pressure curves

The simulated gas-oil capillary pressure curves in the main image of Bentheim sandstone are shown in Figure 4.16 for all the gas invasion processes, initiated at different constant oil-water capillary pressures, and performed for spreading and non-spreading systems at strongly and weakly water-wet conditions. This figure shows that the gas-oil capillary pressure curves collapse to an almost unique curve as a function of the total liquid saturation int eh major part of the three-phase region, and therefore the gas-oil capillary pressure can be approximated by a function of gas saturation only. However, at small to intermediate gas saturations in the non-spreading systems, the simulated gas-oil capillary pressure curves are located within a narrow band (see for example Figure 4.16(c) and Figure 4.16(d)). This behavior is attributed to the formation of gas-water interfaces when gas invades pore spaces which are saturated with both oil and water. Hence, the presence of water in the pore corners, as well as the initial oil-water capillary pressure, affects the gas-oil capillary entry pressure. Such a three-phase displacement is associated with a different capillary entry pressure than the one required for the oil layer formation process in which gas displaces only oil at a two-phase gas-oil capillary entry pressure. The presence of corner water may also change

the invasion order of the pore spaces compared to the two-phase gas-oil displacements.

At low oil saturations, the simulated three-phase gas-oil capillary pressure depends strongly on tow saturations. This changed behavior occurs because gas has started to invade water-filled pores while oil still exists in the medium. For the non-spreading systems, the oil is located in a few small pore areas at small oil saturations, and gas invasion results in formation of gas-water interfaces as described in Figure 4.16(c) and Figure 4.16(d). However, it is for the weakly water-wet spreading system this changed saturation dependency of the gas-oil capillary pressure is most significant, as shown in Figure 4.16(b). In this case oil layer formation occurs most frequently, and thin oil layers are observed to remain present at very small oil saturations even after gas has started to invade pores occupied by water, leading to the non-unique gas-oil capillary pressure curves in the small oil saturation range as shown in Figure 4.16(b).

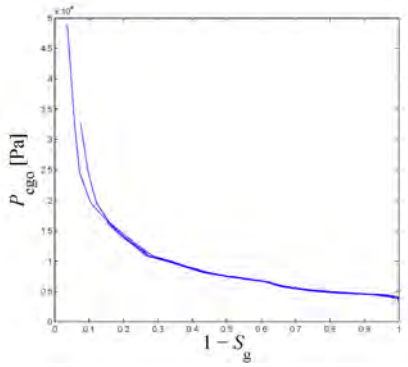

(a) Strongly water-wet spreading system

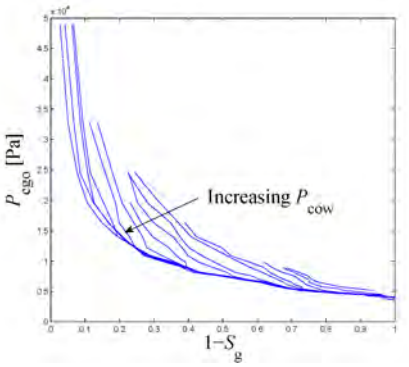

(b) Weakly water-wet spreading system

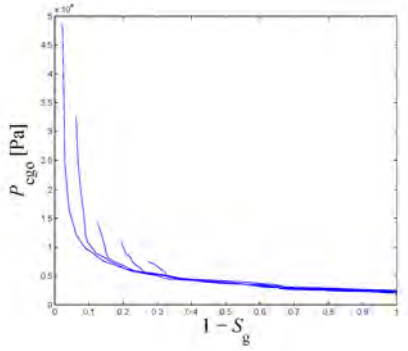

(c) Strongly water-wet non-spreading system

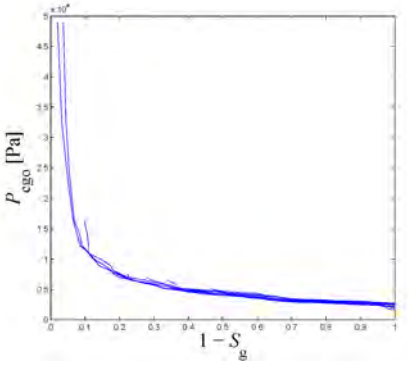

(d) Weakly water-wet non-spreading system

Figure 4.16: Three-phase gas-oil capillary pressure curves as a function of gas saturation for different constant oil-water capillary pressures.

Chapter 5

Conclusions and Future Work

5.1 Conclusions

Two- and three-phase capillary pressure curves and fluid configurations were simulated in high resolution segmented 2D rock images by developing further a combinatorial, semi-analytical method. The simulated capillary pressure and associated fluid-configuration conductances were adopted as input for the interacting tube bundle model to simulate the two-phase saturation profile development under capillary-viscous force dominated flow conditions. Dynamic effects in capillary pressure curves were investigated with the extended interacting tube bundle model and a proper phase averaging algorithm. The conclusions of this work are summarized as follows:

- The level of computed capillary pressure curves for uniformly water-wet conditions depends on the contact angle of the fluid/solid surfaces, and the traditional J-function is capable of scaling the wettability effects in the simulated capillary pressure curves.

- Computed capillary pressure curves and corresponding fluid configurations depend strongly on wettability and initial water saturation for mixed-wet conditions. Generally, capillary pressure curves obtained in systems with larger contact angles and smaller initial water saturations at the end of drainage exhibit more oil-wet behavior.

- An improved J-function for mixed-wet conditions is developed to describe more accurately the variability of formation wettability in reservoir simulation models; the proposed J-function works satisfactorily for measured imbibition capillary pressure curves in sandstone mixed-wet conditions.

- Non-wetting phase (e.g., CO_2) entry pressures are (a) strongly affected by the presence of a third intermediate-wet phase (e.g., oil) in the pore space and (b) strongly dependent on the existing initial fluid (e.g., oil/water) configuration existing in the pore space. Generally, the presence of an oil phase lowers the CO_2 entry pressure at water-wet conditions, indicating that CO_2 is stored more safely below low-permeable formation layers in subsurface aquifers than in depleted oil reservoirs.

- The computed three-phase fluid configurations exhibit the same trends as recently published experimental fluid configurations that are obtained from micro-CT imaging in Bentheim sandstone. Generally, spreading systems clearly display oil-layer behavior, especially in a high oil-water capillary pressure state. Non-spreading systems have fewer oil layers, while some thick oil layers exist when the gas-oil capillary pressure is relatively low.

- The gas-oil capillary pressure at water-wet conditions seems to be described well as a function of only the gas saturation in the major part of the three-phase region, despite three-phase displacements in which gas displaces both oil and water occur frequently in individual pore geometries for the non-spreading systems. At small oil

saturations, the gas-oil capillary pressure depends strongly on two saturations, which is particularly visible in the results for the weakly water-wet spreading system because thin oil layers exist after gas has started to invade pores occupied by water only.

- The simulated saturation profiles at mixed-wet conditions, exhibit an increasingly gradual behavior with time as the contact angle defined on the oil-wet solid surfaces increases or the initial water saturation decreases. Steep Buckley-Leverett profiles were observed for high flow rates at larger initial water saturations and smaller contact angles defined on the oil-wet solid surfaces.

- In the interacting tube bundle model, front menisci associated with positive capillary pressures promote oil displacement by water, whereas for large and negative capillary pressures at small flow rates oil displaces water because the associated front menisci retract. This results in the development of pronounced gradual saturation fronts at mixed-wet conditions.

- Simulated dynamic capillary pressure curves are located at a higher capillary level than the corresponding static curve for drainage, whereas for imbibition the dynamic curve is located at a lower capillary level than the corresponding static curve, regardless the porous medium wetting condition. The difference becomes larger as the pressure step applied in the simulations is increased.

- The simulation obtained dynamic capillary coefficient is a function of saturation and appears bo be independent of the incremental pressure step, which is consistent with the results reported in previous studies.

- For imbibition, the main trend is that the dynamic capillary coefficient increases with decreasing water saturations at water-wet conditions, whereas for mixed- to oil-wet conditions the dynamic coefficient increases with increasing water saturation. Imbibition

processes simulated at mixed- to oil-wet conditions indicate that the dynamic capillary coefficient increases with decreasing initial water saturation.

5.2 Future work

The following recommendations for future work are suggested:

- Improve the current mixed-wet model, which is based on the work of Kovscek et al. (1993), to include a transition zone near the contact line, as deposition of crude oil components is observed to occur non-uniformly and reaching a plateau at a finite distance outside of the remaining bulk water phase, as reported by Kumar & Fogden (2010).

- Extend the semi-analytical model to simulate three-phase capillary pressure and associated fluid configurations in mixed-wet complex pore spaces and formulate physically-based capillary pressure correlations based on simulated results.

- Extend the models to account for phase entrapment. This can be done by constructing a pore-network model and utilize complex pore geometries from segmented SEM images as throat cross-sections. Another possibility is to use SEM images from different cross-sections along the core and implemented sound rules for pore interconnectivity between the different sections (Wang & Dong, 2011). A third possibility is to account for these features by introducing correction parameters in the simulated results performed with the present model (Virnovsky et al., 2009).

- Perform quantitative comparisons between the results obtained from interacting tube bundle model with water flooding experimental results in core samples.

- Formulate physically-sound correlations for dynamic capillary coefficient for various wettabilities and initial water saturations for reservoir simulation.
- Apply the developed modeling procedures to segmented SEM images of other rock materials, such as carbonates, including chalk.

References

Adler, P. M., Jacquin, C. G., & Thovert, J. F. (1992). The formation factor of reconstructed porous media. *Water Resources Research*, *28*, 1571–1576.

Ahrenholz, B., Tölke, J., & Krafczyk, M. (2006). Lattice-Boltzmann simulations in reconstructed parametrized porous media. *International Journal of Computational Fluid Dynamics*, *20*, 369–377.

Ahrenholz, B., Tölke, J., Lehmann, P., Peters, A., Kaestner, A., Krafczyk, M., & Durner, W. (2008). Prediction of capillary hysteresis in a porous material using Lattice-Boltzmann methods and comparison to experimental data and a morphological pore network model. *Advances in Water Resources*, *31*, 1151 – 1173.

Akhlaghi Amiri, H., & Hamouda, A. (2013). Evaluation of level set and phase field methods in modeling two phase flow with viscosity contrast through dual-permeability porous medium. *International Journal of Multiphase Flow*, *52*, 22 – 34.

Al-Dhahli, A. R. S., Geiger, S., & van Dijke, M. I. J. (2013). Three-phase pore-network modeling for reservoirs with arbitrary wettability. *SPE Journal*, *18*, 285–295.

Al-Futaisi, A., & Patzek, T. W. (2003). Extension of Hoshen-Kopelman algorithm to non-lattice environments. *Physica A: Statistical Mechanics and its Applications*, *321*, 665 – 678.

Al-Kharusi, A. S., & Blunt, M. J. (2007). Network extraction from sandstone and carbonate pore space images. *Journal of Petroleum Science and Engineering*, *56*, 219 – 231.

Anderson, W. G. (1986). Wettability literature survey - Part 1: Rock/oil/brine interactions and the effects of core handling on wettability. *Journal of Petroleum Technology*, *38*, 1125–1144.

Anderson, W. G. (1987). Wettability literature survey - Part 4: Effects of wettability on capillary pressure. *Journal of Petroleum Technology*, *39*, 1283–1300.

Baker, L. E. (1998). Three-phase relative permeability correlations, paper SPE 17639. In *Proc. of the SPE/DOE Enhanced Oil Recovery Symposium, Tulsa, OK, April 17-20*.

Bandara, U. C., Tartakovsky, A. M., & Palmer, B. J. (2011). Pore-scale study of capillary trapping mechanism during CO_2 injection in geological formations. *International Journal of Greenhouse Gas Control*, *5*, 1566 – 1577.

Barenblatt, G., & Vinnichenko, A. P. (1980). Non-equilibrium seepage of immiscible fluids. *Adv. Mech*, *3*, 35–50.

Berg, S., Ott, H., Klapp, S., Schwing, A., Neiteler, R., Brussee, N., Makurat, A., L.Leu, Enzmann, F., Schwarz, J., Kersten, M., Irvine, S., & Stampanoni, M. (2013). Real-time 3D imaging of haines jumps in porous media flow. *Proc. Natl. Acad. Sci. U S A*, *110*, 3755–3759.

Blunt, M., & King, P. (1991). Relative permeabilities from two- and three-dimensional pore-scale network modelling. *Transport in Porous Media*, *6*, 407–433.

Blunt, M. J. (1997a). Physically-based network modeling of multiphase flow in intermediate-wet porous media. *Journal of Petroleum Science and Engineering*, *20*, 111–125.

Blunt, M. J. (1997b). Pore level modeling of the effects of wettability. *SPE Journal*, *2*, 494–510.

Blunt, M. J. (2001). Flow in porous media - pore-network models and multiphase flow. *Current Opinion in Colloid and Interface Science*, *6*, 197–207.

Blunt, M. J., Bijeljic, B., Dong, H., Gharbi, O., Iglauer, S., Mostaghimi, P., Paluszny, A., & Pentland, C. (2013). Pore-scale imaging and modelling. *Advances in Water Resources*, *51*, 197 – 216.

Blunt, M. J., & Scher, H. (1995). Pore-level modeling of wetting. *Phys. Rev. E*, *52*, 6387–6403.

Boek, E. S., & Venturoli, M. (2010). Lattice-Boltzmann studies of fluid flow in porous media with realistic rock geometries. *Computers and Mathematics with Applications*, *59*, 2305 – 2314.

Bottero, S., Hassanizadeh, S. M., Kleingeld, P. J., & Bezuijen, A. (2006). Experimental study of dynamic capillary pressure effect in two-phase flow in porous media. In *Proceedings of the XVI International Conference on Computational Methods in Water Resources (CMWR 2006)*. Copenhagen, Denmark.

Bottero, S., Hassanizadeh, S. M., Kleingeld, P. J., & Heimovaara, T. J. (2011). Nonequilibrium capillarity effects in two-phase flow through porous media at different scales. *Water Resources Research*, *47*, 2011WR010887.

Bradford, S. A., & Leij, F. J. (1995). Fractional wettability effects on two-and three-fluid capillary pressure-saturation relations. *Journal of Contaminant Hydrology*, *20*, 89–109.

Bradford, S. A., & Leij, F. J. (1996). Predicting two- and three-fluid capillary pressure-saturation relationships of porous media with fractional wettability. *Water Resources Research*, *32*, 251–259.

Braquelaire, J.-P., & Vialard, A. (1999). Euclidean paths: A new representation of boundary of discrete regions. *Graphical Models and Image Processing*, *61*, 16 – 43.

Brooks, R. H., & Corey, A. T. (1964). Hydraulic properties of porous media. *Hydrology Papers from Colorado State University*, *3*, 1–27.

Bryant, S. L., King, P. R., & Mellor, D. W. (1993a). Network model evaluation of permeability and spatial correlation in a real random sphere packing. *Transport in Porous Media*, *11*, 53–70.

Bryant, S. L., Mellor, D. W., & Cade, C. A. (1993b). Physically representative network models of transport in porous media. *AIChE Journal*, *39*, 387–396.

Cahn, J. W., & Hilliard, J. E. (1958). Free energy of a nonuniform system. I. interfacial free energy. *The Journal of Chemical Physics*, *28*, 258–267.

Camps-Roach, G., O'Carroll, D. M., Newson, T. A., Sakaki, T., & Illangasekare, T. H. (2010). Experimental investigation of dynamic effects in capillary pressure: Grain size dependency and upscaling. *Water Resources Research*, *46*, 2009WR008881.

Cassie, A. B. D., & Baxter, S. (1944). Wettability and porous surfaces. *Transactions of the Faraday Society*, *40*, 546–551.

Class, H., Ebigbo, A., Helmig, R., Dahle, H., Nordbotten, J., Celia, M., Audigane, P., Darcis, M., Ennis-King, J., Fan, Y., Flemisch, B., Gasda, S., Jin, M., Krug, S., Labregere, D., Naderi Beni, A., Pawar, R., Sbai, A., Thomas, S., Trenty, L., & Wei, L. (2009). A benchmark study on problems related to CO_2 storage in geologic formations. *Computational Geosciences*, *13*, 409–434.

Cuiec, L. E. (1991). Evaluation of reservoir wettability and its effect on oil recovery. In N. R. Morrow (Ed.), *Interfacial Phenomena in Petrolem Recovery* (pp. 319–375). New York and Basel, Marcel Dekker, Inc.

Dahle, H., & Celia, M. (1999). A dynamic network model for two-phase immiscible flow. *Computational Geosciences*, *3*, 1–22.

Dahle, H., Celia, M., & Hassanizadeh, S. M. (2005). Bundle-of-tubes model for calculating dynamic effects in the capillary-pressure-saturation relationship. In D. Das, & S. Hassanizadeh (Eds.), *Upscaling Multiphase Flow in Porous Media* (pp. 5–22). Springer Netherlands.

Dandekar, A. Y. (2006). *Petroleum reservoir rock and fluid properties*. Taylor & Francis, Boca Raton, Fla.

Das, D. B., & Mirzaei, M. (2012). Dynamic effects in capillary pressure relationships for two-phase flow in porous media: Experiments and numerical analyses. *AIChE Journal*, *58*, 3891–3903.

Diamantopoulos, E., & Durner, W. (2012). Dynamic nonequilibrium of water flow in porous media: A review. *Vadose Zone Journal*, *11*.

Diaz, C., Chatzis, I., & Dullien, F. (1987). Simulation of capillary pressure curves using bond correlated site percolation on a simple cubic network. *Transport in Porous Media*, *2*, 215–240.

Donaldson, E., & Alam, W. (2008). *Wettability*. Gulf Publishing Company, Houston, Texas.

Dong, H., & Blunt, M. J. (2009). Pore-network extraction from micro-computerized-tomography images. *Phys. Rev. E*, *80*, 036307.

Dong, M., Dullien, F., Dai, L., & Li, D. (2005). Immiscible displacement in the interacting capillary bundle model part I. Development of interacting capillary bundle model. *Transport in Porous Media*, *59*, 1–18.

Dong, M., Dullien, F. A., & Chatzis, I. (1995). Imbibition of oil in film form over water present in edges of capillaries with an angular cross section. *Journal of Colloid and Interface Science*, *172*, 21 – 36.

Fatt, I. (1956). The network model of porous media i. capillary pressure characteristics. *Petroleum Transactions, AIME*, *207*.

Feali, M., Pinczewski, W., Cinar, Y., Arns, C., Arns, J., Senden, T., Francois, N., & Knackstedt, M. (2012). Qualitative and quantitative analyses of the three-phase distribution of oil, water, and gas in bentheimer sandstone by use of micro-ct imaging. *SPE Reservoir Evaluation & Engineering*, *15*, 706–711.

Fenwick, D. H., & Blunt, M. J. (1998). Three-dimensional modeling of three phase imbibition and drainage. *Advances in Water Resources*, *21*, 121–143.

Ferrari, A., & Lunati, I. (2013). Direct numerical simulations of interface dynamics to link capillary pressure and total surface energy. *Advances in Water Resources*, *57*, 19 – 31.

Frette, O. I., & Helland, J. O. (2010). A semi-analytical model for computation of capillary entry pressures and fluid configurations in uniformly-wet pore spaces from 2D rock images. *Advances in Water Resources*, *33*, 846–866.

Frette, O. I., Virnovsky, G., & Hildebrand-Habel, T. (2009). Modeling the stability of thin water film using SEM images. In *EUROPEC/EAGE Conference and Exhibition, 8-11 June 2009, Amsterdam, The Netherlands*. Amsterdam, The Netherlands.

Gauteplass, J., Follesø, H. N., Graue, A., Kovscek, A. R., & Fernø, M. A. (2013). Visualization of pore-level displacement mechanisms during co_2 injection and eor processes. In *IOR 2013 17th European Symposium on Improved Oil Recovery St. Petersburg, Russia, 16-18 April 2013*.

Glantz, R., & Hilpert, M. (2011). Capillary displacement in totally wetting and infinitely long right prisms. *Multiscale Modeling and Simulation*, *9*, 1765–1800.

Goel, G., & O'Carroll, D. M. (2011). Experimental investigation of nonequilibrium capillarity effects: Fluid viscosity effects. *Water Resources Research*, *47*, 2010WR009861.

Grate, J. W., Dehoff, K. J., Warner, M. G., Pittman, J. W., Wietsma, T. W., Zhang, C., & Oostrom, M. (2012). Correlation of oil-water and air-water contact angles of diverse silanized surfaces and relationship to fluid interfacial tensions. *Langmuir*, *28*, 7182–7188.

Haines, W. B. (1930). Studies in the physical properties of soil. V. the hysteresis effect in capillary properties, and the modes of moisture distribution associated therewith. *The Journal of Agricultural Science*, *20*, 97–116.

Hamon, G. (2000). Field-wide variations of wettability, paper SPE 63144. In *SPE Annual Technical Conference and Exhibition, 1-4 October 2000, Dallas, Texas, USA*.

Hanspal, N. S., & Das, D. B. (2012). Dynamic effects on capillary pressuresaturation relationships for two-phase porous flow: Implications of temperature. *AIChE Journal*, *58*, 1951–1965.

Hassanizadeh, S. M., Celia, M. A., & Dahle, H. K. (2002). Dynamic effect in the capillary pressuresaturation relationship and its impacts on unsaturated flow. *Vadose Zone Journal*, *1*, 38–57.

Hassanizadeh, S. M., & Gray, W. G. (1993). Thermodynamic basis of capillary pressure in porous media. *Water Resources Research*, *29*, 3389–3405.

Held, M. (2010). Analytical computation of arc menisci configuration under primary drainage in convex capillary cross sections. *Computational Geosciences*, *14*, 311–317.

Helland, J. O., & Frette, O. I. (2010). Computation of fluid configurations and capillary pressures in mixed-wet 2D pore spaces from rock

images. In *Proceedings of the XVIII International Conference on Water Resources*. Barcelona, Spain, June 21-24.

Helland, J. O., & Skjæveland, S. M. (2004). Three-phase capillary pressure correlation for mixed-wet reservoirs, paper SPE 92057. In *SPE International Petroleum Conference in Mexico*. Puebla Pue., Mexico.

Helland, J. O., & Skjæveland, S. M. (2006a). Physically-based capillary pressure correlation for mixed-wet reservoirs from a bundle-of-tubes model. *SPE Journal*, *11*, 171–180.

Helland, J. O., & Skjæveland, S. M. (2006b). Three-phase mixed-wet capillary pressure curves from a bundle of triangular tubes model. *Journal of Petroleum Science and Engineering*, *52*, 100–130.

Hiorth, A., Jettestuen, E., Cathles, L., & Madland, M. (2013). Precipitation, dissolution, and ion exchange processes coupled with a Lattice Boltzmann advection diffusion solver. *Geochimica et Cosmochimica Acta*, *104*, 99 – 110.

Hirasaki, G. (1991a). Shape of meniscus/film transition region. In N. R. Morrow (Ed.), *Interfacial Phenomena in Petrolem Recovery* (pp. 77–99). New York and Basel, Marcel Dekker, Inc.

Hirasaki, G. (1991b). Thermodynamics of thin film and three-phase contact regions. In N. R. Morrow (Ed.), *Interfacial Phenomena in Petrolem Recovery* (pp. 23–76). New York and Basel, Marcel Dekker, Inc.

Hirt, C., & Nichols, B. (1981). Volume of fluid (VoF) method for the dynamics of free boundaries. *Journal of Computational Physics*, *39*, 201 – 225.

Hu, X. Y., & Adams, N. (2006). A multi-phase SPH method for macroscopic and mesoscopic flows. *Journal of Computational Physics*, *213*, 844 – 861.

Hughes, R., & Blunt, M. (2000). Pore scale modeling of rate effects in imbibition. *Transport in Porous Media*, *40*, 295–322.

Hui, M., & Blunt, M. J. (2000). Effects of wettability on three-phase flow in porous media. *J. Phys. Chem. B*, *104*, 3833–3845.

Jacqmin, D. (1999). Calculation of two-phase navierstokes flows using phase-field modeling. *Journal of Computational Physics*, *155*, 96 – 127.

Jadhunandan, P. P., & Morrow, N. R. (1995). Effect of wettability on waterflood recovery for crude-oil/brine/rock systems. *SPE Reservoir Eng.*, *10*, 40–46.

Jettestuen, E., Helland, J. O., & Prodanović, M. (2013). A level set method for simulating capillary-controlled displacements at the pore scale with nonzero contact angles. *Water Resources Research*, wrcr.20334.

Jiang, Z., van Dijke, M., Sorbie, K., & Couples, G. (2013). Representation of multi-scale heterogeneity via multi-scale pore networks. *Water Resources Research*, (p. wrcr.20304).

Jiang, Z., Dijke, M., Wu, K., Couples, G., Sorbie, K., & Ma, J. (2012). Stochastic pore network generation from 3D rock images. *Transport in Porous Media*, *94*, 571–593.

Joekar-Niasar, V., van Dijke, M., & Hassanizadeh, S. (2012). Pore-scale modeling of multiphase flow and transport: Achievements and perspectives. *Transport in Porous Media*, *94*, 461–464.

Joekar-Niasar, V., & Hassanizadeh, S. M. (2011). Effect of fluids properties on non-equilibrium capillarity effects: Dynamic pore-network modeling. *International Journal of Multiphase Flow*, *37*, 198–214.

Joekar-Niasar, V., & Hassanizadeh, S. M. (2012). Analysis of fundamentals of two-phase flow in porous media using dynamic pore-network

models: A review. *Critical Reviews in Environmental Science and Technology*, *42*, 1895–1976.

Joekar-Niasar, V., Hassanizadeh, S. M., & Dahle, H. K. (2010). Non-equilibrium effects in capillarity and interfacial area in two-phase flow: dynamic pore-network modelling. *Journal of Fluid Mechanics*, *655*, 38–71.

Juanes, R., MacMinn, C. W., & Szulczewski, M. L. (2010). The footprint of the CO_2 plume during carbon dioxide storage in saline aquifers: Storage efficiency for capillary trapping at the basin scale. *Transport in Porous Media*, *82*, 19–30.

Kalaydjian, F. (1992). Dynamic capillary pressure curve for water/oil displacement in porous media: Theory vs. experiment, paper SPE 24813. In *67th SPE Annual Technical Conference and Exhibition, Washington, DC. USA*.

Kaminsky, R., & Radke, C. (1997). Asphaltenes, water films, and wettability reversal. *SPE Journal*, *2*, 485–493.

Keller, A., Blunt, M., & Roberts, A. (1997). Micromodel observation of the role of oil layers in three-phase flow. *Transport in Porous Media*, *26*, 277–297.

Kim, D., & Lindquist, W. B. (2012). A semianalytic model for the computation of imbibition through polygonal cross sections. *Water Resources Research*, *48*, 2011WR011111.

Kordilla, J., Tartakovsky, A., & Geyer, T. (2013). A smoothed particle hydrodynamics model for droplet and film flow on smooth and rough fracture surfaces. *Advances in Water Resources*, *59*, 1–14.

Korteland, S., Bottero, S., Hassanizadeh, S., & Berentsen, C. (2010). What is the correct definition of average pressure? *Transport in Porous Media*, *84*, 153–175.

Kovscek, A. R., Wong, H., & Radke, C. J. (1993). A pore-level scenario for the development of mixed wettability in oil reservoirs. *AIChE Journal*, *39*, 1072–1085.

Kumar, M., & Fogden, A. (2010). Patterned wettability of oil and water in porous media. *Langmuir*, *26*, 4036–4047. PMID: 19916532.

Kumar, M., Fogden, A., Tim, S., & Knackstedt, M. A. (2012). Investigation of pore-scale mixed wettability. *SPE Journal*, *17*, 20–30.

Kumar, M., Senden, T., Latham, M. A. K. S., Sok, R., Sheppard, A., Turner, M. L., & Pinczewski, V. (2009). Imaging of pore scale distribution of fluid and wettability. *Petrophysics*, *50*, 311–321.

Lago, M., & Araujo, M. (2001). Threshold pressure in capillaries with polygonal cross section. *Journal of Colloid and Interface Science*, *243*, 219–226.

Lago, M., & Araujo, M. (2003). Threshold capillary pressure in capillaries with curved sides. *Physica A: Statistical Mechanics and its Applications*, *319*, 175–187.

Legait, B. (1983). Laminar flow of two phases through a capillary tube with variable square cross-section. *Journal of Colloid and Interface Science*, *96*, 28–38.

Lenhard, R. J., & Parker, J. C. (1988). Experimental validation of the theory of extending two-phase saturation-pressure relations to three-phase systems for monotonic drainage paths. *Water Resources Research*, *24*, 373–380.

Lenormand, R., Zarcone, C., & Sarr, A. (1983). Mechanisms of the displacement of one fluid by another in a network of capillary ducts. *Journal of Fluid Mechanics*, *135*, 337–353.

Leverett, M. C. (1941). *Capillary behavior in porous solids*. Trans. AIME 142.

Li, S., Dong, M., Li, Z., Huang, S., Qing, H., & Nickel, E. (2005). Gas breakthrough pressure for hydrocarbon reservoir seal rocks: implications for the security of long-term CO_2 storage in the Weyburn field. *Geofluids*, *5*, 326–334.

Lindquist, W., & Venkatarangan, A. (1999). Investigating 3D geometry of porous media from high resolution images. *Physics and Chemistry of the Earth, Part A: Solid Earth and Geodesy*, *24*, 593 – 599.

Lindquist, W. B. (2006). The geometry of primary drainage. *Journal of Colloid and Interface Science*, *296*, 655–668.

Lomeland, F., & Ebeltoft, E. (2008). A new versatile capillary pressure correlation. In *Proc. of the International Symposium of the Society of Core Analysts*. Abu Dhabi, U.A.E.

Long, J., Hyder, M., Huang, R., & Chen, P. (2005). Thermodynamic modeling of contact angles on rough, heterogeneous surfaces. *Advances in Colloid and Interface Science*, *118*, 173 – 190.

Ma, S., Mason, G., & Morrow, N. R. (1996). Effect of contact angle on drainage and imbibition in regular polygonal tubes. *Colloids and Surfaces A – Physicochemical and Engineering Aspects*, *117*, 273–291.

MacMinn, C. W., & Juanes, R. (2009). Post-injection spreading and trapping of CO_2 in saline aquifers: impact of the plume shape at the end of injection. *Comput. Geosci.*, *13*, 483–491.

Måløy, K. J., Furuberg, L., Jens, F., & Jøssang, T. (1992). Dynamics of slow drainage in porous media. *Phys. Rev. Lett.*, *68*, 2161–2164.

Manwart, C., Aaltosalmi, U., Koponen, A., Hilfer, R., & Timonen, J. (2002). Lattice-Boltzmann and finite-difference simulations for the permeability for three-dimensional porous media. *Phys. Rev. E*, *66*, 016702.

Manz, B., Gladden, L. F., & Warren, P. B. (1999). Flow and dispersion in porous media: Lattice-boltzmann and nmr studies. *AIChE Journal*, *45*, 1845–1854.

Martys, N. S., & Chen, H. (1996). Simulation of multicomponent fluids in complex three-dimensional geometries by the lattice Boltzmann method. *Phys. Rev. E*, *53*, 743–750.

Masalmeh, S. K. (2003). The effect of wettability heterogeneity on capillary pressure and relative permeability. *Journal of Petroleum Science and Engineering*, *39*, 399 – 408.

Mason, G., & Morrow, N. R. (1984). Meniscus curvatures in capillaries of uniform cross-section. *J. Chem. Soc., Faraday Trans. 1*, *80*, 2375–2393.

Mason, G., & Morrow, N. R. (1991). Capillary behavior of a perfectly wetting liquid in irregular triangular tubes. *Journal of Colloid and Interface Science*, *141*, 262–274.

Mayer, R. P., & Stowe, R. A. (1965). Mercury porosimetry-breakthrough pressure for penetration between packed spheres. *Journal of Colloid Science*, *20*, 893–911.

Mehmani, Y., Sun, T., Balhoff, M., Eichhubl, P., & Bryant, S. (2012). Multiblock pore-scale modeling and upscaling of reactive transport: Application to carbon sequestration. *Transport in Porous Media*, *95*, 305–326.

Middleton, R. S., Keating, G. N., Stauffer, P. H., Jordan, A. B., Viswanathan, H. S., Kang, Q. J., Carey, J. W., Mulkey, M. L., Sullivan, E. J., Chu, S. P., Esposito, R., & Meckel, T. A. (2012). The cross-scale science of CO_2 capture and storage: from pore scale to regional scale. *Energy Environ. Sci.*, *5*, 7328–7345.

Mirzaei, M., & Das, D. B. (2007). Dynamic effects in capillary pressure-saturations relationships for two-phase flow in 3D porous media: Im-

plications of micro-heterogeneities. *Chemical Engineering Science*, *62*, 1927–1947.

Mirzaei, M., & Das, D. B. (2013). Experimental investigation of hysteretic dynamic effect in capillary pressure-saturation relationship for two-phase flow in porous media. *AIChE Journal*, *59*, 3958–3974.

Mohanty, K., Davis, H., & Scriven, L. (1987). Physics of oil entrapment in water-wet rock. *SPE Reservoir Engineering*, *2*, 113–128.

Morrow, N. R. (1970). Physics and thermodynamics of capillary action in porous media. *Industrial & Engineering Chemistry*, *62*, 32–56.

Morrow, N. R. (1990). Wettability and its effect on oil recovery. *Journal of Petroleum Technology*, *42*, 1476–1484.

Mostaghimi, P., Bijeljic, B., & Blunt, M. J. (2012). Simulation of flow and dispersion on pore-scale images. *SPE Journal*, *17*, 1131–1141.

Mousavi, M., Prodanović, M., & Jacobi, D. (2013). New classification of carbonate rocks for process-based pore-scale modeling. *SPE Journal*, *18*, 243–263.

Noaman, E. (1995). Development of a modified capillary pressure *j*-function. In *Middle East Oil Show*. Bahrain.

O'Carroll, D. M., Mumford, K. G., Abriola, L. M., & Gerhard, J. I. (2010). Influence of wettability variations on dynamic effects in capillary pressure. *Water Resources Research*, *46*, 2009WR008712.

Okabe, H., & Blunt, M. J. (2007). Pore space reconstruction of vuggy carbonates using microtomography and multiple-point statistics. *Water Resources Research*, *43*, 2006WR005680.

Øren, P., & Pinczewski, W. (1995). Fluid distribution and pore-scale displacement mechanisms in drainage dominated three-phase flow. *Transport in Porous Media*, *20*, 105–133.

Øren, P. E., & Bakke, S. (2002). Process based reconstruction of sandstones and prediction of transport properties. *Transport in Porous Media*, *46*, 311–343.

Øren, P. E., & Bakke, S. (2003). Reconstruction of berea sandstone and pore-scale modelling of wettability effects. *Journal of Petroleum Science and Engineering*, *39*, 177–199.

Øren, P. E., Bakke, S., & Arntzen, O. (1998). Extending predictive capabilities to network models. *SPE Journal*, *3*, 324–336.

Osher, S., & Fedkiw, R. (2003). *Level Set Methods and Dynamic Implicit Surfaces*. Springer.

Piri, M., & Blunt, M. J. (2004). Three-phase threshold capillary pressures in noncircular capillary tubes with different wettabilities including contact angle hysteresis. *Phys. Rev. E*, *70*, 061603.

Piri, M., & Blunt, M. J. (2005). Three-dimensional mixed-wet random pore-scale network modeling of two- and three-phase flow in porous media. *Phys. Rev. E*, *71*.

Porta, G., Chaynikov, S., Riva, M., & Guadagnini, A. (2013). Upscaling solute transport in porous media from the pore scale to dual- and multicontinuum formulations. *Water Resources Research*, (p. 10.1002/wrcr.20183).

Princen, H. (1969a). Capillary phenomena in assemblies of parallel cylinders: I. capillary rise between two cylinders. *Journal of Colloid and Interface Science*, *30*, 69–75.

Princen, H. (1969b). Capillary phenomena in assemblies of parallel cylinders: II. capillary rise in systems with more than two cylinders. *Journal of Colloid and Interface Science*, *30*, 359–371.

Princen, H. (1970). Capillary phenomena in assemblies of parallel cylinders: III. liquid columns between horizontal parallel cylinders. *Journal of Colloid and Interface Science*, *34*, 171–184.

Princen, H. M. (1992). Capillary pressure behavior in pores with curved triangular cross-section: Effect of wettability and pore size distribution. *Colloids and Surfaces*, *65*, 221–230.

Prodanović, M., & Bryant, S. L. (2006). A level set method for determining critical curvatures for drainage and imbibition. *Journal of Colloid and Interface Science*, *304*, 442 – 458.

Prodanović, M., Bryant, S. L., & Karpyn, Z. T. (2010). Investigating matrix/fracture transfer via a level set method for drainage and imbibition. *SPE Journal*, *15*, 125–136.

Quiblier, J. A. (1984). A new three-dimensional modeling technique for studying porous media. *Journal of Colloid and Interface Science*, *98*, 84 – 102.

Raeini, A. Q., Blunt, M. J., & Bijeljic, B. (2012). Modelling two-phase flow in porous media at the pore scale using the volume-of-fluid method. *Journal of Computational Physics*, *231*, 5653 – 5668.

Ramstad, T., Idowu, N., Nardi, C., & Øren, P. E. (2012). Relative permeability calculations from two-phase flow simulations directly on digital images of porous rocks. *Transport in Porous Media*, *94*.

Ramstad, T., Øren, P. E., & Bakke, S. (2010). Simulation of two-phase flow in reservoir rocks using a Lattice Boltzmann method. *SPE Journal*, *15*, 917–927.

Raoof, A., Nick, H., Wolterbeek, T., & Spiers, C. (2012). Pore-scale modeling of reactive transport in wellbore cement under CO_2 storage conditions. *International Journal of Greenhouse Gas Control*, *11, Supplement*, S67 – S77.

Roof, J. G. (1970). Snap-off of oil droplets in water-wet pores. *SPE Journal*, *10*, 85–90.

Ruth, D., & Bartley, J. (2002). A perfect-cross-flow model for two phase flow in porous media. In *Proc. of the International Symposium of the Society of Core Analysts*. San Antonio, Texas, USA.

Ryazanov, A., Dijke, M., & Sorbie, K. (2009). Two-phase pore-network modelling: Existence of oil layers during water invasion. *Transport in Porous Media*, *80*, 79–99.

Saadatpoor, E., Bryant, S., & Sepehrnoori, K. (2010). New trapping mechanism in carbon sequestration. *Transport in Porous Media*, *82*, 3–17.

Salathiel, R. A. (1973). Oil recovery by surface film drainage in mixed-wettability rocks. *Journal of Petroleum Technology*, *25*, 3–17.

Schembre, J., & Kovscek, A. (2006). Estimation of dynamic relative permeability and capillary pressure from countercurrent imbibition experiments. *Transport in Porous Media*, *65*, 31–51.

Sethian, J. A. (1999). *Level Set Methods and Fast Marching Methods*. Cambridge University Press.

Sheng, Q., Thompson, K., Fredrich, J. T., & Salino, P. A. (2011). Numerical prediction of relative permeability from microct images: Comparison of steady-state versus displacement methods, paper SPE 147431. In *SPE Annual Technical Conference and Exhibition, 30 October-2 November 2011, Denver, Colorado, USA*. Denver, Colorado, USA.

Silin, D., Ajo-Franklin, J., Helland, J. O., Jettestuen, E., & Hatzignation, D. G. (2012). *Pore-scale study of the impact of fracture and wettability on two-phase flow properties of rock*. Technical Report 5810E LBNL, 5810E.

Silin, D., Jin, G., & Patzek, T. (2003). Robust determination of pore space morphology in sedimentary rocks, paper SPE 84296. In *SPE Annual Technical Conference and Exhibition, 5-8 October 2003, Denver, Colorado*.

Silin, D., & Patzek, T. (2004). On Barenblatt's model of spontaneous countercurrent imbibition. *Transport in Porous Media*, *54*, 297–322.

Silin, D., & Patzek, T. (2006). Pore space morphology analysis using maximal inscribed spheres. *Physica A Statistical and Theoretical Physics*, *371*, 336–360.

Silin, D., Tomutsa, L., Benson, S., & Patzek, T. (2011). Microtomography and pore-scale modeling of two-phase fluid distribution. *Transport in Porous Media*, *86*, 495–515.

Skjæveland, S. M., Siqveland, L. M., Kjosavik, A., Hammervold, W. L., & Virnovsky, G. A. (1998). Capillary pressure correlation for mixed-wet reservoirs, paper SPE 39497. In *SPE India Oil and Gas Conference and Exhibition*. New Delhi, India.

Sohrabi, M., Henderson, G., Tehrani, D., & Danesh, A. (2000). Visualisation of oil recovery by water alternating gas (WAG) injection using high pressure micromodels - water-wet system, paper SPE 63000. In *SPE Annual Technical Conference and Exhibition*. Dallas, Texas, USA.

Sohrabi, M., Henderson, G., Tehrani, D., & Danesh, A. (2001). Visualisation of oil recovery by water alternating gas (WAG) injection using high pressure micromodels - oil-wet and mixed-wet systems, paper SPE 71494. In *SPE Annual Technical Conference and Exhibition*. New Orleans, Louisiana, USA.

Staffer, F. (1978). Time dependence of the relations between capillary pressure, water content and conductivity during drainage of porous media. In *Proc, Symp. IAHR, Thessaloniki, Greece*.

Tartakovsky, A. M., & Meakin, P. (2006). Pore scale modeling of immiscible and miscible fluid flows using smoothed particle hydrodynamics. *Advances in Water Resources*, *29*, 1464 – 1478.

Tiab, D., & Donaldson, E. C. (2004). *Petrophysics - Theory and Practice of Measuring Reservoir Rock and Fluid Transport Properties*. Elsevier.

Unsal, E., Mason, G., Morrow, N., & Ruth, D. (2007a). Co-current and counter-current imbibition in independent tubes of non-axisymmetric geometry. *Journal of Colloid and Interface Science*, *306*, 105 – 117.

Unsal, E., Mason, G., Ruth, D., & Morrow, N. (2007b). Co- and counter-current spontaneous imbibition into groups of capillary tubes with lateral connections permitting cross-flow. *Journal of Colloid and Interface Science*, *315*, 200 – 20.

Valvatne, P., Piri, M., Lopez, X., & Blunt, M. (2005). Predictive pore-scale modeling of single and multiphase flow. In D. Das, & S. Hassanizadeh (Eds.), *Upscaling Multiphase Flow in Porous Media* (pp. 23–41). Springer Netherlands.

van der Waals, J. (1979). The thermodynamic theory of capillarity under the hypothesis of a continuous variation of density. *Journal of Statistical Physics*, *20*, 200–244.

van Dijke, M. I. J., Lago, M., Sorbie, K. S., & Araujo, M. (2004). Free energy balance for three fluid phases in a capillary of arbitrarily shaped cross-section: capillary entry pressures and layers of the intermediate-wetting phase. *Journal of Colloid and Interface Science*, *277*, 184–201.

van Dijke, M. I. J., McDougall, S. R., & Sorbie, K. S. (2001). Three-phase capillary pressure and relative permeability relationships in mixed-wet systems. *Transport in Porous Media*, *44*, 1–32.

van Dijke, M. I. J., Piri, M., Helland, J. O., Sorbie, K. S., Blunt, M. J., & Skjæveland, S. M. (2007). Criteria for three-fluid configurations

including layers in a pore with nonuniform wettability. *Water Resources Research*, *43*, W12S05.

van Dijke, M. I. J., & Sorbie, K. S. (2002a). Pore-scale network model for three-phase flow in mixed-wet porous media. *Phys. Rev. E*, *66*, 046302.

van Dijke, M. I. J., & Sorbie, K. S. (2002b). The relation between interfacial tensions and wettability in three-phase systems: consequences for pore occupancy and relative permeability. *Journal of Petroleum Science and Engineering*, *33*, 39–48.

van Dijke, M. I. J., & Sorbie, K. S. (2003a). Pore-scale modelling of three-phase flow in mixed-wet porous media: multiple displacement chains. *Journal of Petroleum Science and Engineering*, *39*, 201–216.

van Dijke, M. I. J., & Sorbie, K. S. (2003b). Three-phase capillary entry conditions in pores of noncircular cross-section. *Journal of Colloid and Interface Science*, *260*, 385–397.

van Dijke, M. I. J., Sorbie, K. S., & McDougall, S. R. (2000). A process-based approach for capillary pressure and relative permeability relationships in mixed-wet and fractional-wet system, paper SPE 59310. In *Proc. of the SPE Improved Oil Recovery Symposium held in Tulsa, Oklahoma, USA*.

van Genuchten, M. T. (1980). A closed-form equation for predicting the hydraulic conductivity of unsaturated soils. *Soil Science Society of America Journal*, *44*, 892–898.

Virnovsky, G. A., Lohne, A., & Frette, O. I. (2009). Modeling capillary pressure using capillary bundles with arbitrary cross-sections obtained from photomicrographs. *Journal of Petroleum Science and Engineering*, *69*, 117–128.

Virnovsky, G. A., Vatne, K. O., Iversen, J. E., & Signy, C. (2004). Three-phase capillary pressure measurements in centrifuge at reservoir conditions. In *Proc. of the International Symposium of the Society of Core Analysts*. Abu Dhabi, U.A.E.

Wang, J., & Dong, M. (2011). Trapping of the non-wetting phase in an interacting triangular tube bundle model. *Chemical Engineering Science*, *66*, 250 – 259.

Wu, K., van Dijke, M. I. J., Couples, G. D., Jiang, Z., Ma, J., Sorbie, K. S., Crawford, J., Young, I., & Zhang, X. (2006). 3D stochastic modelling of heterogeneous porous media - applications to reservoir rocks. *Transport in Porous Media*, *65*, 1573–1634.

Yeong, C. L. Y., & Torquato, S. (1998). Reconstructing random media. *Phys. Rev. E*, *57*, 495–506.

Zhou, D., Blunt, M. J., & Orr Jr., F. M. (1997). Hydrocarbon drainage along corners of noncircular capillaries. *J. Coll. Int. Sci.*, *187*, 11–21.

Paper 1

Zhou, Y., Helland, J.O., Hatzignatiou, D.G. (2011)

A model for imbibition in pore spaces from 2D rock images,

In Proc. of the Pore2Field International Conference, IFP Energies nouvelles, France, Nov. 16-18, 2011.

Abstract: We model viscous- and capillary-controlled fluid displacement directly in 2D rock images by considering the identified pore spaces as cross-sections in a bundle of capillary tubes. The phase pressures vary with length positions but remain unique in each cross-section; this leads to a nonlinear system of equations that are solved for the interface positions as a function of time. The cross-sectional fluid configurations are computed accurately at any capillary pressure and wetting condition by a semi-analytical model. Evolution of saturation profiles during imbibition is simulated for different wetting conditions, viscosity ratios and injection rates. An attractive feature of the model is the opportunity to evaluate the effects of pore-scale mechanisms on macro-scale properties because the flow simulations and required input data are calculated consistently in identical geometries.

Paper 2

Zhou, Y., Helland, J.O., and Hatzignatiou, D.G. (2013).

A Dimensionless Capillary Pressure Function for Imbibition Derived From Pore-Scale Modeling in Mixed-Wet-Rock Images. SPE J. 18 (2): 296-308. SPE-154129-PA. http://dx.doi.org/10.2118/154129-PA.

Abstract: It has been demonstrated experimentally that Leverett's J-function yields almost unique dimensionless drainage capillary pressure curves in relatively homogeneous rocks at strongly water-wet conditions, whereas for imbibition at mixed-wet conditions, it does not work satisfactorily because the permeability dependency on capillary pressure has been reported to be weak. The purpose of this study is to formulate a new dimensionless capillary pressure function for mixed-wet conditions on the basis of pore-scale modeling, which could overcome these restrictions. We simulate drainage, wettability alteration, and imbibition in 2D rock images by use of a semianalytical pore-scale model that represents the identified pore spaces as cross sections of straight capillary tubes. The fluid configurations occurring during drainage and imbibition in the highly irregular pore spaces are modeled at any capillary pressure and wetting condition by combining the free-energy minimization with an arc meniscus (AM)-determining procedure that identifies the intersections of two circles moving in opposite directions along the pore boundary. Circle rotation at pinned contact lines accounts for mixed-wet conditions. Capillary pressure curves for imbibition are simulated for different mixed-wet conditions in Bentheim sandstone samples, and the results are scaled by a newly proposed improved J-function that accounts for differences in formation wettability induced by different initial water saturations after primary drainage. At the end of primary drainage, oil-wet-pore wall segments are connected by many water-wet corners and constrictions that remain occupied by water. The novel dimensionless capillary pressure expression accounts for these conditions by introducing an effective contact angle that depends on the initial water saturation and is related to the wetting property measured at the core scale by means of a wettability index.

The accuracy of the proposed J-function is tested on 36 imbibition capillary pressure curves for different mixed-wet conditions that are simulated with the semianalytical model in scanning-electron-microscope (SEM) images of Bentheim sandstone. The simulated imbibition capillary pressure curves and the reproduced curves, based on the proposed J-function, are in good agreement for the mixed-wet conditions considered in this study. The detailed behavior is explained by analyzing the fluid displacements occurring in the pore spaces. It is demonstrated that the proposed J-function could be applied to mixed-wet conditions to generate a family of curves describing different wetting states induced by assigning different wetting properties on the solid surfaces or by varying the initial water saturation after primary drainage. The variability of formation wettability and permeability could be described more accurately in reservoir-simulation models by means of the proposed J-function, and hence the opportunity arises for improved evaluation of core-sample laboratory experiments and reservoir performance.

Paper 3

Zhou, Y., Helland, J.O. and Hatzignatiou, D.G. (2013)

Pore-Scale Modelling of Water Flooding in Mixed-Wet Rock Images: Effects of Initial Saturation and Wettability, SPE Journal. SPE-154284-PA (in press; posted 5 July 2013) http://dx.doi.org/10.2118/154284-PA.

Abstract: We simulate transient behavior of viscous- and capillary-dominated water invasion at mixed-wet conditions directly in scanningelectron- microscope (SEM) images of Bentheim sandstone by treating the pore spaces as cross sections of straight tubes. Initial conditions are established by drainage and wettability alteration. Constant rate or differential pressure is imposed along the tube bundle. The phase pressures vary with positions along the tube length but remain unique in each cross section, consistent with 1D core-scale models. This leads to a nonlinear system of equations that are solved for the interface positions as a function of time. The cross-sectional fluid configurations are computed accurately at any capillary pressure and wetting condition by a semianalytical model that is based on free-energy minimization. The fluid conductances are estimated by newly derived explicit expressions that are shown to be in agreement with numerical computations performed directly on the cross-sectional fluid configurations. An SEM image of Bentheim sandstone is taken as input to the developed model for simulating the evolution of saturation profiles during waterfloods for different flow rates and several mixed-wet conditions, which are established with various initial water saturations and contact angles. It is demonstrated that the simulated saturation profiles depend strongly on initial water saturation at mixedwet conditions. The saturation profiles exhibit increasingly gradual behavior in time as the contact angle, defined on the oil-wet solid surfaces, increases or the initial water saturation decreases. Front menisci associated with positive capillary pressures promote oil displacement by water, whereas for large and negative capillary pressures at small flow rates, oil displaces water because the associated front menisci retract. This results in the development of pronounced gradual saturation fronts at mixed-wet conditions. The waterfloods simulated at conditions established with a large initial water saturation and small contact angle on the oil-wet solid surfaces exhibit sharp Buckley-Leverett saturation profiles for high flow rates because the capillary pressure is small and less important. The shape of the saturation profiles is interpreted on the basis of the simulated capillary pressure curves and the corresponding fluid configurations occurring in the rock image.

Paper 4

Zhou, Y., Helland, J.O., and Jettestuen, E. (2013)

Dynamic Capillary Pressure Curves From Pore-Scale Modeling in Mixed-Wet-Rock Images. SPE J. 18 (4): 634-645. SPE-154474-PA. http://dx.doi.org/10.2118/154474-PA.

Abstract: In reservoir multiphase-flow processes with high flow rates, both viscous and capillary forces determine the pore-scale fluid configurations, and significant dynamic effects could appear in the capillary pressure/saturation relation. We simulate dynamic and quasistatic capillary pressure curves for drainage and imbibition directly in scanning-electron-microscope (SEM) images of Bentheim sandstone at mixed-wet conditions by treating the identified pore spaces as tube cross sections. The phase pressures vary with length positions along the tube length but remain unique in each cross section, which leads to a nonlinear system of equations that are solved for interface positions as a function of time. The cross-sectional fluid configurations are computed accurately at any capillary pressure and wetting condition by combining free-energy minimization with a menisci-determining procedure that identifies the intersections of two circles moving in opposite directions along the pore boundary. Circle rotation at pinned contact lines accounts for mixed-wet conditions. Dynamic capillary pressure is calculated with volume-averaged phase pressures, and dynamic capillary coefficients are obtained by computing the time derivative of saturation and the difference between the dynamic and static capillary pressure. Consistent with previously reported measurements, our results demonstrate that, for a given water saturation, simulated dynamic capillary pressure curves are at a higher capillary level than the static capillary pressure during drainage, but at a lower level during imbibition, regardless of the wetting state of the porous medium. The difference between dynamic and static capillary pressure becomes larger as the pressure step applied in the simulations is increased. The model predicts that the dynamic capillary coefficient is a function of saturation and is independent of the incremental pressure step, which is consistent with results reported in previous studies. The dynamic capillary coefficient increases with decreasing water saturation at water-wet conditions, whereas, for mixed- to oil-wet conditions, it increases with increasing water saturation. The imbibition simulations performed at mixed- to oil-wet conditions also indicate that the dynamic capillary coefficient increases with decreasing initial water saturation.

The proposed modeling procedure provides insights into the extent of dynamic effects in capillary pressure curves for realistic mixed-wet pore spaces, which could contribute to the improved interpretation of core-scale experiments. The simulated capillary pressure curves obtained with the pore-scale model could also be applied in reservoir-simulation models to assess dynamic pore-scale effects on the Darcy scale.

Paper 5

Zhou, Y., Helland, J. O. and Hatzignatiou, D.G. (2013). Computation of three-phase capillary entry pressures and arc menisci configurations in pore geometries from 2D rock images: a combinatorial approach. Submitted to Advances in Water Resources, October 2013.

Abstract: We present a semi-analytical, combinatorial approach to compute three-phase capillary entry pressures for gas invasion into pore throats with constant cross-sections of arbitrary shapes that are occupied by oil and/or water. For a specific set of three-phase capillary pressures, geometrically allowed gas/oil, oil/water and gas/water arc menisci are determined by moving two circles in opposite directions along the pore/solid boundary for each fluid pair such that the contact angle is defined at the front circular arcs. Intersections of the two circles determine the geometrically allowed arc menisci for each fluid pair. The resulting interfaces are combined systematically to allow for all geometrically possible three-phase configuration changes. The three-phase extension of the Mayer & Stowe – Princen method is adopted to calculate capillary entry pressures for all determined configuration candidates, from which the most favorable gas invasion configuration is determined. The model is validated by comparing computed three-phase capillary entry pressures and corresponding fluid configurations with analytical solutions in idealized triangular star-shaped pores. It is demonstrated that the model accounts for all scenarios that have been analyzed previously in these shapes. Finally, three-phase capillary entry pressures and associated fluid configurations are computed in throat cross-sections extracted from segmented SEM images of Bentheim sandstone. The computed gas/oil capillary entry pressures account for the expected dependence of oil/water capillary pressure in spreading and non-spreading fluid systems at the considered wetting conditions. Because these geometries are irregular and include constrictions, we introduce three-phase displacements that have not been identified previously in pore-network models that are based on idealized pore shapes. However, in the limited number of pore geometries considered in this work, we find that the favorable displacements are not generically different from those already encountered in network models previously, except that the size and shape of oil layers that are surrounded by gas and water are described more realistically. The significance of the results for describing oil connectivity in porous media accurately can only be evaluated by including throats with more complex cross-sections in three-phase pore-network models.

Paper 6

Zhou, Y., Helland, J.O., Hatzignatiou, D.G. (2013)

Simulation of three phase capillary pressure curves directly in 2D rock images, paper IPTC 16547 presented at the International Petroleum Technology Conference held in Beijing, China, 26–28 March 2013.

Abstract: Pore-scale modeling of three-phase capillary pressure in realistic pore geometries could contribute to an increased knowledge of three-phase displacement mechanisms and also provide support to time-consuming and challenging core-scale laboratory measurements. In this work we have developed a semi-analytical model for computing three-phase capillary pressure curves and the corresponding three-phase fluid configurations in uniformly-wet rock images encountered during tertiary gas invasion. The fluid configurations and favorable entry pressure are determined based on free energy minimization by combining all physically allowed gas-oil, gas-water, and oil-water arc menisci in various ways. The model is shown to reproduce all three-phase displacements and capillary entry pressures that previously have been derived in idealized angular tubes for gas invasion at uniform water-wet conditions. These single-pore displacement mechanisms include (i) gas invasion into pores occupied by oil and water leading to simultaneous displacement of the three fluids, (ii) simultaneous invasion of bulk gas and surrounding oil into water filled pores, and finally (iii) the pure two-phase fluid displacements in which gas invades pores occupied by either water or oil.

The proposed novel semi-analytical model is validated against existing analytical solutions developed in a star-shape pore space, and subsequently employed on an SEM image of Bentheim sandstone to simulate three-phase fluid configurations and capillary pressure curves at uniform water-wet conditions and different spreading coefficents. The simulated fluid configurations for the different spreading coefficients show similar oil layer behaviour as previously published experimental three-phase fluid configurations obtained by computed microtomography in Bentheim sandstone. The computed saturation paths indicate that three-phase oil-water capillary pressure is a function of the water saturation only, whereas the three-phase gas-oil capillary pressure appears to be a function of two saturations. This is explained by the three-phase displacements occurring in the majority of the simulations, in which gas-water interfaces form immediately during gas invasion into oil- and water-saturated pore shapes.

Paper 7

Zhou, Y., Helland, J.O., Hatzignatiou, D.G. (2013)

Simulation of three phase capillary pressure curves directly in 2D uniformly-wet rock images. Manuscripts under preparation, 2013.

Abstract: Pore-scale modeling of three-phase capillary pressure in realistic pore geometries could contribute to an increased knowledge of three-phase displacement mechanisms and also provide support to time-consuming and challenging core-scale laboratory measurements. In this work we have developed a semi-analytical model for computing three-phase capillary pressure curves and the corresponding three-phase fluid configurations for gas invasion processes in uniformly-wet rock images. The fluid configurations and favorable capillary entry pressures are determined based on free energy minimization by combining all physically allowed gas-oil, gas-water, and oil-water arc menisci in various ways. The model is shown to reproduce all three-phase displacements and capillary entry pressures that previously have been derived in idealized angular tubes for gas invasion at uniform water-wet conditions. These single-pore displacement mechanisms include (i) gas invasion into pores occupied by oil and water leading to simultaneous displacement of the three fluids, (ii) simultaneous invasion of bulk gas and surrounding oil into water filled pores, and finally (iii) the pure two-phase fluid displacements in which gas invades pores occupied by either water or oil.

The proposed semi-analytical model is validated against existing analytical solutions developed in a star-shape pore space, and subsequently employed on an SEM image of Bentheim sandstone to calculate three-phase fluid configurations and capillary pressure curves at uniform water-wet conditions and different spreading coefficients for gas invasion processes. The simulated fluid configurations for the different spreading coefficients show similar oil layer behaviour as previously published experimental three-phase fluid configurations obtained by micro-tomography in Bentheim sandstone. The computed saturation paths for gas invasion indicate that the oil-water capillary pressure can be described as a function of the water saturation only. The gas-oil capillary pressure can be represented as a function of only the gas saturation in the major part of the three-phase region, despite three-phase displacements in which gas displaces both oil and water occur frequently in individual pore geometries for the non-spreading systems, which slightly reduces the accuracy of such a representation. At small oil saturations, the simulated results indicate that the gas-oil capillary pressure depends strongly on two saturations, which is particularly visible in the weakly water-wet spreading system because thin oil layers still exists when gas has started to invade water-filled pore geometries.